Isotope dependence of the H-mode pedestal in JET-ILW plasmas

Laszlo Horvath

Doctor of Philosophy
University of York
Physics
September 2019

Abstract

In tokamak H-mode plasmas, the level of energy and particle transport at the plasma edge is reduced and a steep pressure gradient is formed, giving rise to an edge pressure "pedestal", which positively affects the global energy confinement. A positive isotope mass scaling of the thermal energy confinement time in H-mode plasmas has been observed in several tokamaks, however, this favourable isotope dependence has not yet been fully understood theoretically. This thesis examines the pedestal structure, edge transport, linear MHD stability and inter-ELM edge current evolution in a series of JET-ILW Hydrogen (H) and Deuterium (D) type I ELMy H-mode plasmas with the aim to better understand the isotope dependence of the pedestal and its contribution to the favourable isotope scaling. Simulations of the inter-ELM edge current evolution showed that current diffusion contributes little to the time evolution of the total edge current prior to the ELM crash. Therefore, current diffusion does not explain why JET-ILW type I ELMy pedestals at high gas rate and moderate to high β_N are found to be stable to Peeling-Ballooning modes. The pedestal pressure is typically higher in D than in H at the same input power and gas rate, with the difference mainly due to lower density in H than in D. Analysis of the pedestal structure and power balance, and results of interpretative 2D edge transport simulations with EDGE2D-EIRENE indicate that the difference in neutral penetration between H and D leads only to minor changes in the pedestal density and temperature profiles, and differences in heat and particle transport must also play a role in the favourable isotope scaling of the pedestal. The effect of the isotope mass on linear MHD pedestal stability is small, but an indirect isotope dependence through the separatrix temperature is qualitatively consistent with the reduced pedestal confinement in H and could play a role in JET-ILW H-mode plasmas at low gas rate.

Contents

Acknowledgements

I would like to express my special thanks to my supervisor at CCFE, Costanza Maggi, for her continuous support and motivation. This thesis would not have been possible to write without her help. My sincere thanks also go to my York supervisor, Kieran Gibson, for his help through these years.

I would like to thank my colleagues at JET, CCFE and York, who have helped me with their advice during my time in Culham. I would like to thank all the students I have met during my PhD, especially the Fusion CDT cohort, who have made these years a more enjoyable experience. Here, I have to mention Samuel Ward for his support when it was really needed... Special thanks go to my friends, Michail and Siobhan, for the moments we have spent and will spend together. I am very lucky to have them. A special mention must also go to Zsolt for those lunches we have had in Culham.

Last and by all means most, I thank my family. Words cannot express how grateful I am for all of the sacrifices that they have made on my behalf. Finally, I owe much to my fiancée, Eszter, without whose love I would not have completed this work.

This work was supported by the Engineering and Physical Sciences Research Council [EP/L01663X/1]. This work has been carried out within the framework of the EUROfusion Consortium and has received funding from the Euratom research and training programme 2014-2018 and 2019-2020 under grant agreement No 633053. The views and opinions expressed herein do not necessarily reflect those of the European Commission.

Author's declaration

I declare that this thesis is a presentation of original work and I am the sole author. This work has not previously been presented for an award at this, or any other, University. All sources are acknowledged as References.

The work presented in this thesis was performed at the Culham Centre for Fusion Energy whilst working on JET under the joint supervision of Dr. Costanza Maggi and Prof. Kieran Gibson. Note, that

- The HRTSfit pedestal fitting routine has been developed and maintained by Dr. Lorenzo Frassinetti.
- The EDGE2D-EIRENE simulations presented in section 6.3 for a pair of JET-ILW hydrogen and deuterium plasmas were initially set up by Alex Chankin with constraints on the upstream kinetic profiles. Extension of the simulations to match the divertor target heat flux profiles and optimisation for the inter-ELM phase of the discharges was carried out by myself.

This thesis contains work previously presented at conferences and published in peer-reviewed journal articles as listed in the following list of publications and conferences.

List of publications and conferences

Publications in Scientific Journals as first author

- **L. Horvath**, C. F. Maggi, A. Chankin, S. Saarelma, A. R. Field, S. Aleiferis, E. Belonohy, A. Boboc, G. Corrigan, E. G. Delabie, J. Flanagan, L. Frassinetti, C. Giroud, D. Harting, D. Keeling, D. King, M. Maslov, G. F. Matthews, S. Menmuir, S. A. Silburn, J. Simpson, A. C. C Sips, H. Weisen, K. J. Gibson and JET Contributors, Isotope dependence of the type I ELMy H-mode pedestal in JET-ILW Hydrogen and Deuterium plasmas. submitted to Nuclear Fusion, 2019.

- **L. Horvath**, C. F. Maggi, F. J. Casson, V. Parail, L. Frassinetti, F. Koechl, S. Saarelma, M. G. Dunne, K. J. Gibson and JET Contributors, Inter-ELM evolution of the edge current density in JET-ILW type I ELMy H-mode plasmas. Plasma Physics and Controlled Fusion, 60 085003, 2018.

Publications in Scientific Journals as co-author

- S. Saarelma, L. Frassinetti, P. Bilkova, C. D. Challis, A. Chankin, R. Fridström, L. Garzotti, **L. Horvath**, C. F. Maggi and JET Contributors, Self-consistent pedestal prediction for JET-ILW in preparation of the DT campaign. Physics of Plasmas, 26 072501, 2019.

- C. F. Maggi, H. Weisen, F. J. Casson, F. Auriemma, R. Lorenzini, H. Nordman, E. Delabie, F. Eriksson, J. Flanagan, D. Keeling, D. King, **L. Horvath**, S. Menmuir, A. Salmi, G. Sips, T. Tala, I. Voitsekhovich and JET Contributors, Isotope identity experiments in JET-ILW with H and D L-mode plasmas. Nuclear Fusion, 59 076028, 2019.

- L. Frassinetti, M. G. Dunne, U. Sheikh, S. Saarelma, C. M. Roach, E. Stefanikova, C. Maggi, **L. Horvath**, S. Pamela, E. de la Luna, E. Wolfrum, M. Bernert, P. Blanchard, B. Labit, A. Merle, L. Guimarais, S. Coda, H. Meyer, J. C. Hillesheim, the ASDEX Upgrade Team, JET Contributors, the TCV Team and the EUROfusion MST1 Team, Role of the pedestal position on the pedestal performance

in AUG, JET-ILW and TCV and implications for ITER. Nuclear Fusion, 59 076038, 2019.

- C. Perez von Thun, L. Frassinetti, **L. Horvath**, S. Saarelma, L. Meneses, E. de la Luna, M. Beurskens, J. Boom, J. Flanagan, J. C. Hillesheim, C. F. Maggi, S. J. P. Pamela, E. R. Solano and JET Contributors, Long-lived coupled peeling ballooning modes preceding ELMs on JET. Nuclear Fusion, 59 056004, 2019.
- C. F. Maggi, H. Weisen, J. C. Hillesheim, A. Chankin, E. Delabie, **L. Horvath**, F. Auriemma, I. S. Carvalho, G. Corrigan, J. Flanagan, L. Garzotti, D. Keeling, D. King, E. Lerche, R. Lorenzini, M. Maslov, S. Menmuir, S. Saarelma, A. C. C. Sips, E. R. Solano, E. Belonohy, F. J. Casson, C. Challis, C. Giroud, V. Parail, C. Silva, M. Valisa, JET Contributors, Isotope effects on L-H threshold and confinement in tokamak plasmas. Plasma Physics and Controlled Fusion, 60 014045, 2018.
- C. Bowman, D. Dickinson, **L. Horvath**, A. E. Lunniss, H. R. Wilson, I. Cziegler, L. Frassinetti, K. Gibson, A. Kirk, B. Lipschultz, C. F. Maggi, C. M. Roach, S. Saarelma, P. B. Snyder, A. Thornton, A. Wynn and JET Contributors, Pedestal evolution physics in low triangularity JET tokamak discharges with ITER-like wall. Nuclear Fusion, 58 016021, 2018.
- C. F. Maggi, L. Frassinetti, **L. Horvath**, A. Lunniss, S. Saarelma, H. Wilson, J. Flanagan, M. Leyland, I. Lupelli, S. Pamela, H. Urano, L. Garzotti, E. Lerche, I. Nunes, F. Rimini and JET Contributors, Studies of the pedestal structure and inter-ELM pedestal evolution in JET with the ITER-like wall. Nuclear Fusion, 57 116012, 2017.

Conference contributions

Talks

- **L. Horvath et al.** Isotope dependence of the pedestal in JET-ILW type I ELMy H-modes. 46th EPS Plasma Physics Conference, Milan, Italy, 2019-07-11.
- **L. Horvath et al.** Isotope effect of the H-mode pedestal in JET-ILW hydrogen and deuterium plasmas. 23rd Joint EU-US Transport Task Force Meeting, Seville, Spain, 2018-09-11.

Posters

- **L. Horvath et al.** Effect of current diffusion on the inter-ELM pedestal evolution in JET-ILW type I ELMy H-mode plasmas. 45th IOP Plasma Physics Conference, Belfast, UK, 2018-04-09.
- **L. Horvath et al.** Analysis of the pedestal structure and stability in H and D plasmas on JET-ILW. KSTAR Conference 2018, Muju Deogyusan Resort, South Korea, 2018-02-22.

- **L. Horvath et al.** Pedestal structure and stability in H and D isotope experiments on JET-ILW. 44th EPS Plasma Physics Conference, Belfast, UK, 2017-06-30.
- **L. Horvath et al.** Evolution of the bootstrap current profile during the type I ELM cycle of JET-ILW H-mode plasmas. 43rd EPS Plasma Physics Conference, Leuven, Belgium, 2016-07-05.
- **L. Horvath et al.** Outline of a PhD project on the investigation of the isotope effects of the pedestal on JET. 43rd IOP Plasma Conference, Isle of Skye, UK, 2016-05-23.

Chapter 1

Introduction

There are many approaches to meet the energy demand of the world. One of them, which is already in the service of mankind, is the release of atomic binding energy. Today's nuclear power plants generate electricity by nuclear fission of heavy elements. Another way of utilising atomic binding energy for electricity production would be nuclear fusion. Nuclear fusion is a reaction in which two or more light atomic nuclei are combined to form heavier nuclei. Fusion could provide a clean and safe energy source with practically inexhaustible fuel [1]. However, several physics and engineering challenges remain to be solved before sustainable energy production from fusion reactions to the electricity grid can be achieved [2].

1.1 Nuclear fusion

A natural occurrence of fusion energy production is the Sun, which provides energy to life for several billions of years on Earth. Its hydrogen (^{1}H) fuel is converted to helium (^{4}He) in different astrophysical reaction chains [3]. These reaction chains have a very low reaction rate as a proton-neutron decay has to occur. Therefore, the fusion power density of the core of the Sun is in the order of 200 W/m^3 [4]. The low power density is compensated by the astronomically large mass of the Sun, but terrestrial reproduction of stellar core conditions for the generation of electricity would be highly inefficient. For terrestrial realisation of a fusion power plant, other fusion reactions need to be chosen with light elements such as deuterium (^{2}H $\equiv$ D), tritium (^{3}H $\equiv$ T) or ^{3}He [5]:

$$\begin{aligned} \mathrm{D} + \mathrm{D} &\Rightarrow\ {}^3\mathrm{He}\ (0.82\ \mathrm{MeV}) + \mathrm{n}\ (2.45\ \mathrm{MeV}), \\ \mathrm{D} + \mathrm{D} &\Rightarrow\ \mathrm{T}\ (1.01\ \mathrm{MeV}) \quad + \mathrm{p}\ (3.02\ \mathrm{MeV}), \end{aligned}$$

$$\mathbf{D + T} \quad \Rightarrow \quad \mathbf{^4He}\ (3.52\ \text{MeV}) + \mathbf{n}\ (14.1\ \text{MeV}),$$
$$\text{D} + {}^3\text{He} \Rightarrow \quad {}^4\text{He}\ (3.66\ \text{MeV}) \quad + \text{p}\ (14.6\ \text{MeV}).$$

The reaction rates for the above mentioned fusion reactions are shown in figure 1.1. The reaction rate is given by the integral of the energy dependent fusion cross-section over a Maxwellian energy distribution. As shown in figure 1.1, the most favourable fusion reaction is the deuterium-tritium (DT) reaction [6]. Its reaction rate peaks at a lower temperature and at a higher value than the other reactions commonly considered for fusion energy.

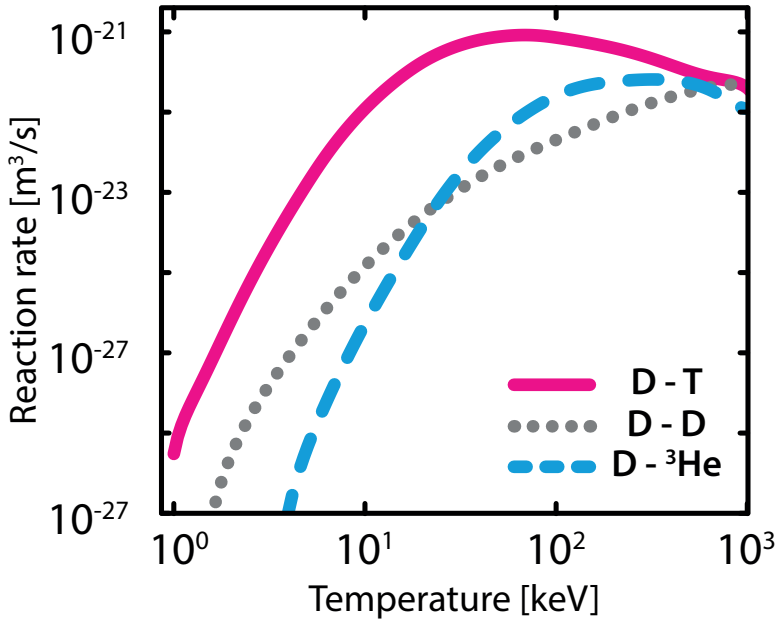

Figure 1.1: The reaction rates of fusion reactions commonly considered for terrestrial fusion power plants [7].

In terms of the required fuel, the use of the DT reaction is challenging. On one hand, large amount of deuterium is available in nature and can easily be extracted at a low cost. In natural water resources there is one atom of deuterium for every 6700 atoms of hydrogen [5]. However, tritium is not naturally extractable as it only exists in trace quantities [8]. It is a radioactive isotope with a half-life of 12.3 years. Since there is no external tritium breeding technology, which could satisfy the demand of a fusion power plant, the required tritium must be produced by the reactor itself. The proposed way of tritium breeding in a power plant is taking advantage of the fusion reaction generated neutrons and the following lithium reactions [5]:

$$^{6}\mathrm{Li} + \mathrm{n} = {}^{4}\mathrm{He} + \mathrm{T}$$
$$^{7}\mathrm{Li} + \mathrm{n} = {}^{4}\mathrm{He} + \mathrm{T} + \mathrm{n}$$

As illustrated in figure 1.2, the fusion-born neutrons can be utilised for tritium breeding as they hit the wall containing lithium. Tritium can then be extracted and burnt in the fusion reaction. Thus, in practical terms, the fuel for a DT fusion reactor is deuterium and lithium. In quantities required for fusion, lithium can even be extracted from seawater providing practically inexhaustible reserves [9].

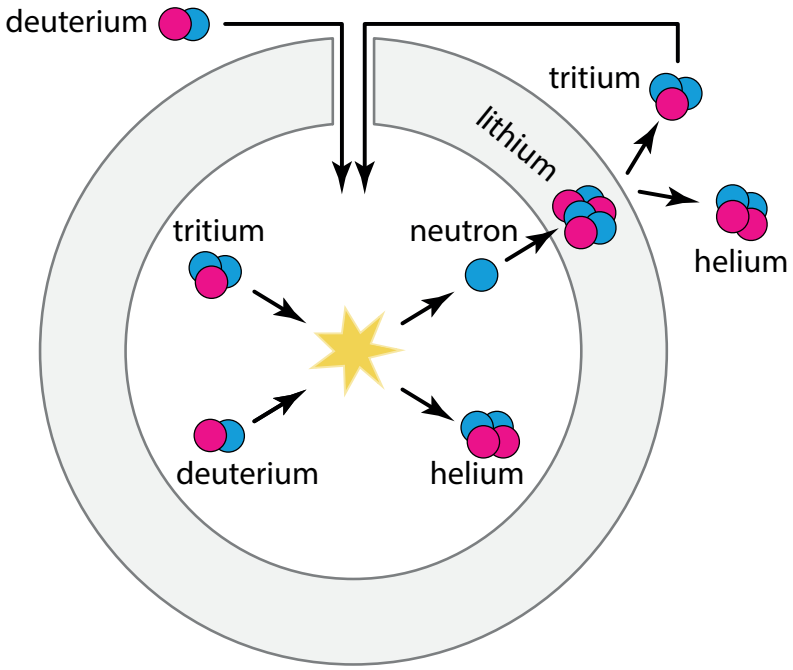

Figure 1.2: Operational scheme of tritium breeding. The fusion-born neutrons, by hitting the wall containing lithium, produce tritium.

For a fusion reaction to occur, the positively charged atomic nuclei must collide at high enough energies to overcome their strong electrostatic repulsion. As the cross-section of Coulomb scattering is several orders of magnitude higher than the cross-section of the fusion reaction [10], a simple scheme of an accelerator firing particles into a target cannot achieve positive energy balance. Too much energy would be lost from the reacting region through Coulomb collisions. The most promising method is the so-called thermonuclear fusion, where the fusion fuel is heated to sufficiently high temperature such that the thermal velocities are high enough to produce fusion reactions [7]. In such a case the Coulomb collisions just redistribute the energy between the particles, but it does not get lost from the system.

The necessary conditions for thermonuclear fusion can be estimated by a simple power balance argument. Initially, external heating is required to heat the fuel to high enough temperatures for fusion reactions. But, in an ideal, steady state case, the energy produced in fusion reactions can heat the reaction region and keep the system self-sustained with no external heating. This is called ignition. To reach ignition, the fusion heating (P_{fus}) needs to exceed the losses (P_{loss}):

$$P_{\text{fus}} \geq P_{\text{loss}} \ . \tag{1.1}$$

In a DT reaction - as imposed by momentum conservation - 4/5 of the fusion energy is carried by the neutrons. As the neutron has no charge, it interacts weakly with matter, thus immediately escapes the reaction region. Therefore, self-sustained fusion relies on the heating of the fusion-born α-particles, which - assuming Maxwellian energy distribution and 50-50 % DT mixture - is given by

$$P_{\text{fus}} = P_{\alpha} \ = \frac{1}{4} n^2 \langle \sigma v \rangle E_{\alpha} \ , \tag{1.2}$$

where n is the density, $\langle \sigma v \rangle$ is the fusion reaction rate and $E_{\alpha} = 3.52$ MeV is the energy of the fusion-born α-particle. The losses are expressed in terms of the energy confinement time (τ_E), which measures the rate at which the system loses energy to its environment:

$$\tau_E = \frac{W}{P_{\text{loss}}}, \tag{1.3}$$

where $W = 3nTV$ is the total energy content with T the temperature and V the volume of the reaction region. Substituting eq. (1.2) and eq. (1.3) into eq. (1.1) gives:

$$n\tau_E > \frac{12T}{E_{\alpha} \langle \sigma v \rangle}. \tag{1.4}$$

Replacing $T/\langle \sigma v \rangle$ with its minimum value, which is around 25 keV, leads to the Lawson criterion for ignition [11]:

$$n\tau_E > 1.5 \cdot 10^{20} \text{s/m}^3. \tag{1.5}$$

This shows that the fusion fuel has to be confined for long enough time (τ_E) and sufficiently high density around the optimal temperature to reach ignition. The fusion power gain (Q) is the ratio of the fusion power and the power required to maintain the plasma in steady state. Ideally, the fusion power gain is $Q = \infty$ in case of ignition. However, in practice, fusion ignition is not necessarily needed for fusion energy

production. Net energy gain can be reached by a small amount of external heating and $Q \approx 20 - 40$, but α-heating must dominate the heating mix [8].

1.2 The tokamak

Due to the excessive temperatures required for fusion, contact between the hot core of the reaction volume and any solid wall material is impracticable. One way of confining the fusion fuel is to employ a magnetic field. At temperatures necessary for the fusion reaction, the particles are ionised and the fuel is in the plasma state. Charged particles (ions and electrons) in a magnetic field are subject to the Lorentz force:

$$\mathbf{F} = q(\mathbf{E} + \mathbf{v} \times \mathbf{B}) \ , \tag{1.6}$$

where q is the charge and $\mathbf{v}$ is the velocity of the particle, $\mathbf{E}$ is the electric field and $\mathbf{B}$ is the magnetic field. The Lorentz force acts perpendicular to both $\mathbf{v}$ and $\mathbf{B}$. As a result, particles are free to move along magnetic field lines, but are trapped in a circular orbit in the perpendicular direction. This helical motion - the so-called gyromotion - is suitable to confine the plasma, because it does not allow the particles to move perpendicular to the magnetic field.

The problem of losses at the ends of a linear device can be solved by bending the magnetic field lines into a torus. The coordinates used in a toroidal system are shown in figure 1.3. The distance measured from the centre of the torus to the centre of the plasma column is the major radius (R_0). The minor radius ($r = a$) is measured from the centre of the plasma column to the edge. The toroidal direction is the long way, the poloidal direction is the short way around the torus. The corresponding coordinates to toroidal and poloidal directions are denoted by Φ and Θ, respectively.

In a torus shaped geometry, the strength of the toroidal magnetic field (B_Φ) is inversely proportional to R, because the higher current density in the toroidal field coils on the inner side of the torus results in a stronger magnetic field there. This inhomogeneity leads to a charge dependent drift (∇B drift) [7], which causes the electrons and ions to move in vertically opposite directions. The resulting vertical electric field creates a charge independent $\mathbf{E} \times \mathbf{B}$ drift [7], which moves the entire plasma towards the outside of the torus. This electric field between the top and the bottom of the torus needs to be cut short by helically twisting the magnetic field lines.

A type of magnetic confinement device, where the magnetic field lines are helically twisted by a toroidal plasma current is the tokamak [7]. Figure 1.4 illustrates the main

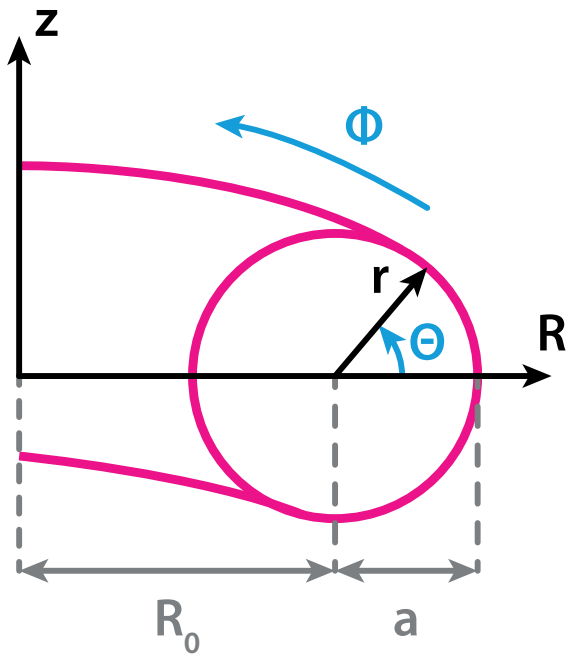

Figure 1.3: The coordinates in a toroidal system. R_0 is the major radius, a is the minor radius ($r = a$), Φ is the toroidal coordinate (long way around the torus) and Θ is the poloidal coordinate (short way around the torus).

components of a tokamak. The plasma is shown in magenta, surrounded by the vacuum vessel (in light grey) and the toroidal field coils (in cyan). The toroidal plasma current (I_p) is driven by a transformer coil, which is shown in grey inside the toroidal field coils in figure 1.4. The plasma current generates a poloidal magnetic field (B_Θ), which twists the magnetic field lines. The twist of magnetic field lines is described by the safety factor q, which is the number of toroidal transits per single poloidal transit of a magnetic field line [12]:

$$q = \frac{1}{2\pi} \oint \frac{1}{R_0} \frac{B_\Phi}{B_\Theta} \mathrm{d}s \approx \frac{r}{R_0} \frac{B_\Phi}{B_\Theta} \ . \tag{1.7}$$

If q is a low order rational, the field line joins up on itself after a few turns, and such a configuration is subject to instabilities. For stable tokamak operation q is kept above 3 at the plasma edge and slightly above 1 at the magnetic axis [12].

The circular orbit of the particles in gyromotion is defined by the gyroradius:

$$\rho = \frac{m v_\perp}{qB} \ . \tag{1.8}$$

In a typical tokamak plasma, the gyroradius is much smaller than the macroscopic size of the plasma ($\rho \ll a$). This scale restriction is required to treat the plasma as an electrically conducting fluid and leads to the theory of magnetohydrodynamics (MHD). Further assumptions and derivation of the MHD model can be found in [13]. MHD is

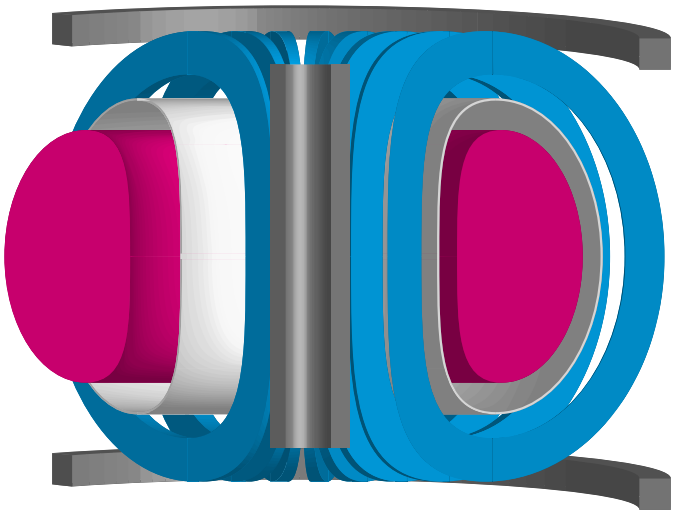

Figure 1.4: Schematic drawing of a tokamak. The plasma is shown in magenta, surrounded by the vacuum vessel (in light grey) and the toroidal field coils (in cyan). The transformer coil inside the toroidal field coils and the poloidal field coils at the top and bottom of the device are shown in grey.

a fluid model, which together with the Maxwell-equations, describes the macroscopic equilibrium and stability properties of a plasma.

The MHD equilibrium in a magnetised plasma is given by the following force balance equation:

$$\mathbf{j} \times \mathbf{B} = \nabla p \ , \tag{1.9}$$

where $\mathbf{j}$ is the current density and ∇p is the pressure gradient. Eq. (1.9) shows that the plasma pressure is balanced by the $\mathbf{j} \times \mathbf{B}$ force. It also implies that both $\mathbf{j}$ and $\mathbf{B}$ are perpendicular to the pressure gradient, meaning that magnetic field lines and current lie on surfaces of constant pressure. These surfaces are called magnetic flux surfaces and as a result of the axisymmetric nature of a tokamak (to good approximation), these are organised as a series of closed, nested surfaces. Since the particles can move freely along the magnetic field lines, several plasma parameters - so-called flux surface quantities - are approximately constant on a magnetic flux surface. It is convenient to label the flux surfaces with one of these flux surface quantities. The poloidal flux contained within any given pressure contour is often used for this purpose:

$$\Psi = \int \mathbf{B} \cdot d\mathbf{S_p} \ , \tag{1.10}$$

where $d\mathbf{S_p}$ is the poloidal surface element.

The balance of the plasma pressure and magnetic field can be described by the plasma beta, β:

$$\beta = \frac{p}{B^2/2\mu_0} \ . \tag{1.11}$$

In some sense, β describes the efficiency of plasma confinement at a given magnetic field. For fusion energy, high values of β are required (maximising plasma pressure at a given magnetic field), but MHD equilibrium and stability requirements limit the maximum achievable value in a given configuration. Often the following normalisation of β is used:

$$\beta_N = \beta \frac{aB_\Phi}{I_p} \tag{1.12}$$

where a is measured in [m], B_Φ in [T], I_p in [MA] and β_N is expressed in percentage.

In a tokamak, the plasma sits inside a torus shaped vacuum chamber, which is usually located inside the magnetic field coils. High vacuum is required because the plasma density is ~ 5 orders of magnitude lower than the atmosphere. The inductively driven toroidal plasma current provides heating (Ohmic heating) through the resistance caused by electron-ion collisions. The resistance of the plasma scales with $\sim T_e^{-3/2}$ (with T_e the electron temperature), thus the efficiency of Ohmic heating sharply drops at high temperatures. As a result, Ohmic heating alone in a tokamak would only be enough to heat a plasma to ≈ 1 keV [7], which is not sufficient for ignition. In order to top-up the Ohmic heating, several different external heating methods can be applied. One method used for auxiliary heating is Neutral Beam Injection (NBI), where ions are accelerated to typically 40 keV to 1 MeV [8]. The ion beam is neutralised before injection so that the beam can travel into the plasma unaffected by the magnetic field. The beam atoms then become ionised and transfer their energy to the background plasma through collisions. The other important external heating method is radio frequency (RF) heating. Electromagnetic waves with a frequency either around the ion cyclotron, the electron cyclotron or the lower hybrid frequency can be injected such that the waves are absorbed in the plasma. Accordingly, these heating systems are named as ion cyclotron resonance heating (ICRH), electron cyclotron resonance heating (ECRH) or lower hybrid (LH) heating.

As described above, closed magnetic flux surfaces are essential for the confinement of the plasma. However, flux surfaces at the edge of the plasma inevitably intersect with the plasma facing wall components. In tokamak terminology, magnetic field lines outside the last closed flux surface (LCFS) are called open field lines. In order to control the plasma shape and position, a tokamak is installed with so-called poloidal field coils (grey coils

in figure 1.4). Non-circular shapes can have a positive effect on plasma performance and stability. The two main shaping parameters are triangularity (δ) and elongation (κ). κ is the ratio of the height of the plasma and the minor radius. Upper or lower triangularity is defined as the horizontal distance between the major radius and the highest or lowest vertical point of the LCFS divided by the minor radius.

By driving current in the direction of I_p in a poloidal field coil under the plasma, a so-called X-point can be generated on the LCFS as shown in figure 1.5. In such a configuration the plasma wall interaction is localised to the so-called divertor, away from the core plasma. This helps to keep sputtering of the wall material far from the confined region, thus reducing the impurity content in the plasma. In divertor configuration a magnetic separatrix separates the open and closed field lines and defines the LCFS. The region outside the separatrix, where the plasma streams along open field lines is called the scrape-off layer (SOL). The private plasma region is under the X-point. Where the separatrix hits the divertor is called the strike point.

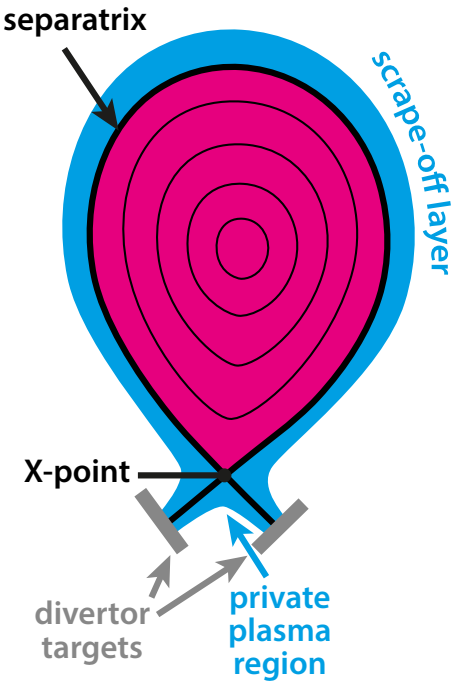

Figure 1.5: Schematic figure of the poloidal cross-section of a tokamak, showing the different regions of the plasma.

Tokamak experiments are in the focus of fusion energy research all over the world. The most important devices currently in operation or under upgrade are the Joint European Torus (JET) in the UK [14], ASDEX-Upgrade in Germany [15], DIII-D in the US [16], JT-60SA in Japan [17, 18], KSTAR in South Korea [19] and EAST in China [20]. Since the 1950s invention of the tokamak, considerable improvement has been achieved in plasma confinement and the plasma performance is approaching the burning plasma regime. In

1997, JET achieved a maximum of 16 MW fusion power using 25 MW of external heating in a transient discharge [21]. The next step large tokamak experiment currently being built in the south of France is ITER [22]. Its goal is to demonstrate burning plasma operation, namely 500 MW fusion power using only 50 MW of auxiliary heating. The first plasma is foreseen in 2025 [22].

In order to realise fusion energy production, further optimisation of plasma confinement is needed. The energy confinement time of the plasma is determined by how rapidly particles and energy are lost from a plasma by means of transport. Plasma transport can be characterised by continuity equations for the particles, heat and momentum for each plasma species. These equations describe the response of the density, temperature and rotation profiles to the fluxes and sources. For example, the continuity equation for the density can be written in the following form:

$$\frac{\partial n}{\partial t} + \nabla \cdot \Gamma = S_n \ , \tag{1.13}$$

where Γ is the particle flux and S_n is the particle source. Similar equations can also be written for the temperature and momentum. The task of transport theory is to calculate the fluxes.

Transport through Coulomb collisions in toroidal geometry is described by neoclassical theory [23]. However, in a tokamak plasma transport is typically dominated by turbulence driven micro-instabilities, which is also called anomalous transport. Turbulent transport is generally discussed within the framework of gyrokinetic theory [24–26]. The first principles description of magnetised plasmas is the kinetic description. In kinetic theory, the time evolution of the particle distribution function is described in the 6 dimensional phase space. The 7 dimensional (3 spatial, 3 velocity and 1 time), full kinetic description is very difficult to solve for macroscopic plasma behaviour. However, the trajectory of the plasma particles can be decomposed into a slow drift of the guiding centre and the fast gyromotion. The gyrokinetic equation can be obtained by averaging over the gyromotion. In this way the number of dimensions is reduced by one and the plasma is described as the evolution of charged rings with a guiding centre position.

Instead of reducing the dimensions of the model, the kinetic description can also be simplified by taking various velocity moments of the kinetic equation. This leads to a set of fluid equations for each plasma species. The two-fluid model describes the plasma as interacting electron and ion fluids, including self-consistent calculation of the electric

and magnetic fields. The briefly introduced MHD theory is a one-fluid description of the plasma.

These theories are implemented in simulations codes and continuously being improved and validated against the experiments. It is important to note that the majority of current tokamak experiments are operating with a deuterium plasma. In fact, the only two experimental campaigns with DT plasma were in the 90s at JET and TFTR. As a result, most of the tokamak plasma simulation tools are optimised and validated with deuterium plasmas. From the plasma physics point of view, the main difference when the isotope of the main ion is modified is the change in ion gyroradius. This influences the transport and thereby affects the confinement. The different isotope mass potentially also effects how neutral atoms, which are injected into the vacuum chamber or recycled from the walls, penetrate into the plasma. The isotope effect in fusion plasma physics is a subject currently undergoing intense study in preparation for upcoming DT experiments on JET and ITER.

1.3 High confinement mode

Over the long history of magnetic confinement fusion research, significant improvement in the performance of tokamak plasmas has been achieved through exploiting enhanced confinement regimes. The most developed enhanced confinement regime is the so-called High confinement mode or H-mode was discovered in 1982 at the ASDEX tokamak [27] and is now routinely accessed in most experiments. H-mode can be reached when the heating power is high enough to exceed a certain threshold. The mode below this power threshold is correspondingly called the low confinement mode or L-mode. With the H-mode confinement regime, about a factor of 2 improvement in global confinement can be gained compared to L-mode. The improvement in confinement is due to the formation of a narrow transport barrier in the outer region of the plasma. Inside the transport barrier the level of energy and particle transport is reduced and a steep pressure gradient is formed, which gives rise to a pressure pedestal as illustrated in figure 1.6. Although the physics of the transition to H-mode is not fully understood, it is widely accepted that sheared flows play an important role. Zonal flow and equilibrium $\mathbf{E} \times \mathbf{B}$ flow shear can lead to a reduction in anomalous transport by breaking up the turbulent eddies, thus suppressing the dominant transport mechanism [28, 29].

The heightened edge pressure in H-mode also leads to higher pressure in the plasma core due to core profile stiffness, thus positively affecting the global confinement [30, 31].

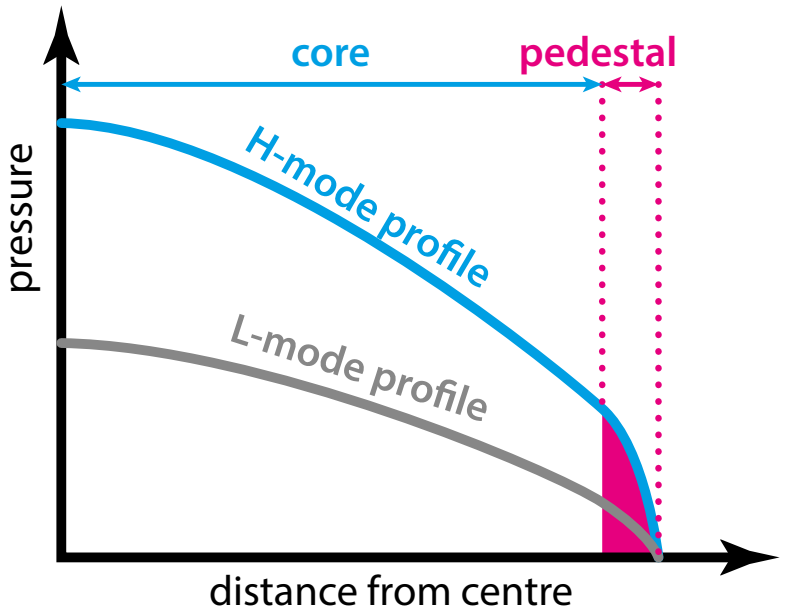

Figure 1.6: Schematic drawing of the pressure profile in L- and H-mode. In H-mode, the transport is reduced at the plasma edge leading to a steep pressure gradient region, called the pedestal.

Profile stiffness occurs, when the temperature profiles are limited by a critical gradient length, $L_T = T/\nabla T$, above which the heat flux rises sharply. If the temperature gradient significantly exceeds the critical value, the profiles would quickly relax towards it, leading to a "stiff" temperature profile. Experimental evidence for stiff temperature profiles has been found in several tokamak experiments [30–33].

The steep pressure gradient at the edge, however, can trigger Edge Localised Modes (ELMs). ELMs are MHD related periodic instabilities of the plasma edge [34–36], which are leading to the collapse of the pedestal and followed by a transient loss of energy and particles from the plasma. Following the crash, the pedestal recovers and rises until it reaches the associated MHD stability limit, which leads to a consecutive ELM event. The repetition rate of the ELM cycle - also referred to as ELM frequency (f_{ELM}) - is typically in the order of 10-500 Hz. The effect of ELMs on global energy confinement is limited, but the associated high heat loads onto the divertor are a major concern. The transient heat load on the divertor following the ELM crash does not cause any problem in current tokamaks, but extrapolations indicate that large ELMs on ITER could substantially exceed the limit for material damage at the divertor and significantly reduce the lifetime of the plasma facing components [37–39]. Future devices may need to utilise ELM control techniques or ELM-free scenarios [40, 41] to reduce the transient heat fluxes to a tolerable level.

ELMs can have distinct behaviours depending on the discharge conditions. Detailed comparison of different ELM types is discussed in [34]. In the present thesis only type I and type III ELMs will be discussed. Type I ELMs typically occur when the heating power sufficiently exceeds the power threshold required for H-mode. The ELM frequency increases with heating power. Type I ELMs are associated with large energy losses and, thus, large transient heat loads on plasma facing components. Type III ELMs are small, frequent ELMs occurring typically at power levels just above the LH power threshold. Their ELM frequency decreases with increasing heating power.

The edge pedestal structure determines the boundary condition for the heat transport in the plasma core. Thus, the understanding of the physical processes governing the behaviour of the edge transport barrier is crucial in order to predict the plasma performance in future devices. The physics of the pedestal in a developed H-mode regime is discussed in detail in chapter 2.

1.4 The JET tokamak with ITER-like wall

The data presented in this thesis were collected on the JET tokamak. JET is the world's largest operational tokamak. The main parameters of the device are shown in table 1.1. One of the most important features of JET is its plasma facing component configuration, the so-called ITER-like wall (ILW). The main objective for ITER is to demonstrate the scientific and technological feasibility of fusion energy as a large-scale energy source by achieving sustained burning plasma operation with 500 MW fusion power and $Q = 10$ for longer than 300 seconds. Such long-pulse and high power operation introduces new challenges related to plasma–wall interaction. This includes the control of wall power loads and material erosion, the achievement of sufficient lifetime of the plasma facing components and the problem of tritium inventory. The primary choice of plasma facing material for fusion experiments has been carbon. Carbon tolerates high heat loads and the low atomic number of carbon allows for relatively high carbon impurity concentrations in the plasma without deleterious effects. However, the use of carbon is prohibited in ITER or other future burning plasma devices due to its high tritium retention property [42]. Therefore, the choice of plasma facing component material for ITER is not carbon, but a combination of beryllium (Be) in the main chamber and tungsten (W) in the divertor [39, 43]. Tungsten has been selected due its high melting point (3695 K), while beryllium has been chosen because it has a low atomic number, thus - like carbon - it has low impact on core plasma performance.

Plasma current [44]	$\leq$ 6 MA
Magnetic field [44]	$\leq$ 4 T
Major radius	$\approx$ 2.9 m
Minor radius	$\approx$ 0.9 m
NBI heating power [45]	$\approx$ 34 MW
ICRH heating power [46, 47]	$\leq$ 10 MW

Table 1.1: Main parameters of the JET-ILW tokamak.

The JET carbon wall (JET-C) has been replaced with the ITER-like wall (JET-ILW) with remote handling between 2009 and 2011 in order to test the ITER first wall and divertor materials in terms of acceptable tritium retention and the ability to operate a large high power tokamak with metallic plasma facing components [44, 48, 49]. As shown in figure 1.7 the main chamber is made of beryllium, while the divertor comprises a combination of bulk tungsten and tungsten coated carbon fibre composite tiles. The fuel retention properties of JET-ILW fulfilled the expectations. An order of magnitude reduction has been observed in deuterium retention of the ITER-like wall compared to the carbon wall [50].

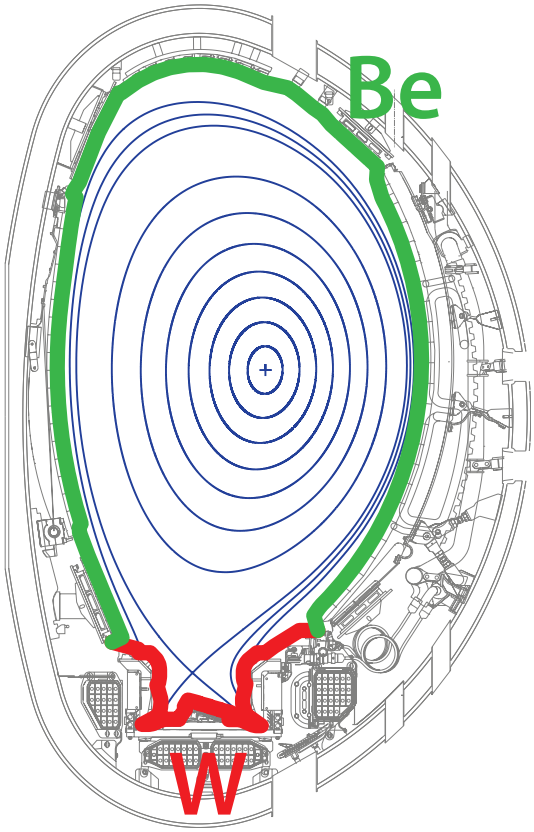

Figure 1.7: The material composition of the JET ITER-like wall. The main chamber is made of beryllium (green) and the divertor is a combination of bulk tungsten and tungsten coated carbon fibre composite tiles (red).

Beside the positive effect on fuel retention properties, the new wall material has also affected the plasma performance. A reduction in the global confinement has been observed in type I ELMy H-mode plasmas in JET-ILW compared to JET-C at low β_N ($\beta_N \sim 1.2$) [51, 52]. The confinement is affected by the requirement of an increased gas fuelling to avoid tungsten impurity accumulation in the plasma core [51, 52]. This reduction in confinement is primarily due to a degraded temperature pedestal, which in combination with core profile stiffness leads to generally lower confinement in JET-ILW than in JET-C at given input power [51–55]. Better performance at higher $\beta_N > 2$ and low gas fuelling rate was demonstrated first at low plasma current ($I_p = 1.4$ MA) [53, 56]. However, these low gas rate plasmas were prone to impurity accumulation. Good performance plasmas were also obtained in the previous experimental campaign at high plasma current ($I_p = 3.0$ MA) with increased heating power and $\beta_N \simeq 2.1$ using low injected gas fuelling rate [57, 58]. The impurity accumulation was mitigated by means of tungsten control with ICRH [59] and possibly by the combination of low gas and ELM pacing pellet injection [57, 58].

JET is the only tokamak capable of tritium operations [60]. In support of ITER, JET is currently preparing for a deuterium-tritium campaign to demonstrate fusion power generation with the ITER-like wall. Preparations include operations with H, D, T hydrogen isotopes and their mixtures, which place JET to an excellent position for studying the isotope dependence of the core and pedestal confinement.

Although considerable success has been made in the past decades, fusion energy still has a long way to go before becoming commercially available. The present thesis attempts to contribute to the understanding of the physics governing the plasma edge, which has particular importance in achieving high performance plasma operation. This work also pays special attention to the isotope dependence of the H-mode pedestal.

1.5 Motivation and thesis outline

As it will be explained in chapters 2 and 3, the global confinement in H-mode strongly depends on the pedestal performance and there is experimental evidence that the isotope mass plays an important role in the edge transport barrier. The present thesis focuses on the isotope dependence of the pedestal with the aim to make a contribution towards better understanding of pedestal and global plasma confinement and provide input for future pedestal simulation tools concerning which physics mechanisms need to be considered for accurate pedestal predictions.

The next two chapters provide the physics background for the topics discussed in this thesis. Chapter 2 discusses the physics of the H-mode pedestal, including the Peeling-Ballooning and EPED models. Chapter 3 summarises the latest developments in understanding the isotope dependence of plasma confinement.

Chapter 4 first introduces the diagnostic and analysis methods used in the present thesis and then discusses the role of the edge current evolution in the inter-ELM cycle. The saturation of the pressure gradient prior to the ELM crash has been observed in many tokamaks. This observation raises a question on the nature of the ELM trigger. A possible explanation could be a time lag in the build-up of the total edge current with respect to the pressure gradient due to current diffusion, which leads to a delay of the ELM crash. In order to test this hypothesis in JET-ILW H-mode pedestals, the time evolution of the edge current during the ELM cycle is analysed, investigating both the edge bootstrap current density profile and the Ohmic component.

From chapter 5 onward, the thesis focuses on the isotopic dependence of the H-mode pedestal. The pedestal structure, edge transport and linear MHD stability are analysed in a series of JET-ILW H and D type I ELMy H-mode plasmas. Chapter 5 introduces the data set of the JET-ILW H-modes investigated in this work and the characterisation of the pedestal structure and neutral penetration for the edge density profile are discussed.

The analysis of the pedestal structure will reveal differences between H and D plasmas, the most important of which is that the pedestal pressure is typically lower in H than in D at the same input power and fuelling gas rate, primarily due to lower density in H. Chapter 6 shows the analysis carried out to understand the changes in pedestal transport when the isotope mass is different. First, a power balance analysis is presented to compare the inter-ELM transport between H and D, followed by a study of the ELM particle losses, which could play an important role in setting the lower density in the H pedestals. Interpretative simulations with EDGE2D-EIRENE, a two-dimensional plasma fluid code coupled to a kinetic Monte Carlo code for the neutrals are also presented for better understanding of the edge transport and neutral penetration.

In chapter 7, the isotope dependence of pedestal stability is investigated. The potential effect of the change in isotope mass on the bootstrap current is discussed. The isotope dependence of linear MHD stability, introduced through diamagnetic stabilisation, is examined with the HELENA equilibrium and ELITE ideal MHD stability codes. The sensitivity of pedestal stability on the separatrix temperature is also discussed. The conclusions and future work are presented in chapter 8.

Chapter 2

Physics of the H-mode pedestal

Physics-based modelling is essential to predict plasma performance beyond the current experiments and optimise the plasma confinement. As briefly discussed in the previous chapter, the pedestal structure determines the boundary condition for the core plasma transport. Thus, integrated simulation tools require predictive capabilities for the pedestal structure. This motivates the understanding of the physics governing the pedestal.

The H-mode pedestal is governed by at least three interacting processes: pedestal stability, transport and sources. The stability of the pedestal is generally described by MHD theory. The high pressure gradient and the edge current density at the edge drive MHD modes unstable, which limit the maximum achievable pedestal pressure. In order to reach high pedestal pressure - and thus maximising global confinement and fusion gain - several plasma parameters need to be optimised to extend the limits posed by MHD instabilities. H-modes with so called "type I ELMs" are the most common high confinement regimes in current tokamaks. This regime provides good confinement and there is good confidence that the regime can be accessed in ITER, where it has been chosen as the reference operating scenario [61]. It is widely accepted that type I ELMs are an MHD related phenomenon and the stability of the pedestal in a type I ELMy regime can be explained by the peeling-ballooning (P-B) model [62, 63], which is discussed in section 2.1 in detail.

The crash following the trigger of the ELM is a transient event ($\sim 0.1 - 1$ ms), where significant amount of energy (5-30 % of the energy stored in the pedestal) is lost from the confined region and transported to the SOL towards the plasma facing components. The ELM crash is responsible for up to 1/3 of the total plasma transport in the pedestal. Non-linear MHD theory would be required to predict the heat and particle fluxes during the ELM crash. This is beyond the scope of the present thesis,

but experimental characterisation of the ELM losses in JET-ILW Hydrogen (H) and Deuterium (D) H-modes is discussed in chapter 6.

The inter-ELM evolution of the temperature pedestal between two ELM events is determined by the balance of the pedestal transport and the heat reaching the pedestal from the core. The particle channel behaves somewhat differently. Beyond the particle source from the core, which is typically provided by fuelling due to NBI, the ionisation of neutral atoms penetrating into the pedestal is also important. Neutrals are injected into the vacuum chamber for fuelling purposes or recycled from the walls. The constraints provided by inter-ELM transport and stability together define the maximum achievable pedestal height. Inter-ELM transport is introduced in more detail in section 2.3.

The pedestal structure is usually characterised by the pedestal height, width and gradient as illustrated in figure 2.1 for the pressure. Similarly to the pressure, the width and height can also be defined for the density and temperature. The pedestal height is an essential parameter to set the boundary condition for core transport modelling. The average pedestal pressure, density or temperature gradient is often estimated by ratio of the height and width of the pedestal.

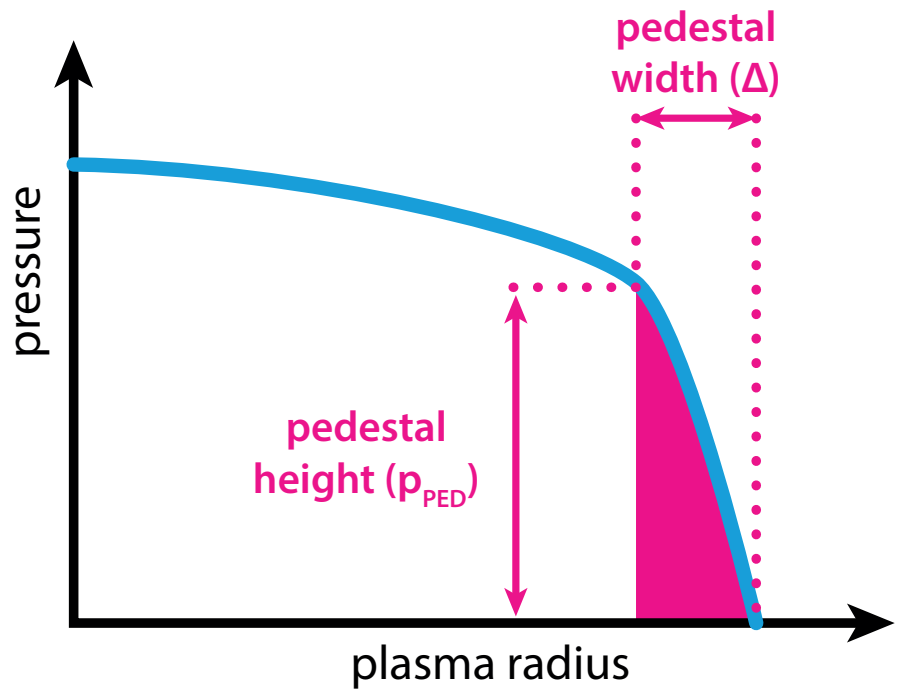

Figure 2.1: Illustration of the width and height of the pedestal.

2.1 The Peeling-Ballooning model

The trigger of type I ELMs can be understood by means of the P-B model, which is based on ideal MHD theory. The MHD equations provide a single fluid description of the plasma [13]:

$$\frac{\partial \rho}{\partial t} + \nabla \cdot (\rho \mathbf{v}) = 0 \ , \tag{2.1}$$

$$\rho \frac{\mathrm{d}\mathbf{v}}{\mathrm{d}t} = \mathbf{J} \times \mathbf{B} - \nabla p \ , \tag{2.2}$$

$$\frac{\mathrm{d}}{\mathrm{d}t}\left(\frac{p}{\rho_\gamma}\right) = 0 \ , \tag{2.3}$$

where ρ is the mass density, $\mathbf{v}$ is the fluid velocity, p is the pressure, $\mathbf{J}$ is the current density, $\mathbf{B}$ is the magnetic field, γ is the ratio of specific heats and $\mathrm{d}/\mathrm{d}t = \partial/\partial t + \mathbf{v} \cdot \nabla$ is the convective derivative.

Eq. (2.1) is the continuity equation describing the conservation of mass. Atomic processes which could act as a source or sink for the particles are negligible in the MHD time scale. The momentum equation (eq. (2.2)) describes the balance between the inertial force $\rho \mathrm{d}\mathbf{v}/\mathrm{d}t$, the magnetic force $\mathbf{J} \times \mathbf{B}$ and the pressure gradient ∇p. The energy equation (eq. (2.3)) expresses an adiabatic evolution of the plasma. To obtain the final set of MHD equations, the above three need to be completed with the low-frequency Maxwell equations and with Ohm's law:

$$\mathbf{E} + \mathbf{v} \times \mathbf{B} = 0 \ , \tag{2.4}$$

where $\mathbf{E}$ is the electric field. Adding $\eta \mathbf{J}$ on the right-hand side of eq. (2.4), resistivity (η) could be introduced in the system, leading to resistive MHD. In ideal MHD, the plasma is a perfect conductor, $\eta = 0$.

There are two important assumptions, which are required to derive the MHD equations from the two-fluid equations [64]. First, the vacuum permittivity is eliminated in the Maxwell equations ($\epsilon_0 \to 0$), which means that the displacement current $\epsilon_0 \partial \mathbf{E}/\partial t$ and the net charge $\epsilon_0 \nabla \cdot \mathbf{E}$ are neglected. This leads to the low-frequency Maxwell equations. The neglect of $\epsilon_0 \partial \mathbf{E}/\partial t$ implies the local quasineutrality of the plasma: $n_i = n_e \equiv n$, where n_i and n_e are the ion and electron densities, respectively. The second assumption is that on MHD time scales, the electrons have an infinitely fast response due to their relatively small mass. Formally this means that the electron inertia is neglected: $m_e \to 0$.

The static ($\mathbf{v} = 0$), steady state ($\partial/\partial t = 0$) solution of the MHD equations provide the equilibrium in a given geometry. In a two-dimensional axisymmetric toroidal geometry, the equilibrium is described by the Grad-Shafranov equation [65, 66]. In practical applications the Grad-Shafranov equation is solved numerically to obtain the experimental or model equilibria. Free boundary equilibrium codes solve the Grad-Shafranov equation in an iterative way to find an equilibrium that best matches the magnetic measurements and possibly other constraints on the pressure and current profiles. Fixed boundary equilibrium solvers require the plasma boundary as input and typically use constraints on the pressure profile and complex models for the parallel current density.

For a given equilibrium, the next question to ask is whether the equilibrium is stable or unstable. The simplest way to evaluate the stability of a given MHD equilibrium is to study its linear stability. Linear stability can be examined by applying a small perturbation to the system in the form of a plasma displacement. If the displacement leads to a restoring force, then the equilibrium is stable and the result - in the absence of damping in ideal MHD - is an oscillation around the equilibrium. If the resulting force enhances the initial perturbation, then the equilibrium is unstable and the displacement grows indefinitely. This linear approach is useful to examine the stability of the system. In order to obtain the behaviour of any instability away from the equilibrium, non-linear theory is needed. Non-linearly, instabilities can reach a saturated state (for e.g. turbulence driven micro-instabilities) or exhibit an explosive behaviour (for e.g. ELMs), where linear theory is not applicable anymore.

In linear MHD stability analysis, the primary interest is typically to determine whether the equilibrium is stable or unstable and the precise value of the growth rate of unstable modes is not important. Thus, MHD codes typically adopt the formulation known as the Energy Principle [13, 67]. It is a simple and convenient way to determine the stability of MHD modes and it provides a reasonable estimate for the MHD growth rate. The derivation of the Energy Principle formulation starts with expressing all perturbed quantities in terms of the displacement of a plasma fluid element, $\boldsymbol{\xi}(\mathbf{x}, t)$. A perturbation to $\boldsymbol{\xi}$ is applied in the form of a Fourier harmonic: $\boldsymbol{\xi} = \boldsymbol{\xi}(\mathbf{x}) \exp(i\omega t)$. Substituting the perturbed displacement into the MHD equations leads to:

$$\rho_0 \frac{\partial^2 \boldsymbol{\xi}}{\partial t} = \mathbf{F}(\boldsymbol{\xi}) \ , \tag{2.5}$$

where $\mathbf{F}(\boldsymbol{\xi})$ is the MHD force operator:

$$\mathbf{F}(\boldsymbol{\xi}) = \frac{1}{\mu_0}(\nabla \times \mathbf{B_0}) \times \mathbf{B_1} + \frac{1}{\mu_0}(\nabla \times \mathbf{B_1}) \times \mathbf{B_0} + \nabla(p_0 \gamma \nabla \cdot \boldsymbol{\xi} + \boldsymbol{\xi} \cdot \nabla p_0) \ . \tag{2.6}$$

In eq. (2.6) the zero subscript denotes the equilibrium quantities. The perturbed magnetic field, $\mathbf{B_1}$ still appears in the MHD force operator, but it can be substituted with $\boldsymbol{\xi}$ using:

$$\mathbf{B_1} = \nabla \times (\boldsymbol{\xi} \times \mathbf{B_0}) \ . \tag{2.7}$$

Using the Fourier decomposition of the perturbation allows to express eq. (2.5) as an eigenvalue problem:

$$-\omega^2 \rho_0 \boldsymbol{\xi} = \mathbf{F}(\boldsymbol{\xi}) \ , \tag{2.8}$$

where ω is the mode frequency.

Multiplying eq. (2.8) with $\boldsymbol{\xi}^*$ and integrating over the plasma volume V leads to the following form, which allows the use of the Energy Principle:

$$\omega^2 = \frac{\delta W(\boldsymbol{\xi}^*, \boldsymbol{\xi})}{K(\boldsymbol{\xi}^*, \boldsymbol{\xi})} \ , \tag{2.9}$$

$$\delta W = -\frac{1}{2} \int_V \boldsymbol{\xi}^* \cdot \mathbf{F}(\boldsymbol{\xi}^*) \mathrm{d}V \ , \tag{2.10}$$

$$K = \frac{1}{2} \int_V \rho |\boldsymbol{\xi}^*|^2 \mathrm{d}V \ . \tag{2.11}$$

K is the kinetic energy of the system and δW is the potential energy.

Assuming that the plasma is surrounded by a vacuum region and a conducting wall, the potential energy can be written in the following intuitive form:

$$\delta W = \delta W_F + \delta W_S + \delta W_V \ , \tag{2.12}$$

where

$$\delta W_F = \frac{1}{2} \int_{\text{Fluid}} \left[\frac{|B_{1\perp}|^2}{\mu_0} + \frac{B_{0\perp}^2}{\mu_0} \left| \nabla \cdot \boldsymbol{\xi}_\perp + 2 \boldsymbol{\xi}_\perp \cdot \boldsymbol{\kappa} \right|^2 + \right.$$
$$\left. + \gamma p \left| \nabla \cdot \boldsymbol{\xi} \right|^2 - 2(\boldsymbol{\xi}_\perp \cdot \nabla p)(\boldsymbol{\kappa} \cdot \boldsymbol{\xi}_\perp^*) - j_\parallel (\boldsymbol{\xi}_\perp^* \times \mathbf{B_0}) \cdot \mathbf{B_1} \right] \mathrm{d}V \ , \tag{2.13}$$

is the fluid contribution with $\boldsymbol{\kappa}$ the curvature vector of the equilibrium magnetic field: $\boldsymbol{\kappa} = \mathbf{B}/B \cdot \nabla(\mathbf{B}/B)$.

$$\delta W_S = \frac{1}{2} \int_{\text{Surface}} \left| \mathbf{n} \cdot \boldsymbol{\xi}_\perp \right|^2 \mathbf{n} \cdot \left[\nabla \left(p_0 + \frac{B_0^2}{2\mu_0} \right) \right] \mathrm{d}S \ , \tag{2.14}$$

is the surface contribution with $\mathbf{n}$ the normal vector on the surface and

$$\delta W_V = \frac{1}{2} \int_{\text{Vacuum}} \frac{|B_1|^2}{\mu_0} \mathrm{d}V \ . \tag{2.15}$$

is the vacuum contribution.

As the force operator is self-adjoint [13], the eigenvalues ω^2 are real and the stability properties are as follows: if the potential energy (δW) of the system is negative for any displacement then the equilibrium is unstable as the perturbation moves the plasma to a more favourable state. Positive δW indicates a stable equilibrium.

Eq. (2.13) shows the fluid term δW in a form that allows the interpretation of the different terms [67]. The first three terms are positive and thus stabilising. The first term is related to the Shear Alfven wave, the second is related to the compressional Alfven waves and the third term is related to the sound waves. The last two terms can either be negative or positive, thus these are the potential sources of instability. The sources of free energy to drive unstable modes are the pressure gradient and the parallel current density, respectively.

First, the pressure-driven instabilities are discussed. The sign of the fourth term in eq. (2.13) depends on the relative alignment of the pressure gradient and the curvature. In the inboard side of the torus (it is also called the high field side (HFS) due to the higher toroidal magnetic field) ∇p and $\boldsymbol{\kappa}$ point to opposite directions, thus the curvature is stabilising. This is why the HFS is also referred to as the "good curvature" region. On the outboard side of the torus (low field side - LFS, "bad curvature" region), ∇p and $\boldsymbol{\kappa}$ point to the same direction, in which case term 4 is negative. This could lead to conditions where the stabilising effect from magnetic field line bending cannot compensate for the destabilising pressure gradient. The so-called ballooning modes are pressure-driven instabilities, which are concentrated in regions with the least favourable magnetic curvature, thus on the outboard side of the tokamak.

Besides the pressure gradient, the parallel current density is also a source of free energy. The current density at the edge is usually dominated by the bootstrap current, which can be efficiently driven by the steep pressure gradient. Figure 2.2 sketches the

edge current density profile at the plasma edge. The physical mechanism of the bootstrap

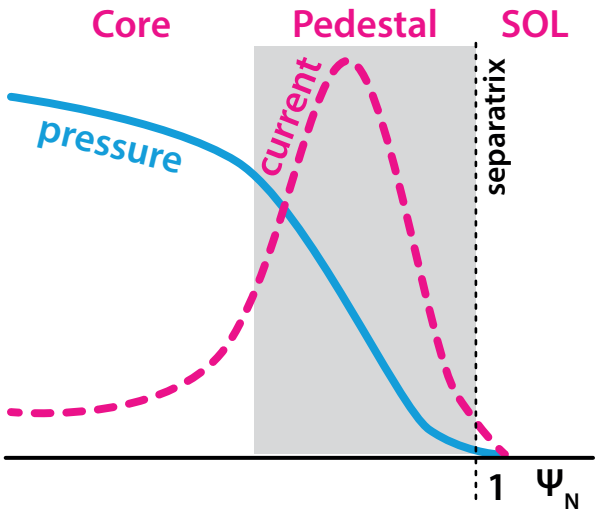

Figure 2.2: The edge current density is usually dominated by the bootstrap current, which can be efficiently driven by the steep pressure gradient.

current is described here based on Peeters's work [68]. In a tokamak, due to the radial gradient in the magnetic field, particles with low enough parallel velocity ($v_{\|}$) follow banana orbits. When the particle moves from the LFS to the HFS, it experiences a magnetic mirror effect and its $v_{\|}$ is decreasing. If $v_{\|}$ becomes zero, the particle gets reflected. These particles are called trapped particles and they bounce backwards and forwards around the outboard side of the plasma. Due to the drifts in the plasma, particles are moving up- and down when they are moving relative to the magnetic field gradient. As a result, the shape of the particle orbit is "banana shaped" in the poloidal cross-section, as shown in figure 2.3.

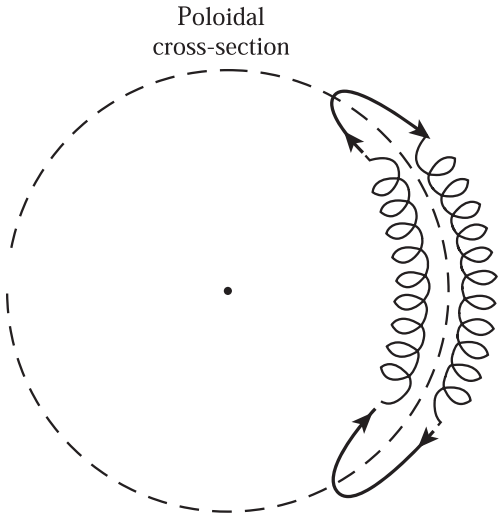

Figure 2.3: A trapped particle orbit projected onto the poloidal plane. Figure is adapted from [69].

Two trapped ions at a given flux surface with opposite sign of parallel velocity are drifting to opposite directions: one drifts inwards, while the other drifts outward. If a density gradient exists in the plasma, the number of trapped particles populating the orbit drifting inward is higher than the number of trapped particles populating the orbit drifting outward. As a consequence, there will be a net flow of ions in the toroidal direction. As electrons drift in the opposite direction, the net toroidal flow of electrons points to the opposite direction, leading to a net toroidal current. This toroidal current is called the banana current and it serves a seed current for the bootstrap current. The main part of the bootstrap current is carried by the passing particles and is generated through collisional coupling of trapped and passing particles.

The last term of eq. (2.13) describes the current driven modes, which are also called kink modes. These modes are primarily driven by the parallel current density. The name arises from the nature of this instability, such as it deforms the plasma into a kink shape. The so-called peeling mode, which is important for the stability of the pedestal, is a limit of the kink mode when the current gradient is infinitely large over an infinitesimally small region at the plasma boundary [70]. Intuitively, the peeling mode is strongly localised at the edge, and is driven by the rapid change in parallel current across the separatrix. It is also important to note that the kink drive is negligible at large toroidal mode number (n), but the peeling drive is not.

Eqs. (2.12)-(2.15) are very complex and simplified numerical approaches are required to investigate the stability in experimental cases with realistic geometry. Local, high-n treatment of the problem allows to examine the behaviour of peeling and ballooning modes [71, 72], the two instabilities, which are associated with ELMs. Such an approach implies that the main drive for the ballooning modes is the pressure gradient, while the current density can stabilise ballooning modes through reduced magnetic shear. The magnetic shear is the variation in the field pitch angle between flux surfaces: $s = \mathrm{d}\ln(q)/\mathrm{d}r$, where q is the safety factor.

The local, high-n limit of MHD modes can easily be calculated, but in a realistic pedestal finite Larmor-radius effects stabilise high-n modes and the pedestal is typically limited by finite-n modes. These modes are radially extended enough that different poloidal harmonics may couple to each other. Furthermore, peeling and ballooning modes may couple leading to the so-called coupled peeling-ballooning (P-B) modes, which have enough radial extent to affect the whole pedestal.

To calculate the stability of P-B modes in the pedestal, first an equilibrium is needed that matches the actual plasma as closely as possible (the operational point or OP). The

growth rate (γ_{MHD}) for a range of toroidal mode numbers can then be calculated. The equilibrium is stable if the growth rate is 0 for all mode numbers and unstable if there is any non-zero growth rate. In numerical stability codes the stability criterion is often set as a small proportion of the Alfven-frequency $\gamma_{\mathrm{MHD}} > c \times \omega_A$, instead of $\gamma_{\mathrm{MHD}} > 0$. c is typically $\approx 0.02 - 0.05$ and $\omega_A = B_0/(R_0\sqrt{4\pi\rho_0})$ with ρ_0 the mass density. Using such a stability criterion, the stability of the pedestal can then be mapped around the operational point as a function of the normalised pressure gradient and the edge current density, which are the two main drives of P-B modes. A detailed description of the analysis method can be found in [73]. New, perturbed equilibria are generated by multiplying the pressure and current density profiles of the operational point with a Gaussian function that is centred in the middle of the pedestal and has the same width as the pedestal. The stability of these perturbed equilibria is then evaluated and visualised on the $j-\alpha$ space, as illustrated in figure 2.4. j corresponds to the maximum normalised current density in the edge and α is the normalised pressure gradient as defined in [74]:

$$\alpha = \frac{-2\partial V/\partial\Psi}{(2\pi)^2}\left(\frac{V}{2\pi^2 R_0}\right)^{1/2}\mu_0\frac{\partial p}{\partial\Psi}\ , \tag{2.16}$$

where V is the volume enclosed by the flux surface, R_0 is the geometric centre of the plasma and Ψ is the poloidal flux. The pink solid line in figure 2.4 is the P-B stability boundary as defined by the applied stability criterion. The area below the pink curve is the stable region, everything outside is linearly unstable. At low current and high α, high n ballooning modes are dominant, while at low α and high current low n peeling modes are more unstable. Mid-n, coupled P-B modes are typically unstable at the "nose" of the P-B stability boundary. As indicated with the black arrows, in this model the pedestal builds up in the recovery phase and hits the stability boundary just before the type I ELM crash. The operational point of the so-called pre-ELM pedestal is indicated with the cyan star. Note that in a realistic case the P-B boundary is not fixed during the inter-ELM phase, but evolves as the plasma equilibrium changes.

In an ideal case, the OP of a pre-ELM pedestal is at or close to the stability boundary. However, due to uncertainties either in α, j or the underlying plasma equilibrium, the OP can be either in the stable or unstable side of the boundary. Inaccuracies in the equilibrium reconstruction typically arise from the uncertainties of the magnetic measurements, which are affected by slow data acquisition and the screening of the vacuum vessel and other conducting structures. The equilibrium is also affected by the chosen set of additional constraints on the pressure and current profiles and their uncertainties. α is generally

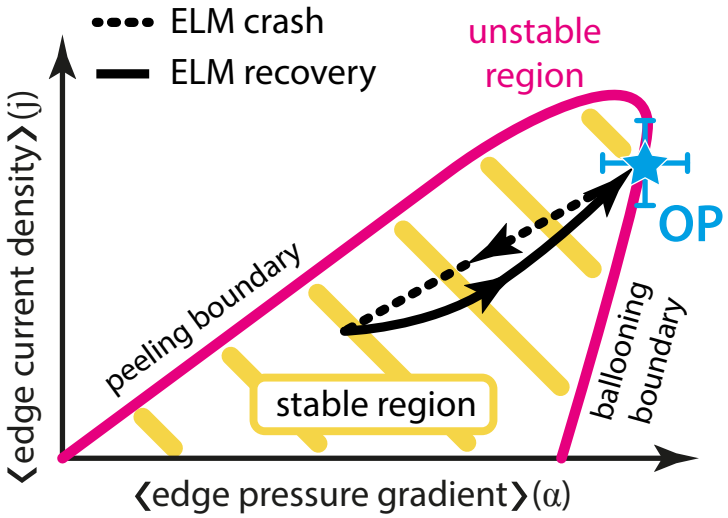

Figure 2.4: Peeling-Ballooning stability diagram of the pedestal. The operational point (cyan star) is shown as a function of j and α. The stability boundary is in magenta. The black arrows represent the ELM cycle.

affected by the uncertainty of the kinetic profile measurement and the regularisation introduced by the profile fit. In most tokamaks there is no reliable edge current density measurement, thus j is typically estimated using bootstrap models. Accuracy of j relies on the uncertainty of the kinetic profiles, the equilibrium, the validity of the bootstrap current model and the assumption on the electric field profile for the Ohmic current.

In order to quantify the proximity of the OP to marginal stability, the pedestal temperature is scaled up and down with respect to the operation point, which provides a scan in ∇p. ∇p which is closest to marginal stability is called the critical pressure gradient. The ratio of the critical and the experimental ∇p provides a measure to quantify the stability of the pedestal [73, 75]. This method can also be used to determine the maximum pedestal height for a given pedestal width. In order to simultaneously predict the width and height of the pedestal another constraint is required.

2.2 The EPED model

The EPED [76, 77] model provides predictions for both the height and the width of the pedestal in a type I ELMy regime. According to this model, the pedestal is limited by two instabilities, namely the kinetic ballooning modes (KBMs) and P-B modes. KBM is a micro-instability, which can be described by introducing kinetic effects in the high-n ideal ballooning MHD formalism [78]. Although the suppression of micro-instabilities via sheared $\mathbf{E} \times \mathbf{B}$ flows at the edge of the plasma plays an important role in the formation of the edge transport barrier, KBMs are not entirely suppressed [76]. It has been found in

gyrokinetic simulations that the onset of the KBM instability is highly stiff [79, 80], i.e. the mode growth rate increases quickly above the stability threshold, and that the stability threshold of the KBM is close to that of the $n = \infty$ ideal ballooning mode [81, 82]. Due to the stiff onset and the insensitivity to $\mathbf{E} \times \mathbf{B}$ shear, KBM is proposed as a gradient limiting instability in pedestal inter-ELM evolution.

The pedestal evolution during the type I ELM cycle according to the EPED model assumption is illustrated in figure 2.5. After the ELM crash, the pedestal starts to build up and is first limited by KBMs (arrow 1 in figure 2.5). The KBM is a nearly local mode, which constrains the pressure gradient. In the EPED model the pedestal width can further widen (with a limited gradient), until the P-B mode is triggered (arrow 2 in figure 2.5). This leads to the crash and the pedestal collapses (arrow 3 in figure 2.5).

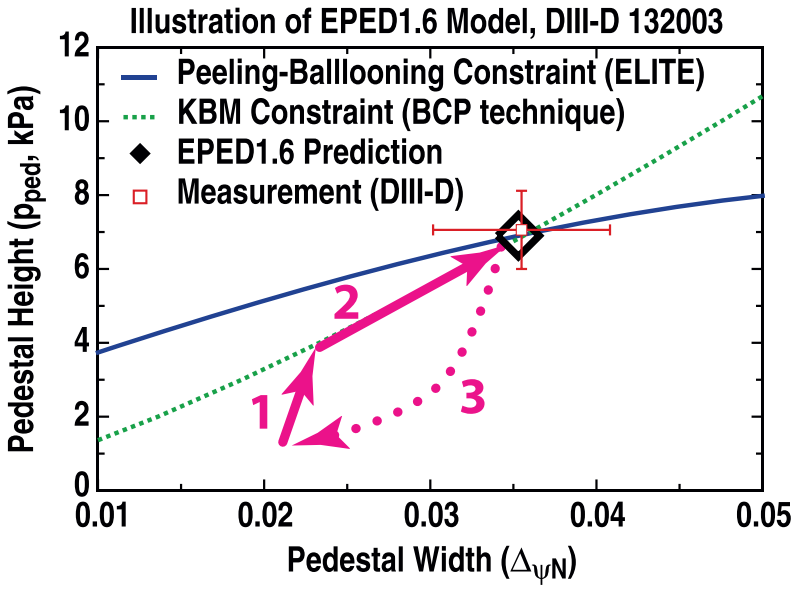

Figure 2.5: Evolution of the pedestal according to the EPED model assumptions. Figure is adapted from [77].

The EPED model predicts the pedestal pressure height with the following inputs: the toroidal magnetic field, the plasma current, the major radius, the minor radius, the plasma triangularity and elongation, the pedestal density and the global β. These parameters are used to construct a series of model equilibria with different pedestal widths. As shown in figure 2.5, the stability of KBMs and P-B modes are evaluated for each pedestal width to obtain the critical pedestal height. The intersection of the two curves representing the stability constraints gives the EPED prediction for the height and width.

EPED does not calculate the KBM stability directly using gyrokinetic codes, but uses a proxy to estimate the limit posed by KBMs. One approach is based on the experimental evidence (originating from data at DIII-D) that there is a strong correlation between the pedestal width and pedestal poloidal beta ($\beta_{\mathrm{pol,PED}}$). $\beta_{\mathrm{pol,PED}}$ is the ratio of the pedestal

pressure and the energy of the poloidal magnetic field:

$$\beta_{\mathrm{pol,PED}} = \frac{p_{\mathrm{PED}}}{B_p^2/2\mu_0} \ . \tag{2.17}$$

Based on the sensitivity of KBM stability on the magnetic shear, a heuristic scaling for the pedestal pressure width is introduced in [76]:

$$\Delta_\Psi = c_{\mathrm{EPED}} \cdot \sqrt{\beta_{\mathrm{pol,PED}}} \ , \tag{2.18}$$

where Δ_Ψ is measured in Ψ_N and is estimated as the average of the density and temperature pedestal widths ($\Delta_\Psi = \Delta n_e/2 + \Delta T_e/2$) and $c_{\mathrm{EPED}} = 0.076$ is a constant obtained from a fit on experimental DIII-D data [76]. There is also significant experimental evidence from other tokamaks that $\Delta_\Psi \sim \sqrt{\beta_{\mathrm{pol,PED}}}$ [83–87]. An other approach to estimate the KBM stability is evaluating the stability of the $n = \infty$ ideal ballooning mode. With the so-called ballooning critical pedestal (BCP) technique [77], the edge pressure gradient is taken to be critical, when the central half of the pedestal is unstable to the $n = \infty$ ideal ballooning mode.

Although the EPED model has successfully reproduced the experimentally observed parameters of the pedestal in many studies [77, 86, 88, 89], there are examples, where the EPED width scaling is not fully consistent with experimental observations. Many studies have reported that the pedestal width increases with increasing gas rate at fixed $\beta_{\mathrm{pol,PED}}$ in JET-ILW H-modes [53, 54, 90, 91]. These observations suggest that the pedestal transport assumption of EPED (i.e. KBMs are limiting the pedestal gradient) may not be valid in all experimental conditions. Gyrokinetic simulations of H-mode pedestals in different tokamaks have shown that other microinstabilities could also be unstable in the edge transport barrier. These are discussed in section 2.3 in more detail.

Furthermore, the EPED model is not fully predictive as it requires the global β and the pedestal density as input. These two parameters, however, are not known prior to the experiment. The use of the global β for the pedestal prediction can be eliminated by the use of integrated core-pedestal modelling [75, 92–96]. With this approach the global β can be replaced by the heating power as input, which is known in advance of the experiment. The global β can be predicted using core transport models, which however require the pedestal density and temperatures as a boundary condition. As the pedestal stability is affected by the global β, the core and edge parts of the simulations needs to be executed in an iterative way. First the core transport model can be run assuming an initial guess for the pedestal parameters. The global β output can then be used for

the pedestal prediction providing the boundary condition for the core transport. This process is then continued until the edge and core solutions are converged and provide a self-consistent prediction for the global confinement.

The other input to the EPED model that is not known prior to the experiment is the pedestal density. In some circumstances the density can be controlled with pellets or gas fuelling, however this is not always the case. For example, in JET-ILW high triangularity plasmas, the gas fuelling has very little effect on the pedestal density [90]. Also, the gas fuelling rate may need to be specified to control the ELM frequency avoiding high Z impurity accumulation in the core plasma. Thus, for a fully predictive pedestal model, the pedestal density needs to be predicted. One approach, which is used to predict the pedestal density is based on the Neutral Penetration Model (NPM) [97]. This model assumes that the pedestal density is set by the edge particle flux and that the pedestal width is proportional to the neutral penetration length. As the mean free path of the neutrals is different with different isotope mass, due to the different velocities at the same temperature, a difference in neutral penetration is expected between H and D plasmas. The isotope dependence of the neutral penetration is investigated experimentally and with edge transport simulations in sections 5.4 and 6.3, respectively.

2.3 Inter-ELM pedestal transport

Although the formation of the pedestal is associated with a strong reduction of turbulent transport at the plasma edge, the remaining residual transport has a fundamental role in defining the pedestal structure. The inter-ELM transport determines the trajectory of the density and temperature profiles evolution prior to the ELM crash and thus it ultimately defines the operating point at which the plasma becomes unstable to peeling-ballooning modes. The heat source in the pedestal is given by the outward heat flux from the core, while the density pedestal is maintained by particle flux from NBI in the core, ionisation of neutral particles from the edge and, possibly, a turbulent particle pinch.

As it has been discussed in the previous section, the EPED model assumption is that the dominant microinstability responsible for the residual transport in the edge transport barrier is the KBM. Several studies utilising linear and nonlinear global gyrokinetic simulations emphasise the role of other microinstabilities in the pedestal of JET-ILW plasmas [82, 98–102]. The most recent analyses [101, 102] point out that in typical JET-ILW plasmas the ratio of the electron heat diffusivity ($\chi_e = Q_e/\nabla T_e$, with Q_e the electron heat transits) far exceeds the particle diffusivity ($D = \Gamma/\nabla n$, with Γ the

particle flux), implying that the particle source is small compared to the heat flux from the core[1] [102, 103]. In the case of a small particle source, MHD-like instabilities (like KBM) would mostly impact the particle transport as they produce equal diffusivities in both the particle and heat transport channels. Thus, other microinstabilities such as electron temperature gradient modes (ETGs), ion temperature gradient modes (ITG) or microtearing modes (MTMs) are likely to be responsible for dominating the heat transport. For example, the degradation of the temperature pedestal in JET-ILW (where significant gas injection is needed for core W control) in comparison to JET-C can partly be explained by more robust ITGs and ETGs in the JET-ILW pedestal, leading to limited pedestal temperature and demanding more heating power to achieve similar pedestal pressure compared to JET-C [99, 102]. These new results do not necessarily contradict the EPED model. KBMs could clamp the pressure gradient by acting on the density, but not contribute much to the heat transport [102]. In the present thesis, the EPED width scaling will be discussed in view of the pedestal structure analysis of JET-ILW plasmas and the inter-ELM transport is analysed experimentally by means of a power balance analysis, but the isotope effect on KBMs and other microinstabilities in the pedestal is beyond the scope of this work.

[1] The use of effective diffusivities in this manner assumes neither the absence of pinches nor the absence of nonlocal effects, but is, rather, a convenient measure of the gradient that can be supported by a given flux or source.

Chapter 3

Isotope dependence of plasma confinement

In order to predict the performance of burning plasma experiments, it is particularly important to understand how the isotope mass of the fuel affects the plasma transport and confinement. In present tokamaks typically pure deuterium plasmas are examined. As most of the existing data was collected in deuterium experiments, the majority of the current models and simulations are optimised and/or validated with deuterium only plasmas. However, the isotope composition will be changed to a deuterium-tritium (DT) mixture for future fusion plasmas such as JET-DTE2 [46, 58] and ITER [22]. Although a positive isotope mass scaling of the thermal energy confinement time in H-mode plasmas has been observed in several tokamaks such as JET [104], JT-60U [83, 105, 106], DIII-D [107], ASDEX [108, 109] and ASDEX-Upgrade [110], this favourable isotope dependence has not yet been fully understood theoretically. This chapter summarises the current understanding on the isotope dependence of confinement in tokamak plasmas.

3.1 Isotope dependence of global confinement

An overview on the effect of isotope mass on confinement can be gained from scaling laws. Scaling laws are developed to provide an empirical prediction for the performance of new devices. These are based on data regression of large amounts of data collected in several different tokamak experiments, but do not rely on any fundamental laws of physics. The most widely used scaling for the thermal energy confinement time ($\tau_{\mathrm{E,th}}$) of ELMy H-modes is the so called IPB98(y,2) scaling [111, 112]:

$$\tau_{\mathrm{E,th}} = 0.0562 \times A^{0.19} I_p^{0.93} B_T^{0.15} P_{\mathrm{abs}}^{-0.69} n^{0.41} R^{1.97} \epsilon^{0.58} \kappa^{0.78} \ , \tag{3.1}$$

where $\tau_{\mathrm{E,th}}$ is measured in [s], A is the effective isotope mass ($A = m_{\mathrm{ion}}/m_{\mathrm{proton}}$), I_p is the plasma current in [MA], B_T is the toroidal magnetic field in [T], P_{abs} is the absorbed power in the plasma [MW], n is the averaged plasma density in [10^{19} m^{-3}], R is the plasma major radius in [m], ϵ is the inverse aspect ratio ($\epsilon = a/R$) and κ is the elongation. The experimental thermal energy confinement is often normalised to the scaling law prediction. This parameter is called the H-factor: $H_{98} = \tau_{\mathrm{E,th}}/\tau_{\mathrm{IPB98(y,2)}}$. The IPB98(y,2) scaling is based on data collected from 11 different tokamaks and it shows a positive isotope scaling ($\sim A^{0.19}$) of the thermal energy confinement time. The energy confinement in most of the H-mode experiments is in qualitative agreement with the positive isotope mass dependence appearing in the IPB98(y,2) scaling [104, 106–110].

The plasma transport in the core of a tokamak plasma is typically dominated by turbulent fluctuations on the scale of the ion Larmor radius [113]. Simple random walk estimates of the turbulent transport results in the so-called gyro-Bohm scaling of the local heat transport [114, 115]:

$$\chi_{\mathrm{gyro-Bohm}} = \rho^* \cdot \chi_{\mathrm{Bohm}} \ , \tag{3.2}$$

where $\chi_{\mathrm{gyro-Bohm}}$ is the gyro-Bohm heat diffusivity, ρ^* is the ion Larmor radius normalised to the plasma minor radius and χ_{Bohm} is the Bohm heat diffusivity: $\chi_{\mathrm{Bohm}} \sim T/eB$ [23]. As ρ^* scales as $\rho^* \sim \sqrt{A}$, the Gyro-Bohm scaling predicts an unfavourable dependence of local transport on isotope mass:

$$\chi_{\mathrm{gyro-Bohm}} \sim \sqrt{A} \ . \tag{3.3}$$

In ideal circumstances (such as fixed density, temperature, heating and fuelling profiles), this leads to [116]:

$$\tau_{\mathrm{E,th}} \sim \frac{1}{\sqrt{A}} \ , \tag{3.4}$$

which implies that the energy confinement time should decrease with increasing isotope mass. However, this simplistic picture does not capture all elements of the underlying physics mechanisms and theory predicts that gyro-Bohm scaling breaks in many different ways.

One mechanism, which can break up the effect of local gyro-Bohm heat transport on a global scale is profile stiffness. Due to profile stiffness, even in the case of the local heat transport being gyro-Bohm ($\chi \sim \sqrt{A}$), the global energy confinement time does not necessarily follow the gyro-Bohm scaling ($\tau_{\mathrm{E,th}} \sim 1/\sqrt{A}$), but Bohm or nearly Bohm

scaling instead [117]. Modelling the core transport of JET-ILW L-mode plasmas with the TGLF quasi-linear turbulence code [118, 119] demonstrated that stiffness can overcome the local gyro-Bohm scaling, which explains the absence of isotope mass dependence of energy confinement in the plasma core for the investigated H and D JET-ILW L-mode plasmas [120]. Note that the isotope dependence of τ_E in L-modes is generally found to be weaker than in H-modes [104, 109, 121, 122].

The plasma heating mix is another important factor when the isotope effect is studied. A favourable isotope dependence on the global confinement in ECRH heated L-mode plasmas on ASDEX-Upgrade could be explained by the isotope mass dependence of the collisional electron-ion energy heat exchange [121]. The heat exchange between ions and electrons due to collisions depends on the ion mass (m_i) [7]: $P_{ei} \propto Z^2 n^2 (T_e - T_i)/(m_i T_e^{3/2})$. As a result, the additional electron heating in H was transported by the ion channel in the cited ASDEX-Upgrade L-modes. Transport simulations with the same transport coefficients for H and D (thus, the ion mass only appears in the energy exchange term) could explain the lower energy confinement time in H and the experimental kinetic profiles could be reproduced [121]. The inverse mass dependence of the energy exchange term also plays a role in the weak, but favourable isotope dependence of τ_E in JET-ILW Ohmic plasmas [123, 124].

The gyro-Bohm scaling of local heat transport is confirmed by gyrokinetic simulations for electrostatic fluctuations with adiabatic electrons, no collisions and no background flows [125], but any departure from these assumptions could modify the mass scaling. The electromagnetic stabilisation of ITGs can be stronger at higher isotope mass [126]. Similarly, the effect of $\mathbf{E} \times \mathbf{B}$ flow shear ($\gamma_{\mathbf{E}\times\mathbf{B}}$), which is known to suppress ITG turbulence [127], can have a stronger impact with increasing isotope mass, because $\gamma_{\mathbf{E}\times\mathbf{B}}$ has no dependence on A, while the ITG growth rate scales as $\gamma_{\mathrm{ITG}} \sim A^{-1/2}$ for same kinetic profiles [128]. Thus, the $\mathbf{E} \times \mathbf{B}$ flow shear can more effectively suppress ITGs at higher isotope mass, at constant $\gamma_{\mathbf{E}\times\mathbf{B}}$. The effect of collisions could also break the gyro-Bohm scaling as demonstrated by non-linear gyrokinetic simulations for JET-ILW H-mode plasmas [129]. The fast ion pressure may also lead to turbulence suppression. Different heating power settings and fast ion slowing down times in plasmas with different main ion species can break the gyro-Bohm scaling through fast ion stabilisation [126, 130]. Although, this is not an intrinsic isotope dependence of the transport, but is due to differences in the heating schemes in different species.

3.2 Isotope dependence of the H-mode pedestal

Changing edge conditions with isotope mass could also break the gyro-Bohm scaling of the global confinement. Transport simulations on JET H, D and T plasmas with a model that has pure gyro-Bohm scaling for the local transport, indicate that the increase in the edge temperatures with isotope mass could lead to a favourable isotope scaling of the global confinement [116].

Previous studies investigating the isotope dependence of the pedestal include reports from JT-60U, JET and ASDEX-Upgrade. A series of H, D, T and DT ELMy H-modes were executed in JET with the Carbon wall (JET-C), which showed a weak isotope dependence of the thermal energy confinement time [131, 132]. The strong positive isotope dependence of the pedestal stored energy was compensated with a weak negative isotope dependence of the core plasma, which indicates that the effect of the pedestal in understanding the isotope dependence on confinement is essential.

Isotope experiments on JT-60U found a positive isotope dependence of the thermal energy confinement time [83, 105, 106], but analysis of the core transport suggests that this effect arises from the core and the pedestal structure has no direct dependence on the isotope mass [106]. The improved confinement is attributed to higher inverse normalised temperature gradient length ($R/L_T = R\nabla T/T$) in the core in D compared to H and/or higher fast-ion pressure in D than in H. Figure 3.1a shows the ion heat transport coefficient (χ_i) as a function of R/L_{T_i} (or $\nabla T_i/T_i$) in the core (at $r/a = 0.6$) for a series of H and D ELMy H-modes in JT-60U. The horizontal grey line denotes plasmas with similar input power, showing that the temperature gradient length is higher in D than in H at given input power, indicating a reduction in heat transport with increasing isotope mass. Although the pedestal pressure increased with increasing isotope mass at given input power, it is a result of the reduced transport in D leading to higher total poloidal β (β_p^{TOT}), which has a stabilising effect on the pedestal [133–135]. The increase in the slowing down time of the fast ions for D compared to H could also contribute to the higher β_p^{TOT} in D.

Recent experiments on ASDEX-Upgrade attempted to obtain similar pedestal pressures in H and D at similar input power and fuelling gas rates by varying the plasma triangularity (δ) at the edge [136, 137]. The pedestal stability is expected to improve with increasing triangularity [36, 62], thus the degraded pedestal pressure in H can be compensated by higher δ. The analysis of the above plasmas indicated that the pedestal has a dominant role in the isotope dependence on global confinement, although differences

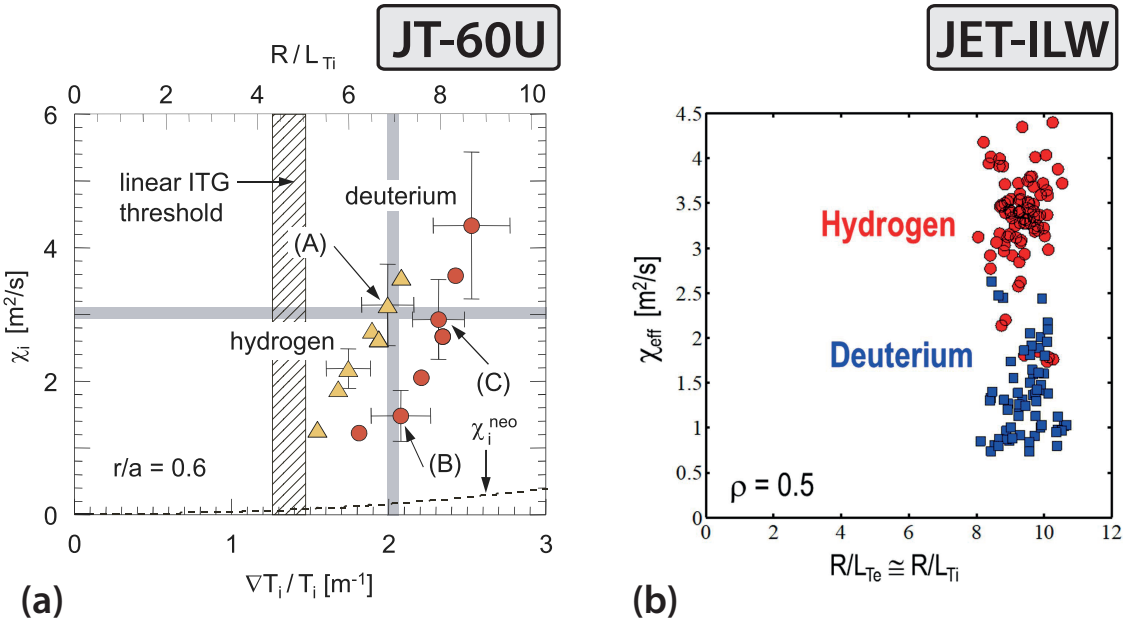

Figure 3.1: (a) The ion heat transport coefficient (χ_i) as a function of R/L_{T_i} (or $\nabla T_i/T_i$) in the core (at $r/a = 0.6$) for a series of H and D ELMy H-modes in JT-60U. Figure is adapted from [106]. (b) Effective heat diffusivity (electron+ion) as a function of $R/L_{T_e} \cong R/L_{T_i}$ in the core (at $\rho_{\mathrm{TOR}} = 0.5$) for JET-ILW type I ELMy H and D H-modes. Figure is adapted from [104].

in core confinement between H and D were also observed at high input power most likely due to higher fast ion pressure in D compared to H.

Type I ELMy H-mode plasmas in JET with the ITER-like Wall (JET-ILW) showed a positive scaling of $\tau_{\mathrm{E,th}}$ with the isotope mass: $\tau_{\mathrm{E,th}} \propto A^{0.4}$ [104, 138]. At the same input power and fuelling gas rate, the pedestal pressure is typically reduced in H compared to D, primarily due to lower pedestal density in H. In contrast to the above mentioned JT-60U experiments, in JET-ILW the gradient length (R/L_T) of core temperature profiles was nearly identical in H and D, despite large variations in the heat flux as shown in figure 3.1b [104, 138]. This suggests that the isotope effect may originate in the pedestal [104]. In JET-ILW, at similar pedestal pressure in H and D, the pedestal density and temperatures are not matched, but lower density in H compared to D is compensated with higher temperature. This is in contrast to JT-60U experiments, where density and temperature profiles were matched in H and D when the stored energy was matched by raising the H-NBI heating [83, 105, 106] and points to a difference in particle confinement in the two tokamaks [104].

Chapter 4

Role of the edge current in H-mode pedestal stability

As discussed in chapter 2, the ELM trigger is associated with the increase of the edge pressure gradient and/or the edge current density, which can drive coupled P-B modes unstable. It has been observed in JET-ILW type I ELMy H-modes that the pedestal stability is consistent with the P-B model in discharges with low D_2 gas fuelling rates, while, at higher gas rates and medium to high β, pre-ELM pedestals are found to be stable to P-B modes, although type I ELMs occur experimentally [53]. Furthermore, at high gas rates, the inter-ELM temperature pedestal growth is saturated half way through the ELM cycle leading to plasmas with reduced confinement [54].

Saturation of the pedestal temperature and its gradient prior to the ELM crash has also been observed on ASDEX-Upgrade [139, 140], DIII-D [141] and on C-mod [142], although the dependence of the saturation on the fuelling gas rate is not discussed in these studies. These reports have also found that the recovery time of the density pedestal is generally shorter than that of the temperature pedestal. Furthermore, the saturation of the pedestal temperature gradient is correlated with the onset of quasi-coherent fluctuations, implying that these fluctuations may play a role in regulating the edge transport. Possible explanations for the delay of the ELM crash when the pedestal evolution is saturated are also considered. The report on DIII-D pedestals [141] argues that quasi-coherent fluctuations limit and saturate the pedestal gradient, but allow the width and height to possibly further increase. However, experimental data where both the density and temperature heights and gradients are saturated is also presented, leaving the question of the ELM crash delay open. A recent study on ASDEX-Upgrade pedestals shows that the total stored energy increases while the pedestal parameters are saturated,

possibly causing stabilisation of P-B modes and delaying the ELM crash [140]. A time lag in the build-up of the total edge current with respect to the pressure gradient due to current diffusion could also be responsible for the delay of the ELM crash. This possibility has been investigated on ASDEX-Upgrade [139, 143], showing that the current diffusion only plays a minor role in the edge of ASDEX-Upgrade H-mode plasmas.

In order to try and understand the origin of the inconsistency between the pedestals stable to P-B modes and the experimentally observed type I ELMs on JET-ILW, in this chapter the time evolution of the edge current during the ELM cycle is analysed, investigating both the edge bootstrap current density profile (j_{BS}) and the Ohmic component (j_{OH}). A similar approach is taken as in [139, 143] for ASDEX-Upgrade, but this investigation accounts for pedestals at higher temperature, where potentially the effect of current diffusion is more dominant due to the higher plasma conductivity. The bootstrap current is calculated with the local neoclassical code NEO [144, 145], and the Ohmic contribution to the total current is accounted for, by solving the current diffusion equation in the plasma. For this analysis the JETTO [146] transport code has been utilised to consider a realistic geometry.

In the present chapter, first the diagnostic and analysis methods used to investigate the pedestal structure are introduced. These measurements and techniques are used throughout this thesis. In section 4.2 the calculation of the edge bootstrap current in JET-ILW H-modes is discussed. The inter-ELM evolution of the edge bootstrap current is studied in section 4.3. Section 4.4 analyses the effect of current diffusion on the evolution of the edge current inter-ELM for a range of JET-ILW pedestal collisionalities.

4.1 Diagnostics and analysis methods

The measurement of the edge current density is very challenging, and to date there is no available diagnostic for this purpose on JET. However, many other plasma parameters can be measured, which then can be used to evaluate the bootstrap current using models. These measurements and other techniques, which are utilised throughout this thesis to examine the pedestal structure are introduced here. The main quantities investigated in this work are the electron density, electron and ion temperatures and the divertor target conditions.

Thomson scattering

The main workhorse for kinetic profile measurements on JET is the high resolution Thomson scattering (HRTS) [147]. The Thomson scattering diagnostic (TS) is able to measure the electron density and temperature in the plasma. A high energy laser pulse is injected into the plasma and the light scattered by free electrons is collected. The electron density can be calculated from the total intensity of the scattered light, while the Doppler broadening of the scattering spectrum carries information on the electron temperature [8]. One very important feature of TS is the intrinsic alignment of the electron temperature and density profiles as it is measured in the same scattering volume. The TS system on JET measures profiles in 63 points along the outer radius of the plasma as shown in figure 4.1 with a 8 mm spatial resolution. The pulse duration of the laser is 20 ns with a 20 Hz repetition rate. The low repetition rate limits the information collected from the ELM cycle, thus the ELM-synchronisation technique is used to improve signal statistics, as discussed in the next subsection.

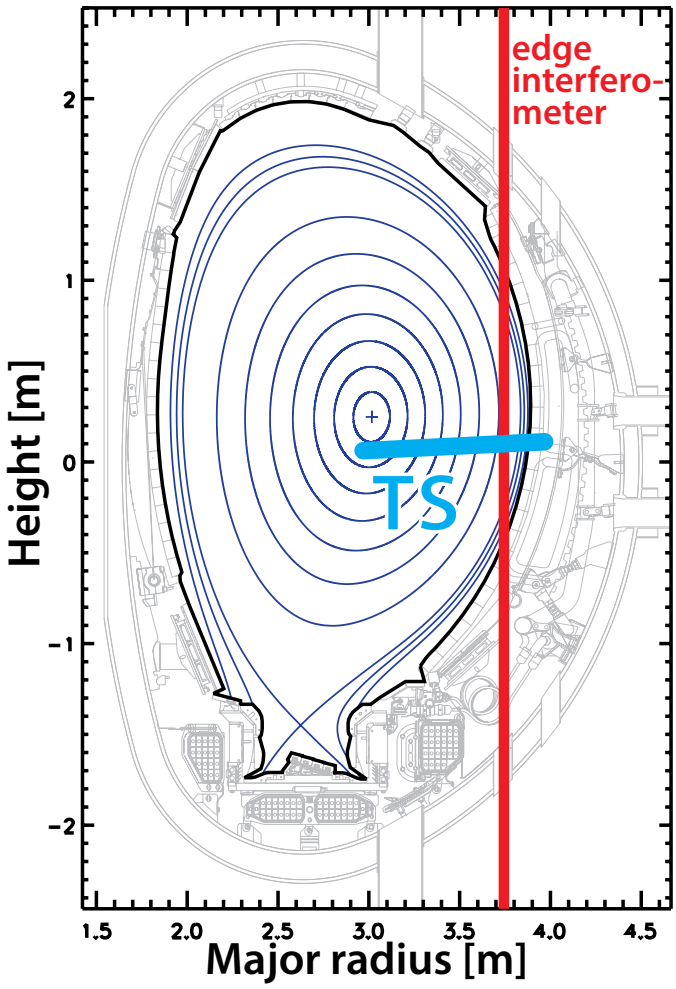

Figure 4.1: The geometry of the TS and edge interferometry is shown in a poloidal cross-section of JET.

The steep gradient region is of particular importance for understanding the pedestal behaviour. However, in this region the gradient length of the kinetic profiles is comparable to the scattering length of a given TS channel. This leads to higher weighting of the temperature in the high density region within the scattering length. Thus, the instrument function of the diagnostic system has to be taken into account. In the fitting code being used here, a density weighted deconvolution method [148] is implemented, which uses the instrument function and the separately recovered density profile for the deconvolution of the temperature profile. The instrument function applied is described in detail in [149].

ELM synchronisation of kinetic profiles

As the typical ELM frequency on JET is of the order of 10-100 Hz, the time resolution (20 Hz) of the TS diagnostic is too low to be able to describe the inter-ELM evolution before an individual ELM. In order to maximise the number of profiles characterising a given phase of the evolution, the so-called ELM synchronisation technique is used. For this purpose, the TS profiles are collected from a steady time window of the discharge, assuming that each individual inter-ELM evolution is similar. The ELM cycle is divided into intervals with a given percentage, as shown in figure 4.2 with 20 % bins. The ELM marker in figure 4.2 is the outer divertor photon flux of the 527 nm Beryllium line which is a good indicator for the ELMs. 100 % corresponds to the ELM crash and 0 % corresponds to the ELM crash of the preceding ELM cycle. In this case, the 0-20 % interval is excluded from the analysis as the profiles in this interval are dominated by the ELM crash. Composite profiles are taken from each 20 % bin and a modified tanh function [148] is fitted to the profiles. To account for the variation of the plasma position during the discharge, the radial position of each profile is aligned relative to the separatrix position provided by the EFIT [150, 151] equilibrium reconstruction. The systematic error introduced due to the variation of the radial shift when overlaying the TS profiles is negligible compared to the stochastic errors [152]. The ELM synchronisation technique assumes that the ELM cycles during the steady phase of a discharge are nearly identical. However, several studies have reported differences in the ELM period and/or ELM energy losses between ELMs even in steady plasmas as for example shown in [153–156]. These differences certainly introduce systematic errors in the ELM synchronisation analysis, nevertheless, the composite profile represents the average behaviour of the ELM cycles in a given discharge. The mtanh fit gives the height, width, position and slope of the profiles. Furthermore, the profiles can be used as input for further analysis as shown in the next section in case of bootstrap profiles calculation. The pedestal fitting method

outlined above is implemented in the HRTSfit pedestal fitting tool, which code has been used for the work presented in this thesis.

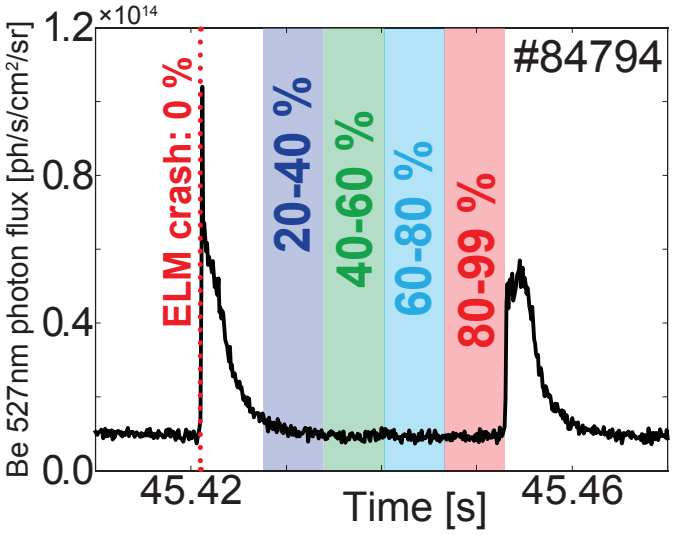

Figure 4.2: ELM cycle is normalised to a relative time scale (from 0 % to 100 %) and divided into 20 % long intervals.

Interferometry

Plasma interferometry is a routinely applied technique to measure the line integrated plasma density [157]. The refractive index in the plasma is a function of the plasma density. Thus, a probing wave directed through the plasma suffers a phase shift in comparison to a reference wave propagating in vacuum. The phase shift is proportional to the line-integrated plasma density:

$$\Delta\phi = -\frac{\omega}{2cn_c}\int n_e \mathrm{d}l \ , \tag{4.1}$$

where ω is the frequency of the probing light, n_c is the critical density and c is the speed of light. JET is equipped with a far infrared interferometer measuring the plasma density with a submillisecond time resolution using 4 vertical and 4 lateral channels [158, 159]. In the present thesis, the edge interferometer channel will be used, which is shown by the solid red line in figure 4.1.

Electron cyclotron emission

The electron cyclotron emission (ECE) diagnostic provides local electron temperature measurements in the plasma [157]. Electrons in the plasma emit microwave radiation at the gyrofrequency: $f = eB/2\pi m_e$ with m_e the electron mass. In an optically thick

plasma (which is typically the case in the core of a tokamak) the radiated intensity can be assumed as black body radiation and the electron temperature can be evaluated. As the magnetic field in a tokamak scales as $1/R$, the gyrofrequency of electrons is a function of the radial position, thus a radial localisation of the T_e measurement is possible. On JET, the ECE diagnostic has 96 channels and measures the electron temperature profile with a millisecond time resolution [160]. In this thesis, ECE is not used for profile measurement, because in the investigated plasmas the pedestal is optically thin. However, ECE channels measuring just radially inward the pedestal are utilised to follow the fast time evolution of the ELM crash.

Charge exchange recombination spectroscopy

Charge exchange recombination spectroscopy (CXRS) is used to measure the ion temperature and the plasma rotation velocity. CXRS is usually applied on the NBI heating beam. Due to the presence of the neutrals, charge exchange recombination reactions take place along the beam lines. Charge is transferred from the neutral beam to the main ions and plasma impurities. The recombined ion is born in an excited state leading to photon emission at characteristic wavelengths. The ion temperature and plasma rotation are measured from the Doppler broadening and the shift of the spectral lines using dedicated spectrometers

JET has separate observation systems for the edge [161, 162] and core [163, 164] profiles. The core CXRS diagnostic has recently been upgraded enabling simultaneous measurement of main ion and impurity charge exchange [164]. The impurity charge exchange measurements in JET-ILW is typically carried out using diagnostic Ne puffs. The maximum time resolution of the diagnostic is 10 ms and the spatial resolution is ≈ 5 cm.

Langmuir probes

Langmuir probes are small electrodes inserted into the plasma to determine the electron density, temperature and ion saturation current [157]. This is an invasive technique as the probe is in direct contact with the plasma. Thus, in tokamaks, Langmuir probes are only used at the plasma edge. Langmuir probes are typically installed on the limiters and divertor targets. The probes are externally biased with respect to the plasma. Information on n_e and T_e can be gained by sweeping the bias on the probe and registering the current-voltage characteristics. Figure 4.3 shows the position of the Langmuir probes in

the JET-ILW divertor. These probes were used to support the results of edge transport simulations in section 6.3

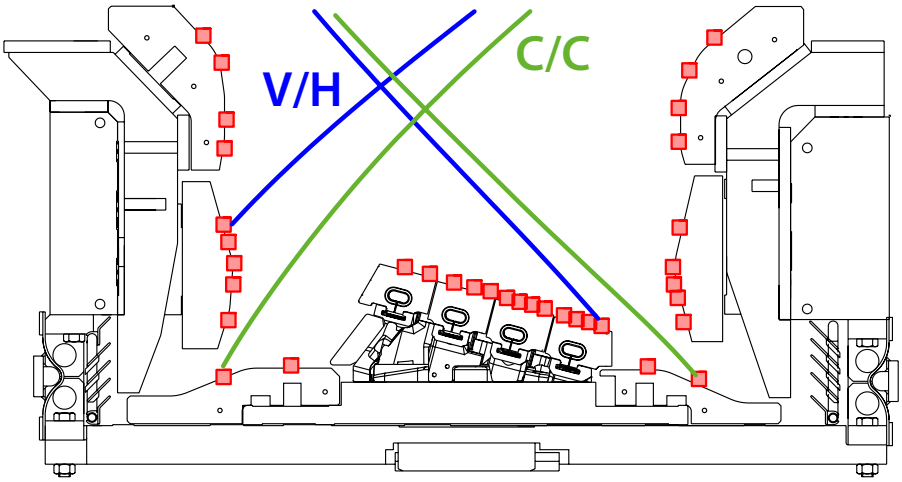

Figure 4.3: Position of the Langmuir probes (in red) in the JET divertor. The magnetic configuration and the position of the strike points for two frequently used divertor configuration are also shown. The so-called "Corner" or C/C divertor configuration, where both divertor strike points are close to the pumping duct is shown in green. The so-called V/H configuration, where the inner strike point is on the vertical target and outer strike point is on the horizontal target is shown in blue.

Infrared thermography

Heat deposition onto the divertor target can be estimated by infrared (IR) thermography. The photon flux emitted from a radiating body at a given wavelength depends on its surface temperature. With a carefully chosen wavelength and known emissivity, the surface temperature can be evaluated using IR thermography. The heat flux deposition can be reconstructed from the time evolution of the surface temperature by solving the heat diffusion equation in the divertor target. On JET, several cameras are installed to view most of the divertor target area [165]. The systems provide reconstruction of the heat deposition profiles with time resolution in the submillisecond range, which are utilised in section 6.3 to constrain edge transport simulations.

4.2 Edge bootstrap current density profile

In the steep pressure gradient region at the edge of H-mode plasmas, the current density is usually dominated by the bootstrap current. In the present section only the bootstrap current is considered and the effect of the Ohmic current on the inter-ELM evolution of the total edge current is discussed in section 4.4.

Trapped particles that are scattered into passing orbits before completing their banana orbits do not contribute to the bootstrap current. As the bootstrap current is associated with the existence of trapped particles, it strongly depends on the collisionality. Collisionality (ν) is the ratio of the particle collision frequency and the banana bounce frequency. The electron collisionality is calculated in this thesis as defined by eq. (18b) in [166]:

$$\nu_e^* = 6.921 \times 10^{-18} \frac{qRn_e Z_{\text{eff}} \ln \Lambda_e}{T_e^2 \epsilon^{3/2}} \ , \tag{4.2}$$

where Z_{eff} is the effective ion charge, $\ln \Lambda_e = 31.3 - \ln(\sqrt{n_e}/T_e)$ is the Coulomb logarithm and $\epsilon = a/R$ the inverse aspect ratio.

The bootstrap current can either be evaluated using first principle neo-classical transport solvers or several formulas exist, which express the bootstrap current as a function of geometric parameters of the magnetic equilibrium and the gradients of the kinetic profiles. One widely used formula is the Sauter-formula [166, 167], which is an analytical fit to the results of the CQLP neoclassical transport solver for various plasma conditions using an approximate linearised collision operator. It expresses the bootstrap current as a function of density and temperature gradients:

$$\begin{aligned} j_{\text{BS}}^{\text{Sauter}} = \ & \frac{I(\Psi)p(\Psi)}{B_{\text{ax}}} \Bigg[\underbrace{\mathcal{L}_{31}}_{\text{coeff. of } \nabla n_e} \frac{\partial \ln n_e}{\partial \Psi} + \underbrace{R_{pe}(\mathcal{L}_{31} + \mathcal{L}_{32})}_{\text{coeff. of } \nabla T_e} \frac{\partial \ln T_e}{\partial \Psi} + \\ & + \underbrace{(1 - R_{pe})(1 + \frac{\mathcal{L}_{34}}{\mathcal{L}_{31}}\alpha)\mathcal{L}_{31}}_{\text{coeff. of } \nabla T_i} \frac{\partial \ln T_i}{\partial \Psi} \Bigg] \ , \end{aligned} \tag{4.3}$$

where $I(\Psi) = RB_t$, $R_{pe} = p_e/p$ and α, $\mathcal{L}_{31}$, $\mathcal{L}_{32}$, $\mathcal{L}_{34}$ are coefficients, which can be analytically computed from equations (13) through (18) in [166]. Due to the approximate electron-ion collision operator used in the simulation and also due to the simplified fitting formula used at high collision frequency, the Sauter-formula is less accurate at higher electron collisionality [168].

In this chapter the bootstrap current density is computed from first principles with the local neoclassical transport code NEO [144, 145], which solves the drift-kinetic equation with the full linearised Fokker-Planck collision operator including all inter-species collisions. This approach provides a more accurate estimation of the bootstrap current than the Sauter-formula, especially at high collisionality, where the Sauter-formula has been shown to overestimate the bootstrap current by up to 100 % compared to NEO for JET-ILW pedestals [53]. The parallel bootstrap current density (j_{BS}) and the parallel component of the total current density (j_{tot}) profiles in this chapter are expressed in the

form of a flux surface average:

$$j_{\mathrm{BS}} = \frac{\langle \boldsymbol{j}_{\mathrm{BS}} \cdot \boldsymbol{B} \rangle}{B_{\mathrm{ax}}} \, , j_{\mathrm{tot}} = \frac{\langle \boldsymbol{j}_{\mathrm{tot}} \cdot \boldsymbol{B} \rangle}{B_{\mathrm{ax}}} \, , \tag{4.4}$$

where $\boldsymbol{B}$ is the magnetic field and B_{ax} is the magnetic field on axis.

The inputs for NEO are the plasma equilibrium reconstructed with EFIT, the electron (T_e) and ion (T_i) temperatures and the electron (n_e) and ion density (n_i) profiles. The kinetic profiles are obtained by fitting the electron kinetic profiles from the TS measurements, assuming equal electron and ion temperatures (consistent with charge exchange measurements at the pedestal top), constant line averaged Z_{eff} measured by visible Bremsstrahlung and Be as the intrinsic impurity.

In order to track the time dependent evolution of j_{BS} during the JET-ILW type I ELM cycle, it is divided into 20 % long intervals and the kinetic profiles are ELM-synchronised. The 0-20 % interval is excluded from the analysis as the profiles in this interval are often dominated by the particular dynamics of each ELM crash. Composite profiles are taken from each 20 % bin of a steady phase of the discharge ($> 10 \times \tau_{\mathrm{E,th}}$) and an mtanh function is fitted to both the electron temperature and density profiles.

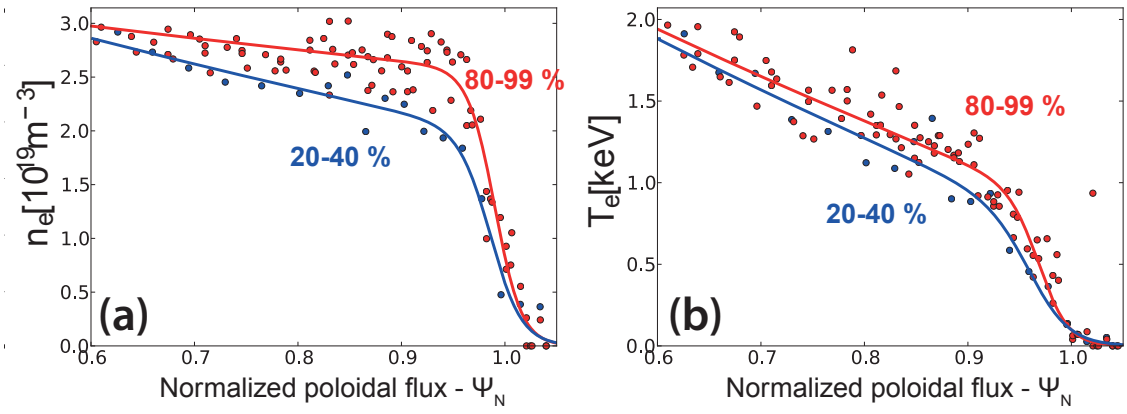

Figure 4.4: The n_e and T_e experimental data for the 20-40 % and 80-99 % intervals in #84794.

Examples of fitted n_e and T_e profiles derived from composite TS measurements are shown in figure 4.5a and 4.5b, respectively, for JET-ILW discharge #84794 (1.4 MA/1.7 T, input power $P_{\mathrm{IN}} \simeq 16$ MW, average triangularity $\delta = 0.27$, injected gas rate $\Gamma_D = 2.8 \cdot 10^{21}$ e/s) for the four inter-ELM intervals from 20-40 % to 80-99 %. The n_e and T_e experimental data for the 20-40 % and 80-99 % intervals in figure 4.4a and b show that the observed difference in the fitted profiles is beyond any experimental uncertainty, as seen in the scatter in the data points. Figure 4.5c shows the inter-ELM evolution of the edge electron pressure gradient. In this discharge the peak pressure gradient continuously

increases during the inter-ELM cycle as typically observed in H-modes with low gas injection rate. The inter-ELM evolution of the j_{BS} profile is shown in figure 4.5d, showing a similar time evolution to that of the pressure gradient, as expected.

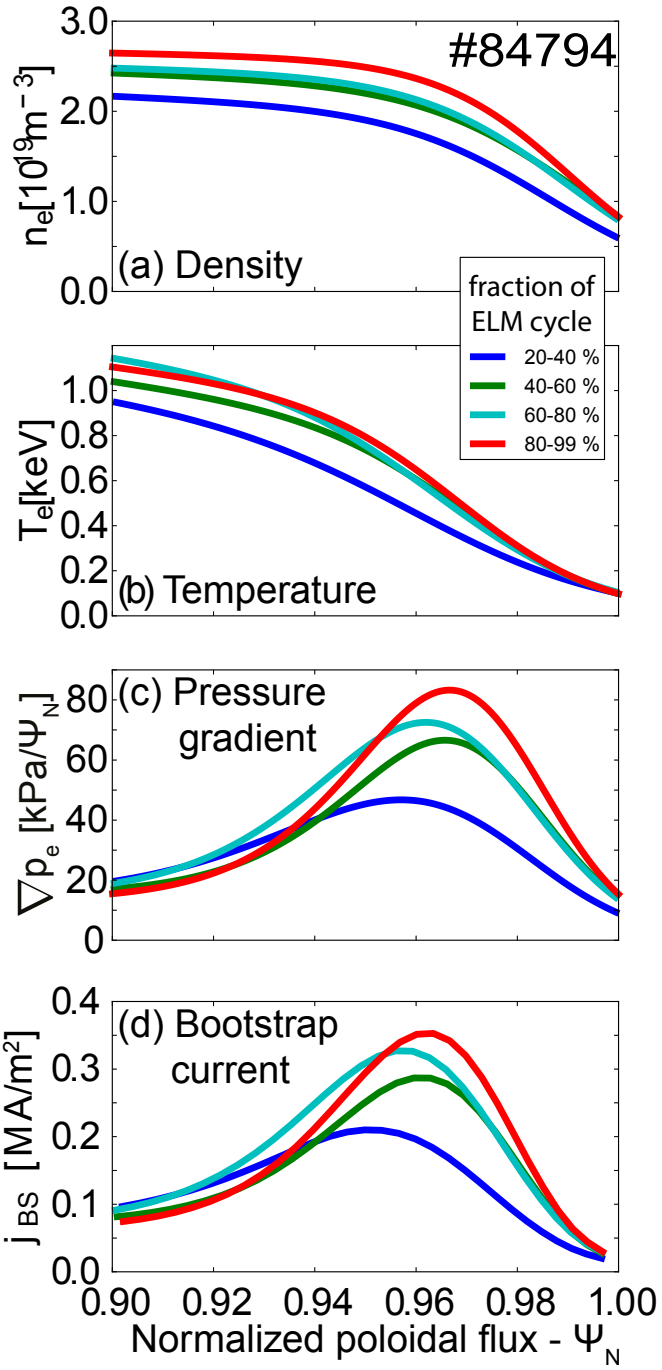

Figure 4.5: Time evolution of (a) the edge electron density (n_e); (b) the edge electron temperature (T_e); (c) the edge electron pressure gradient (∇p_e) and (d) the edge bootstrap current density (j_{BS}) profiles in the inter-ELM cycle of pulse #84794, evaluated for the four intervals: 20-40 %, 40-60 %, 60-80 %, 80-99 % of the total ELM cycle.

The sensitivity of the j_{BS} profiles to the uncertainties of the input parameters n_e, T_e and Z_{eff}, has been investigated. For this purpose, "modulated" n_e and T_e profiles were

constructed, whereby each fitted parameter of the mtanh function (width, height, position and slope) was substituted with a Gaussian random number. The mean and variance of the Gaussian random numbers are given by the mean and variance of the parameter estimates of the mtanh fit. For each case, the j_{BS} profile calculation with NEO is then repeated several times (~ 50) using as input the different "modulated" profiles. The line averaged Z_{eff} is varied within the experimental uncertainty of ± 10 %. The result of the sensitivity analysis is shown in figure 4.6, where all three parameters (n_e, T_e, Z_{eff}) are modulated within their uncertainties. The percentile of the resulting j_{BS} profiles gives the $1\sigma_{sd}$ and $2\sigma_{sd}$ error bars where σ_{sd} is the standard deviation. The error bars are visible in figure 4.6 in red and blue, respectively. Since all three parameters (n_e, T_e, Z_{eff}) were assumed to be independent in the uncertainty analysis, the resulting error bars are somewhat overestimating the error. Systematic errors were not taken into account in this analysis.

Tests where only one input parameter is "modulated" have shown that the uncertainty in the calculated j_{BS} is dominated by the uncertainty in the T_e profiles. This is due to the fitted TS T_e profiles having a larger uncertainty than the n_e profiles in the JET-ILW dataset analysed in this study. In the remainder of this chapter the $1\sigma_{sd}$ error bars are used as the uncertainty in the j_{BS} profile.

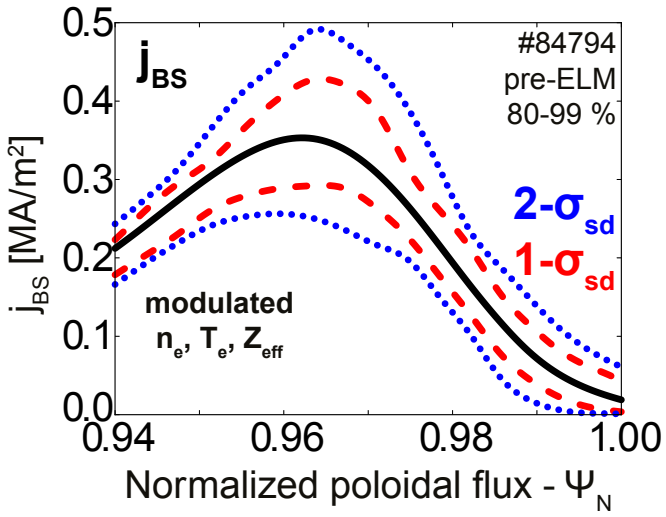

Figure 4.6: Edge j_{BS} profile for pulse #84794 in the last 20 % of the ELM cycle (black) and 1-σ_{sd} (red) and 2-σ_{sd} (blue) uncertainties, derived from the sensitivity analysis on the j_{BS} calculation to n_e, T_e and Z_{eff} uncertainties.

4.3 Inter-ELM evolution of the edge bootstrap current

In JET-ILW type I ELMy H-modes at low D_2 gas rates the edge pressure gradient continuously increases during the inter-ELM phase, until the ELM crash [54]. On the other hand, at high D_2 gas fuelling rates and at high β, the pressure edge gradient is typically saturated in the second half of the ELM cycle and the pre-ELM pedestals have been shown to be stable to P-B modes [53, 54]. In the latter cases, the global confinement (H_{98}) is lower than in pulses with low gas rates at the same input power, primarily due to lower temperature pedestals. In this section the inter-ELM evolution of the edge bootstrap current is investigated and compared to the time evolution of the density, temperature and pressure gradients in the ELM cycle.

The set of type I ELMy Deuterium H-mode discharges studied in [53, 54] are considered here. The plasmas were at 1.4 MA/1.7 T, low triangularity (δ), $P_{\rm sep} = 4 \rightarrow 14$ MW, gas rate: $\Gamma_{\rm D_2} = 2.8 \rightarrow 18 \cdot 10^{21}$ e/s, normalised β: $\beta_N = 1.2 \rightarrow 2.8$ and ELM frequency: $f_{\rm ELM} = 12 \rightarrow 120$ Hz. $P_{\rm sep}$ is the power across the separatrix: $P_{\rm sep} = P_{\rm loss} - P_{\rm rad,bulk} = P_{\rm abs} - {\rm d}W/{\rm d}t - P_{\rm rad,bulk}$, where $P_{\rm abs}$ is the total absorbed power given by the sum of the Ohmic power, the absorbed neutral beam power (accounting for shine through) and absorbed ion cyclotron heating power (where applicable). $P_{\rm rad,bulk}$ is the total radiated power inside the separatrix as estimated by a weighted sum of representative bolometer channels, $P_{\rm loss}$ is the loss power given by $P_{\rm loss} = P_{\rm abs} - {\rm d}W/{\rm d}t$ and ${\rm d}W/{\rm d}t$ is the rate of change of the total stored energy, which is negligible in the steady phases of the discharges.

In the experiment, at a given P_{sep}, the electron pressure at the pedestal top ($p_{e,PED}$ [Pa] $= 1.602 \times n_{e,PED}$ [10^{-19}m^{-3}] $\times T_{e,PED}$ [eV], where 1.602 originates from the elementary charge as T_e is measured in eV) is reduced with increasing gas rate mainly via a reduction in the pedestal temperature. The pedestal collisionality ($\nu_{e,PED}$) is mainly driven by the variation in the pedestal temperature in the power and gas scans [53] and varies between $\nu_{e,PED} = 0.3 \rightarrow 4.5$.

Figure 4.7 compares the inter-ELM evolution of $j_{\rm BS}$ at different gas rates: at low $P_{\rm sep} = 4$ MW (4.7a) and at high $P_{\rm sep} = 13$ MW (4.7b). j_{BS} is reduced at low power due to the lower T_e and thus higher $\nu*$ compared to the high $P_{\rm sep}$ case. At "low" gas injection (where the pre-ELM stability is consistent with the P-B model [53]), the peak j_{BS} continuously increases during the ELM cycle. This change in peak j_{BS} is beyond the uncertainties indicated with the 1σ error bars. Conversely, at "medium" and "high" gas rates the evolution of peak j_{BS} is roughly constant throughout the second half of the

ELM cycle within the 1σ error bars. This saturation of peak j_{BS} during the ELM cycle at high gas rate is observed both at low and high input power.

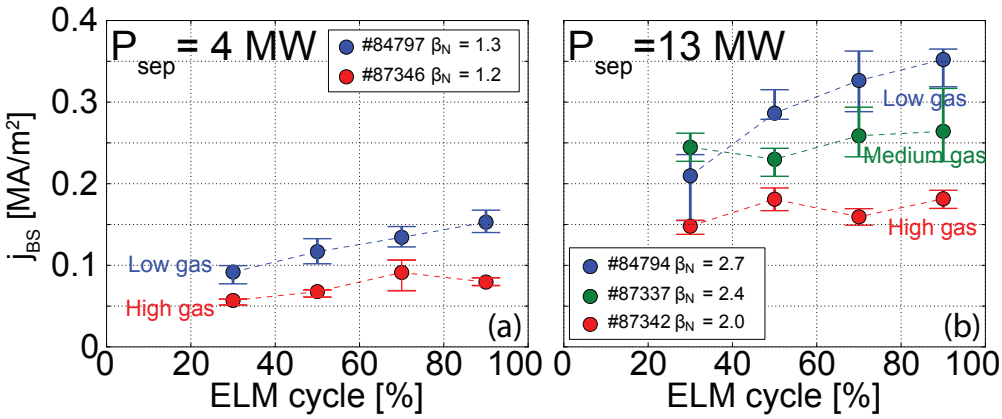

Figure 4.7: Evolution of peak j_{BS} during the ELM cycle in type I ELMy H-modes at low ($2.8 \cdot 10^{21}$ e/s), medium ($8.4 \cdot 10^{21}$ e/s) and high ($18 \cdot 10^{21}$ e/s) gas rates at constant P_{sep}: (a) lowest power and (b) highest power of the power and gas scans dataset.

It is interesting to compare the inter-ELM j_{BS} evolution to that of the separate drives of ∇p_e, namely the temperature and density gradients, as shown in figure 4.8, where all values are normalised to the pre-ELM phase value. Figure 4.8 shows the evolution of the peak of the edge j_{BS} profile and the peak of the gradients, thus the radial location the data corresponds to is changing in time. For all shots of the dataset, it has been observed that peak j_{BS}, peak ∇p_e and peak ∇T_e always exhibit the same time evolution, regardless of the ∇n_e inter-ELM evolution. Figure 4.8a shows the case of pulse #84794 where the pedestal ν^* is lowest in the scan: peak ∇n_e, peak ∇T_e and peak ∇p_e all increase during the ELM cycle. In figure 4.8b a higher ν^* case (#87342) is shown, where the evolution of peak ∇p_e is saturated and closely follows the evolution of peak ∇T_e, but the evolution peak ∇n_e is different, with ∇n_e first increasing and then decreasing. This latter behaviour is typical of the whole dataset, suggesting that the evolution of peak ∇p_e is driven by the time evolution of peak ∇T_e.

The dominant effect of the temperature gradient on j_{BS} can be understood by separately evaluating the ∇n_e and ∇T_e terms of $\nabla p_e \sim n_e \nabla T_e + T_e \nabla n_e$. In JET-ILW pedestals, the maximum ∇T_e is typically located radially inwards of the maximum ∇n_e [169–171], as can be seen e.g. in figure 4.5 for pulse #84794. This relative radial shift between T_e and n_e gradients leads to a smaller contribution of the $T_e \nabla n_e$ term to ∇p_e, as the temperature is low where the density gradient peaks, explaining why the pressure gradient is dominated by the $n_e \nabla T_e$ term. The ratio of $n_e \nabla T_e / T_e \nabla n_e$ is ~ 4 in the dataset at the maximum ∇p_e.

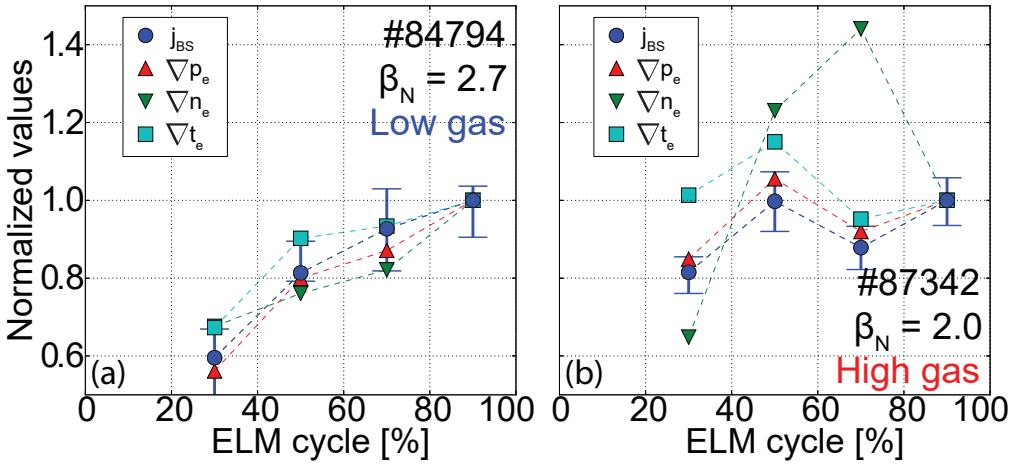

Figure 4.8: Inter-ELM evolution of peak j_{BS} and peak of p_e, n_e, T_e gradients at low and high gas rates at $P_{\text{sep}} = 13$ MW. All values are normalised to the pre-ELM phase. The error bars are shown only for peak j_{BS} to avoid overcrowding of the plot, but all data points have error bars of magnitude similar to those shown.

For the study of the separate contributions from ∇n_e, ∇T_e and ∇T_i to the bootstrap current, Sauter's analytical formula is used as it expresses the bootstrap current as a function of density and temperature gradients as shown in eq. (4.3). The NEO code solves the drift-kinetic equation and its output is the particle distribution function, thus it is not straightforward to extract information on the separate drives of the density and temperature gradients. The coefficient of ∇n_e is larger than the coefficient of ∇T_e and ∇T_i in the range of pedestal collisionalities considered in this chapter. Despite the higher coefficient for ∇n_e, the bootstrap current is dominated by the ∇T_e term of Sauter's formula. The ratio of n_e, T_e and T_i drives is approximately 1:3:1 in the dataset at the maximum ∇p_e. This result also implies that (in case of local calculation of the bootstrap current) the error introduced by the $T_e = T_i \Rightarrow \nabla T_e = \nabla T_i$ approximation is not significant as the contribution from ∇T_i to the bootstrap current is small.

4.4 Effect of Ohmic current diffusion on the total edge current

JET-ILW pre-ELM pedestals at high gas rates and medium to high β ($\beta_N \approx 2-3$) are stable to P-B modes, indicating that additional physics may be required to explain the ELM trigger [53]. Furthermore, in high β, high gas rate discharges both the pressure gradient [53, 54] and the peak bootstrap current (see section 4.3) reach their steepest gradient well before the ELM crash. Therefore, a possible explanation for the "delay" in the ELM crash could be a time delay in the build up of the total edge current inter-

ELM due to current diffusion with respect to the inter-ELM recovery of density and temperature gradients (which drive the bootstrap current recovery).

The bootstrap current profiles presented in section 4.3 are calculated from the measured kinetic profiles assuming steady-state conditions. As a result, the time evolution of j_{BS} follows that of the pressure gradient. The effect of inter-ELM current diffusion can be assessed by taking into account the contribution of the Ohmic current. In [139] and [143], a simple model for current diffusion is used, which helps to understand the dynamics of the edge current in the inter-ELM period. The model includes Ohm's law:

$$j_{\mathrm{tot}} = \sigma E + j_{\mathrm{BS}} \ , \tag{4.5}$$

where E is the electric field and σ the plasma conductivity. In general, the second term in eq. (4.5) includes any non-inductively driven current. Here, only the bootstrap current is considered. Substituting Faraday's law into eq. (4.5) gives a current diffusion equation:

$$\frac{\partial E}{\partial t} = \frac{1}{\sigma}\left(\frac{\nabla^2 E}{\mu_0} - E\frac{\partial \sigma}{\partial t} - \frac{\partial j_{\mathrm{BS}}}{\partial t}\right) \ , \tag{4.6}$$

where μ_0 is the vacuum permeability and $\partial/\partial t$ is the time derivative. Eq. (4.6) shows that an increase in bootstrap current ($\partial j_{\mathrm{BS}}/\partial t$) reduces the electric field in the pedestal build-up phase, such that the electric field opposes the build-up of the total current. Any change in the electric field relaxes in a diffusive process ($\nabla^2 E/\mu_0/\sigma$) on the resistive timescale, which is proportional to the plasma conductivity.

The JETTO [146] code was used to solve the current diffusion equation in realistic geometry. JETTO is a plasma transport code calculating the evolution of plasma parameters in an axisymmetric MHD equilibrium. The simulations were run within the JINTRAC framework [172], which is a set of linked codes for the integrated simulation of all phases of a tokamak scenario. Here only the JETTO part of the framework was used. The energy and particle transport were not simulated in the JETTO runs: the simulations were run in predictive mode for the current, and in interpretative mode for density and temperature. Since NEO is not implemented in JETTO for the calculation of the bootstrap current, the NCLASS code [173] was used for this purpose. NCLASS is a neoclassical code based on the fluid moment approach with a simplified collision operator, in contrast to NEO that solves the drift kinetic equation with the full linearised Fokker-Planck collision operator. The difference between NEO and NCLASS calculated bootstrap currents is less than 10 % in the investigated cases.

The input kinetic profiles for the JETTO runs are the same as those used for the NEO calculations (see section 4.2). However, in order to enable JETTO to simulate the inter-ELM evolution of the total current, the inter-ELM profiles have to be interpolated on a finer time grid. In particular, the collapse of the profiles during the ELM crash have to be included. Due to the relatively slow time resolution of the TS diagnostic (20 Hz), the short time scale of the ELM crash ($\leq$ ms) cannot be resolved. Thus, the temperature and density profile evolution during the ELM-crash is modelled by a simple, linear interpolation in time between the pre-ELM and the post-ELM profiles. In order to obtain a more realistic picture of the sudden change of the pedestal profiles at the ELM crash, the timescale of the crash is estimated from the interferometry and electron cyclotron emission (ECE) measurements, both equipped with higher time resolution than TS (<1 ms for ECE and 1.5 ms for interferometry). An ECE channel located close to the pedestal top and an interferometry line-of-sight through the plasma edge are chosen. The duration of the ELM crash is evaluated by taking the time difference between the maximum and minimum of these signals in the vicinity of the ELM crash. ECE and interferometry are only used for this purpose, while the shape of the density and temperature profiles rely solely on the TS measurements.

The effect of any long time-scale evolution in the plasma is eliminated by running the JETTO simulations with steady (pre-ELM) profiles for 5 seconds. Following this period, 10 consecutive ELM cycles are simulated. This approach ensures that the simulation reaches a dynamic equilibrium in which the ELM cycles become identical. Figure 4.9 illustrates the evolution of the electron pressure close to the pedestal top in the JETTO simulations. In what follows, the results shown belong to the evolution of the last ELM cycle of the sequence.

The fixed boundary equilibrium code ESCO [146] is used to calculate the equilibrium by taking into account the steep pressure gradient at the plasma edge. The plasma boundary is taken from EFIT. ESCO is run only at the very beginning of the simulation to provide the grid on which the current diffusion equation is solved. In the later stage of the simulation, the equilibrium is not self-consistently recalculated, only the current density and q profiles are evolved according to the redistribution of the current.

The boundary condition at the separatrix is a key element in the simulation. However, it is challenging to determine the boundary condition experimentally on the time scale of the ELM cycle, as the magnetic measurements are affected by slow data acquisition and the screening of the vacuum vessel and other conducting structures. In order to examine

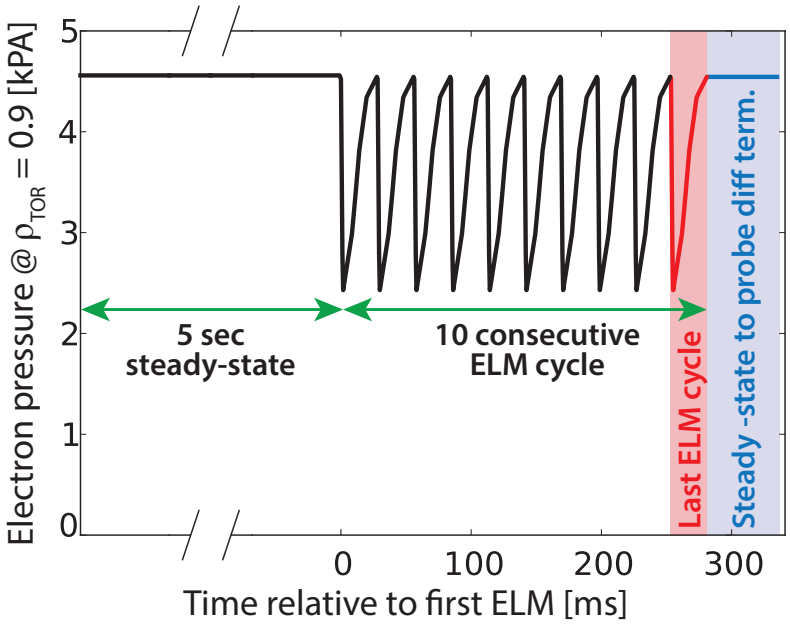

Figure 4.9: Evolution of the electron pressure close to the pedestal top ($\rho_{\mathrm{TOR}} = 0.9$, with ρ_{TOR} the normalised toroidal flux) in the JETTO simulations. After 5 seconds of simulation time with steady kinetic profiles, 10 consecutive ELM cycles are simulated. In what follows, the results shown belong to the evolution of the last ELM cycle of the sequence, indicated with the red shaded area. Some simulations were continued with fixed pre-ELM profiles to test the diffusion term in eq. (4.6). This is indicated with the blue shaded area.

the effect of the choice of boundary condition on the edge current density evolution, two options are tested here:

1. the total plasma current is held constant,

2. the loop voltage is held constant.

It is expected that current diffusion could have a significant effect on the total current build-up if the resistive timescale is comparable to the inter-ELM period. Thus, in section 4.4.1 two extreme cases of JET-ILW type I ELMy pedestals at low I_p (1.4 MA) are investigated in detail: in the first case (pulse #84794), the pedestal collisionality is $\nu^*_{\mathrm{e,PED}} \simeq 0.3$, the ELM frequency is $f_{\mathrm{ELM}} \simeq 35$ Hz and the pedestal temperature is $T_{\mathrm{e,PED}} \simeq 0.9$ keV, thus the conductivity is high and the resistive timescale is longer; the second case is a higher collisionality ($\nu^*_{\mathrm{e,PED}} \simeq 0.9$) pulse (#87342) with the highest power in the high gas rate scan, with a colder pedestal, $T_{\mathrm{e,PED}} \simeq 0.6$ keV, but much higher ELM frequency, $f_{\mathrm{ELM}} \simeq 120$ Hz, thus the ELM period may be short enough to be comparable to the resistive timescale. A connection to high I_p JET-ILW type I ELMy H-modes is achieved by analysing a pedestal obtained at $I_p = 3.0$ MA. This is presented in section 4.4.2, together with sensitivity calculations on the ELM duration and magnitude. Section 4.4.3 discusses the impact of current diffusion on pedestal stability analyses.

4.4.1 Comparison of pedestals at different fuelling gas rates

First, the simulation results of the highest pedestal temperature discharge (#84794, high power, low gas rate) are presented. In figure 4.10 the inter-ELM evolution of the edge total and bootstrap current profiles are shown, comparing the impact of the two different boundary conditions on the current evolution. Figure 4.10a shows the result of the simulation where the total current is held constant at the experimental value: $I_\mathrm{p} = 1.4$ MA. Figure 4.10b shows the result of the JETTO run with a fixed loop voltage at the separatrix. $U_\mathrm{loop} = 0.11$ V is chosen, so that the total plasma current on average is close to 1.4 MA. As a consequence of the flattened kinetic profiles during the ELM crash, the bootstrap current profile (dashed lines in figure 4.10) drops in the first few ms of the ELM cycle. However, the electric field significantly increases as a response to the bootstrap current drop, mitigating the reduction in the peak total current (solid lines in figure 4.10). This is visible in figure 4.11, where the time evolution of the parallel electric field is shown. Note that the profiles corresponding to 0 % (ELM onset) and 100 % (ELM onset of the subsequent ELM) are almost identical both in figure 4.10 and 4.11. This confirms that any long time-scale evolution of the electric field is relaxed in the simulation and the ELM cycle can be examined in steady-state.

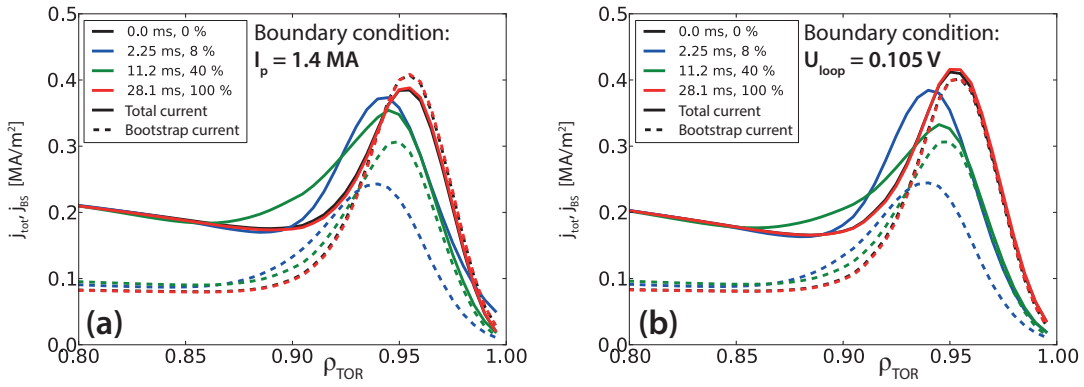

Figure 4.10: Inter-ELM evolution of the total (solid curves) and bootstrap current (dashed curves) profiles in the plasma edge for pulse #84794 ($T_\mathrm{e,PED} = 0.9$ keV). (a) The total current, (b) the loop voltage held constant as a boundary condition. The bootstrap current profile drops during the ELM crash, but the total current decreases on a slower time scale due to the increase in the electric field (see figure 4.11).

The inter-ELM evolution of the bootstrap and total current profiles with the two different boundary conditions are shown in figure 4.12a at a radial coordinate close to the peak value ($\rho_\mathrm{TOR} = 0.95$, with ρ_TOR the normalised toroidal flux). In both cases, the j_BS (dashed lines) significantly drops at the ELM crash, while the drop in the total edge current (solid lines) is relatively small and slightly delayed in time. However, in the

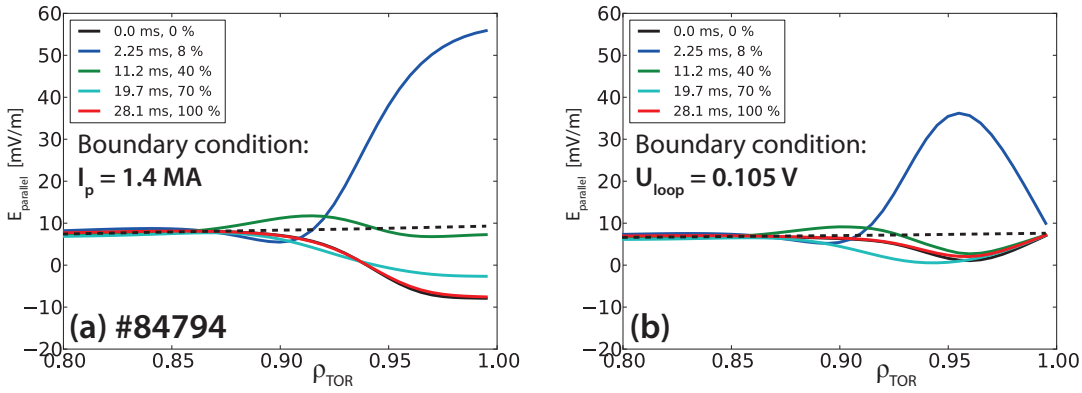

Figure 4.11: Inter-ELM evolution of the parallel electric field profiles for pulse #84794 ($T_{\mathrm{e,PED}} = 0.9$ keV). (a) Total current held constant as boundary condition, (b) loop voltage at the separatrix held constant as a boundary condition. The electric field significantly increases during the ELM crash (blue curve) as a response to the drop in the edge bootstrap current. The dashed lines show the time-average of the electric field profile over the ELM cycle, which is close to the fully diffused electric field.

second half of the ELM cycle, the peak total current builds-up on a similar timescale as the bootstrap current and the pressure gradient (see figure 4.12b).

The difference between the two simulations can be explained by the effect of the boundary condition on the time evolution of the electric field profile. The time evolution of the loop voltage at the separatrix (which is the boundary of the simulation) is shown in figure 4.12c. In the $I_p = \text{const.}$ case, $U_{\mathrm{loop}}^{\mathrm{sep.}}$ is set so that $\partial E/\partial\rho = 0$ at the separatrix (see figure 4.11a), thus the total plasma current is conserved in the system. The prescribed electric field ($U_{\mathrm{loop}} = 2\pi R_0 E$) at the separatrix also affects the electric field inside the separatrix through the first term on the r.h.s. of eq. (4.6). This difference is visible in figure 4.12a: the minimum of the total current is ~ 20 % lower in the $U_{\mathrm{loop}}^{\mathrm{sep.}} = \text{const.}$ case, as some current is lost from the plasma. This can also be seen in figure 4.12d which shows that the total plasma current is reduced after the ELM crash. Furthermore, it is visible in figure 4.11b, that $\partial E/\partial\rho < 0$ at the plasma edge after the ELM crash, implying that current is lost from the system.

The opposite process occurs in the build-up phase of the ELM cycle, thus the peak total current is higher in the $U_{\mathrm{loop}}^{\mathrm{sep.}} = \text{const.}$ case than in the $I_p = \text{const.}$ simulation prior to the ELM crash. Note that despite having the same input kinetic profiles evolution, the j_{BS} evolution is slightly different with the two different boundary conditions. This is due to the different total current profile evolution in the two simulations, which affects the j_{BS} profile through the q-profile and the collisionality.

Both simulations indicate that the electric field induced by the second and third terms on the r.h.s. of eq. (4.6) mitigates the effect of the changing bootstrap current on the

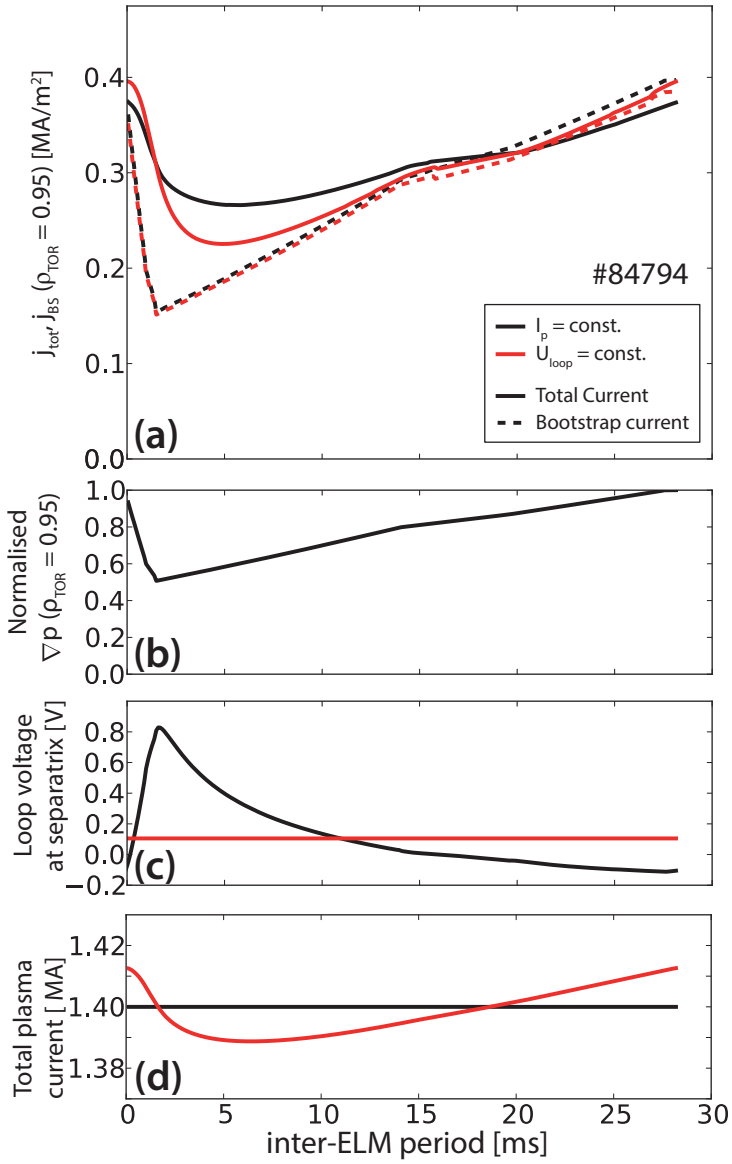

Figure 4.12: (a) Inter-ELM evolution of the total (solid curves) and bootstrap current (dashed curves) close to the position of peak j_{BS} (at $\rho_{\mathrm{TOR}} = 0.95$) in #84794. The simulation with I_p = const. boundary condition is shown in black, and with $U_{\mathrm{loop}}^{\mathrm{sep.}}$ = const. boundary condition in red. The lower panels show the inter-ELM evolution of the: (b) pressure gradient at $\rho_{\mathrm{TOR}} = 0.95$ normalised to the maximum, (c) the loop voltage at the separatrix, (d) the total plasma current.

total current evolution. As this process is present both at the ELM crash and at the recovery phase of the inter-ELM cycle, it leads to a dynamic equilibrium in which the Ohmic current is redistributed in a way that the peak total current evolution closely follows the build-up of the pressure gradient.

Eq. (4.6) and the simulation result suggest that the magnitude of the electric field oscillation at the edge during the ELM cycle is proportional to the lost bootstrap current in the ELM crash. The higher the current loss, the larger the induced electric field in the

pedestal to keep the total current constant. The opposite applies to the recovery phase of the ELM cycle: the higher the bootstrap current increase, the lower the electric field. Thus, if the ELM magnitude is large (which is likely to lead to large bootstrap current drop through low and/or wide post-ELM crash pedestal), the electric field oscillation is also high. In the JETTO simulation of #84794 the ELM magnitude is large enough (the ELM energy loss normalised to the pedestal stored energy is $\Delta W_{\mathrm{ELM}}/W_{\mathrm{PED}} \simeq 0.15$) that the electric field decreases to negative values, as can be seen in figure 4.11. This leads to higher bootstrap current than total current at $\rho_{\mathrm{TOR}} = 0.95$ in the pre-ELM phase, as shown in figure 4.12a.

Figure 4.12 suggests that the effect of current diffusion on the evolution of the total current in the second half of the ELM cycle is negligible. On the other hand, note that the electric field profile is not fully diffused by the end of the ELM cycle (see black and red curves in figure 4.11). It is expected that in a simulation with constant profiles (i.e. no ELMs) the electric field reaches a fully diffused state. In the JETTO runs presented in this chapter, the time-averaged electric field over the ELM cycle (dashed lines in figure 4.11) is very close to the fully diffused electric field which would be obtained in a time independent (i.e. no ELMs) simulation. Therefore, in what follows, I refer to this time-averaged electric field as fully diffused.[1]

In order to understand why the electric field is not fully diffused, but is lower than the time-average by the end of the ELM cycle, all 3 terms on the r.h.s. of eq. (4.6) and the boundary conditions need to be considered. As mentioned earlier in this section, $U_{\mathrm{loop}}^{\mathrm{sep.}}$ changes in the I_p = const. simulation in a way to keep $\partial E/\partial\rho = 0$ at the separatrix. It can be seen in figure 4.11a that the electric field at the separatrix is significantly lower than the fully diffused value, preventing the electric field profile from reaching the fully diffused state. On the other hand, this constraint does not exist when $U_{\mathrm{loop}}^{\mathrm{sep.}}$ is fixed in the simulation (see figure 4.11b), but also in this case the electric field profile is still not diffused by the end of the ELM cycle. This is because the third term on the r.h.s. of eq. (4.6) also plays a role in the inter-ELM evolution of the electric field. This term is inversely proportional to the rate of change of j_{BS}. Since, in pulse #84794 j_{BS} increases in the second half of the inter-ELM cycle as shown in figure 4.12a, the $\partial/\partial t = 0$ solution

[1] In stationary conditions, the loop voltage $U_{\mathrm{pl}} = \mathrm{d}\Psi/\mathrm{d}t$ evaluated at fixed ρ_{TOR} is constant in time and flat as function of ρ_{TOR} if the vacuum magnetic field is constant ($\mathrm{d}B_0/\mathrm{d}t = 0$ is the case in most present day tokamaks) [174]. In figure 4.11, the flux surface averaged parallel component of the electric field $E_\parallel = \langle E \cdot B\rangle/B_0 = U_\parallel/(2\pi R)$ is shown, thus this quantity is not exactly radially constant in steady state conditions. U_{pl} can be evaluated from $E_\parallel = 2\pi R U_\parallel$ in the following way: $U_{\mathrm{pl}} = U_\parallel \mathrm{d}V/\mathrm{d}\rho_{\mathrm{TOR}}/(4\pi^2\rho_{\mathrm{TOR}}R_0)$ [174].

of eq. (4.6) (assuming a constant, negative $-\partial j_{\mathrm{BS}}/\partial t/\sigma$ term) is smaller than the fully diffused electric field.

It is interesting to evaluate the time scale required for the electric field to reach the fully diffused state, if only the diffusion term was considered in eq. (4.6). In order to quantify this, the JETTO simulations were continued after the last ELM cycle but with constant pre-ELM profiles, as depicted with the blue shaded area in figure 4.9. This simulation represents the evolution of the electric field when only the first term on the r.h.s. of eq. (4.6) is non-zero, as conductivity and j_{BS} do not change in time when the kinetic profiles are kept constant.[2] Figure 4.13 shows the evolution of the parallel electric field close to the peak of the total current profile (at $\rho_{\mathrm{TOR}} = 0.95$). The inter-ELM evolution of $E_{\|}$ in the last ELM cycle is shown in red. The rest of the JETTO simulation when the kinetic profiles are kept constant in time and $E_{\|}$ relaxes towards the fully diffused state is in blue. It can be seen that the resistive timescale on which the relaxation process takes place is very long ($\tau_{\mathrm{res}} \sim 20$ ms).

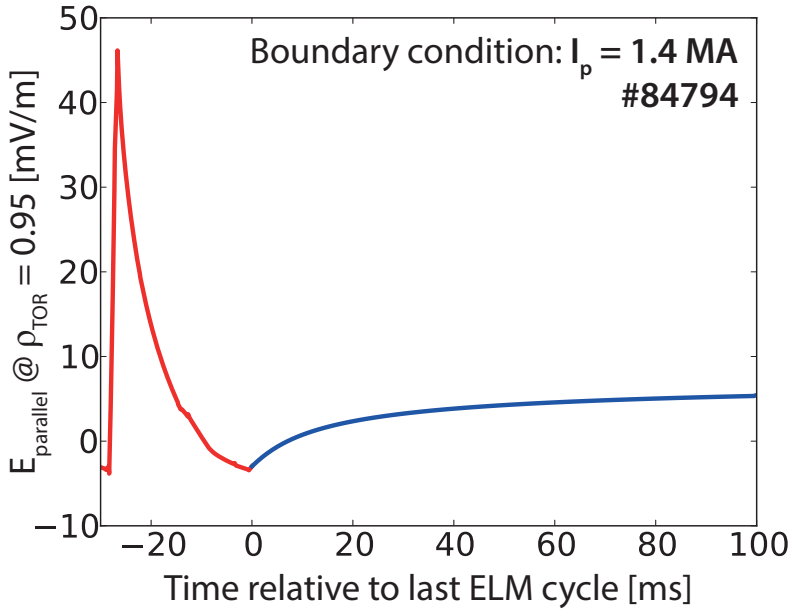

Figure 4.13: The evolution of the parallel electric field close to the peak of the total current profile (at $\rho_{\mathrm{TOR}} = 0.95$) in #84794. After the last ELM cycle (in red), the simulation continues with the kinetic profiles kept constant in time (in blue).

In conclusion, although the resistive time scale in the pedestal is comparable to the ELM period, when the whole ELM cycle (including the ELM crash) is simulated, the resulting time evolution of the peak total current in the second half of the ELM cycle closely follows that of the bootstrap current and pressure gradient, as shown in figure 4.12.

[2]Since the current diffusion modifies the total current distribution, there is also a slight change in j_{BS} through the altered q-profile, but this effect is negligible compared to the diffusive process.

This is a result of the complex interplay between the different terms of the current diffusion equation (eq. (4.6)) and the boundary conditions.

Qualitatively, similar conclusions are reached for the JET-ILW pedestal at lower pedestal temperature, but higher ELM frequency (#87342, $T_{\mathrm{e,PED}} = 0.6$ keV, $f_{\mathrm{ELM}} \simeq 120$ Hz, $\nu_{\mathrm{e,PED}} \simeq 0.9$). For this pedestal, the results of the JETTO simulations with $I_p = $ const. boundary condition is shown in figure 4.14. The inter-ELM evolution of the total and bootstrap current at a radius close to the peak j_{BS} ($\rho_{\mathrm{TOR}} = 0.95$) is shown in red and at a radius close to the pedestal top ($\rho_{\mathrm{TOR}} = 0.93$) in black. At $\rho_{\mathrm{TOR}} = 0.95$, j_{tot} reaches saturation slightly later than j_{BS} and ∇p. The time lag is less than 1 ms, thus this delay is considered non-significant compared to the inter-ELM period (≈ 8 ms). The peak j_{BS} in the second half of the ELM cycle is saturated and the total current evolves similarly, but it slightly decreases towards the end of the ELM cycle. The slight decrease in peak j_{BS} in this discharge can be understood by taking into account the bootstrap current evolution at the top of the pedestal. Figure 4.15 shows the inter-ELM evolution of the bootstrap and total current profiles. It is visible that the j_{BS} profile substantially changes inside the peak of the profile around $\rho_{\mathrm{TOR}} = 0.93$. This is also shown in figure 4.14a with black, where it can be seen that in the second half of the ELM cycle j_{BS} is roughly constant at $\rho_{\mathrm{TOR}} = 0.95$, but it increases at $\rho_{\mathrm{TOR}} = 0.93$. This increase in j_{BS} leads to a decrease in the electric field at $\rho_{\mathrm{TOR}} = 0.93$ (see figure 4.15b), which also affects the electric field evolution at $\rho_{\mathrm{TOR}} = 0.95$ through the diffusive term of eq. (4.6). The evolution of the total current in pulse #87342 shows that the effect of current diffusion on the time evolution of the total current is complex and it is not sufficient to study the profile evolution at the peak.

4.4.2 Edge current evolution at high plasma current

It is important to investigate whether the conclusions reached for the JET-ILW power and gas scans at low plasma current are still relevant for H-mode scenarios at high I_p, which are more relevant for optimising fusion performance. Thus, a representative JET-ILW pulse (#92432) was chosen to examine the inter-ELM edge current evolution in pedestals at high I_p [54]. In this pulse, good performance ($H_{98} \simeq 1$, $\beta_N \simeq 2.1$) type I ELMy H-mode operation has been achieved at $I_p = 3.0$ MA and $B_t = 2.8$ T with ≈ 33 MW auxiliary heating.

The pedestal temperature of this discharge ($T_{\mathrm{e,PED}} = 1.1$ keV) and the ELM frequency ($f_{\mathrm{ELM}} = 25$ Hz) are similar to those of the highest $T_{\mathrm{e,PED}}$ pulse in the low current scan (#84794), but the pedestal top density is roughly a factor of 2 higher in #92432

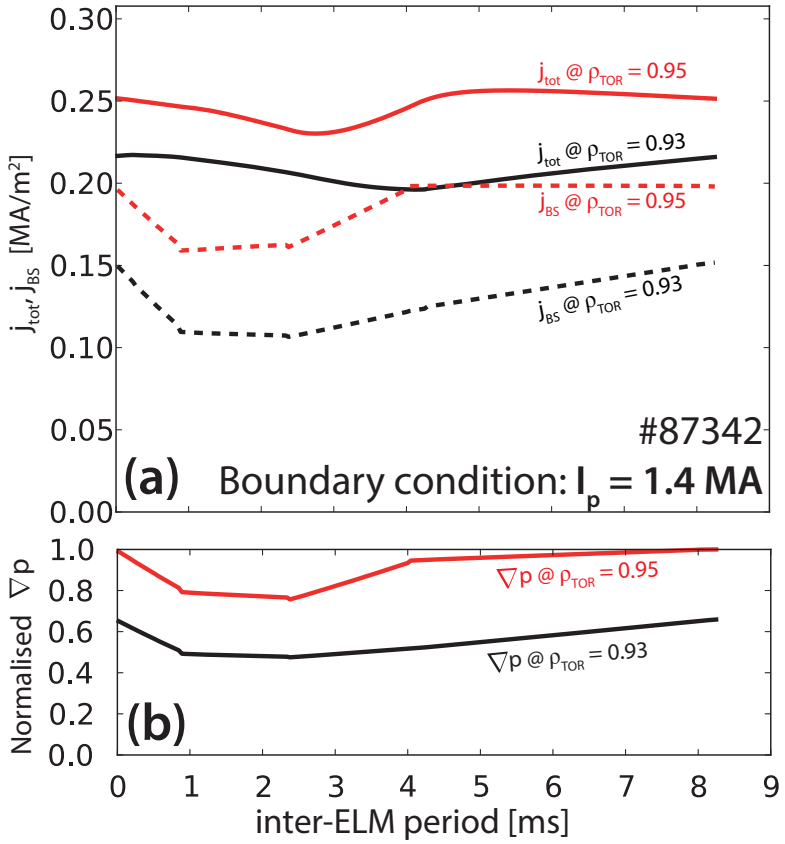

Figure 4.14: (a) Inter-ELM evolution of the total (solid curves) and bootstrap current (dashed curves) profiles at two radial coordinates close to the peak, $\rho_{\mathrm{TOR}} = 0.95$, and close to the pedestal top $\rho_{\mathrm{TOR}} = 0.93$ in #87342 with I_p = const. boundary condition. (b) The evolution of the pressure gradient in the inter-ELM cycle.

($n_{\mathrm{e,PED}} = 5.9 \times 10^{19}\mathrm{m}^{-1}$) due to the high plasma current [54]. The pressure gradient is significantly higher in #92432 compared to #84794, which leads to a higher bootstrap current at the plasma edge as shown in figure 4.16. The inter-ELM evolution of the kinetic profiles for this discharge in the pedestal has been presented elsewhere [54]. Considering that the ELM frequency and $T_{\mathrm{e,PED}}$ in #92432 are close to those of discharge #84794 (leading to similar conductivity, thus comparable current diffusion time scale), similar results are expected to those obtained for #84794. Figure 4.16a shows the bootstrap and total edge current evolution at fixed radial position close to the peak ($\rho_{\mathrm{TOR}} = 0.96$) in the ELM cycle with $I_{\mathrm{p}} = 3.0$ MA as boundary condition (in red). Similarly to the low I_p pedestals, in this case the timescales of the total and bootstrap current evolution are also very similar in the second half of the ELM cycle.

Due to the low time resolution of the measurements, the kinetic profile evolution during the ELM crash has high uncertainties. In order to account for these uncertainties, sensitivity tests on the ELM crash duration and ELM magnitude were carried out for pulse #92432. The nominal value of 1.5 ms assumed in the JETTO simulations for the ELM crash duration was determined using the ECE and interferometry measurements

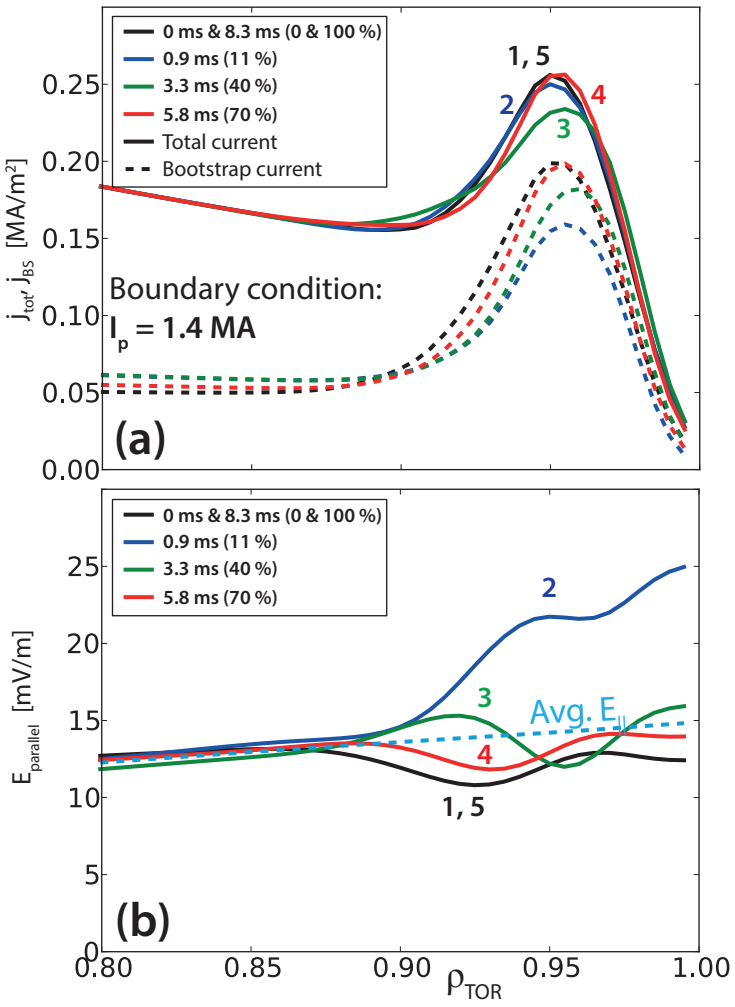

Figure 4.15: (a) Inter-ELM evolution of the total (solid curves) and bootstrap current (dashed curves) profiles in #87342 with I_p = const. boundary condition. (b) Inter-ELM evolution of the parallel electric field.

and it is consistent with the studies reported in [155]. In the sensitivity test, the ELM duration was reduced to 400 μs. Figure 4.16 shows that changing the duration of the ELM crash from 1.5 ms to 400 μs has no impact on the edge current evolution inter-ELM.

It is difficult to accurately quantify the ELM energy losses using the TS diagnostic only. Thus, the effect of an artificially increased ELM magnitude on the edge total current evolution was tested. The normalised ELM energy loss in pulse #92432 is $\Delta W_{\mathrm{ELM}}/W_{\mathrm{PED}} \simeq 0.08$ as evaluated from the fitted kinetic profiles. In the test, this was increased with a factor of 5 to $\Delta W_{\mathrm{ELM}}/W_{\mathrm{PED}} \simeq 0.4$ in order to provoke a large drop in the bootstrap current as a result of the ELM crash. The resulting inter-ELM evolutions of j_{tot} and j_{BS} are shown in blue in figure 4.16. The absolute values of the total and bootstrap currents changed significantly in the initial phase of the ELM cycle, as the average bootstrap current is reduced, however, no significant delay is found between

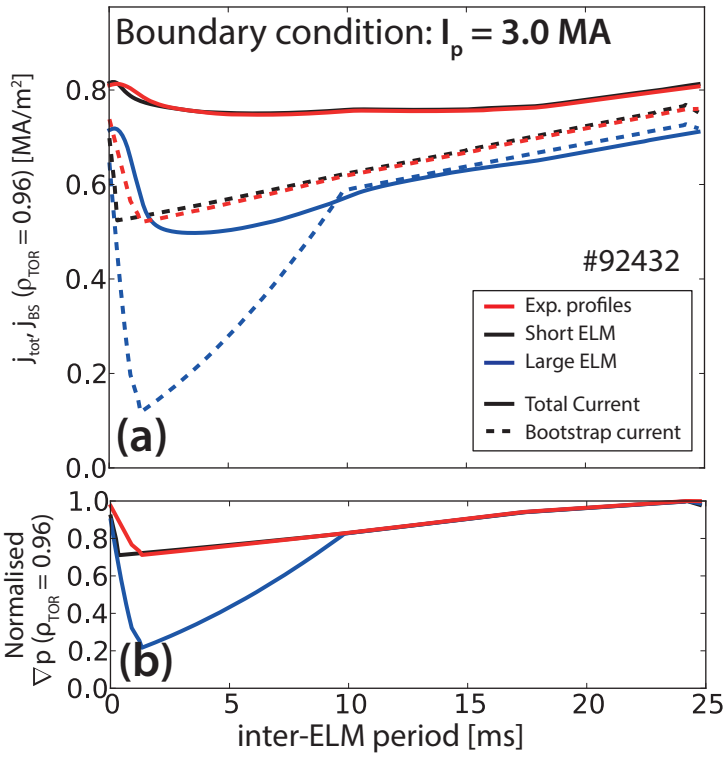

Figure 4.16: (a) Inter-ELM evolution of the total (solid curves) and bootstrap current (dashed curves) profiles at a given radial coordinate close to the peak ($\rho_{\mathrm{TOR}} = 0.96$) in the high I_p discharge (#92432) with red. Even in the case of a short ELM duration (in black) or large ELM magnitude (in blue), there is no significant delay in the total current evolution with respect to the pressure profile build-up. (b) The evolution of the peak pressure gradient in the inter-ELM cycle.

total current and j_{BS} in the second half of the ELM cycle. When the ELM magnitude is large, the associated large electric field oscillation can lead to a smaller peak j_{tot} than peak j_{BS}. This can be seen in figure 4.16a (blue curves) and in the case of pulse #84794 where $\Delta W_{\mathrm{ELM}}/W_{\mathrm{PED}} \simeq 0.15$ (see figure 4.12).

4.4.3 Impact of current diffusion on linear MHD pedestal stability

Despite the small effect of current diffusion on the evolution of the total edge current density, there are some implications of the results presented in this chapter on pedestal stability calculations. As a consequence of the dynamic equilibrium of bootstrap current and electric field profiles during the ELM cycle, the electric field in the pedestal is typically higher after the ELM crash and lower in the second half of the ELM cycle, compared to the fully diffused state. This could be important for pedestal linear MHD stability calculations, where usually a fully diffused electric field profile is assumed to evaluate the Ohmic contribution to the total current. Figure 4.17a compares the Ohmic and total edge currents for #84794 in three different cases: the two JETTO simulations with

different boundary conditions reported above and a calculation assuming fully diffused electric field profile. It can be seen that if a fully diffused electric profile is assumed, the peak total edge current is overestimated by $\sim 15-20$ % if I_p is held constant and by $\sim 5-10$ % if the loop voltage is held constant. Although this uncertainty is small compared to other uncertainties associated with edge stability analysis, this exercise shows that the boundary condition affects the absolute value of the electric field profile and the systematic error introduced in calculations assuming a fully diffused electric field profile cannot be precisely quantified without the knowledge of the experimental boundary condition.

Figure 4.17b shows a linear MHD stability diagram calculated using the HELENA/MISHKA [175] codes for the pre-ELM phase of #84794. The black circle shows the operational point as calculated with the HELENA equilibrium code using the input kinetic profiles, the Sauter-formula for the bootstrap current[3] and assuming fully diffused electric field (this corresponds to the black curves in figure 4.17a). The red and green circles show the operational point for the JETTO fixed I_p and fixed $U_{\text{loop}}^{\text{sep.}}$ simulations, respectively. The edge stability analysis was not self-consistently recalculated using the current profile outputted from JETTO, but the operational point was scaled according to the peak of the current profiles in figure 4.17a. As the shape of the total current density profile does not change significantly between the different cases in figure 4.17a, this is a good approximation to show the impact of current diffusion on P-B mode stability in the pre-ELM phase. As it can be seen in figure 4.17b, the impact of current diffusion is small compared to the uncertainties arising from the profile measurement indicated by the error bars. The error bars on the operational points were calculated with a sensitivity analysis as explained in section 4.2. The effect of current diffusion on the magnetic shear is negligible ($\simeq 5$ % at the peak of the total edge current density, $\rho_{\text{TOR}} = 0.95$). Figure 4.17c shows the shear at the plasma edge from the JETTO simulation with fixed I_p in red and from the fully diffused electric field assumption in black. This comparison is outputted from the simulation shown in figure 4.13: the red curve corresponds to the end of the ELM cycle, the black curve shows the magnetic shear 100 ms later when the electric field is fully diffused at the edge.

In summary, although the current diffusion simulations show that the resistive timescale is comparable to the ELM period in the investigated pedestals, when the

[3] The equilibrium for the MISHKA stability analysis is calculated with the HELENA code in a self-consistent way, namely that the bootstrap current and the equilibrium are calculated iteratively until the solution converges. The result of the Sauter formula for the calculation of j_{BS} is in good agreement with that of NEO for the low collisionality pedestal of #84794. Thus, the usage of the Sauter formula in HELENA provides a sufficiently accurate and quick way to produce the equilibrium in this case.

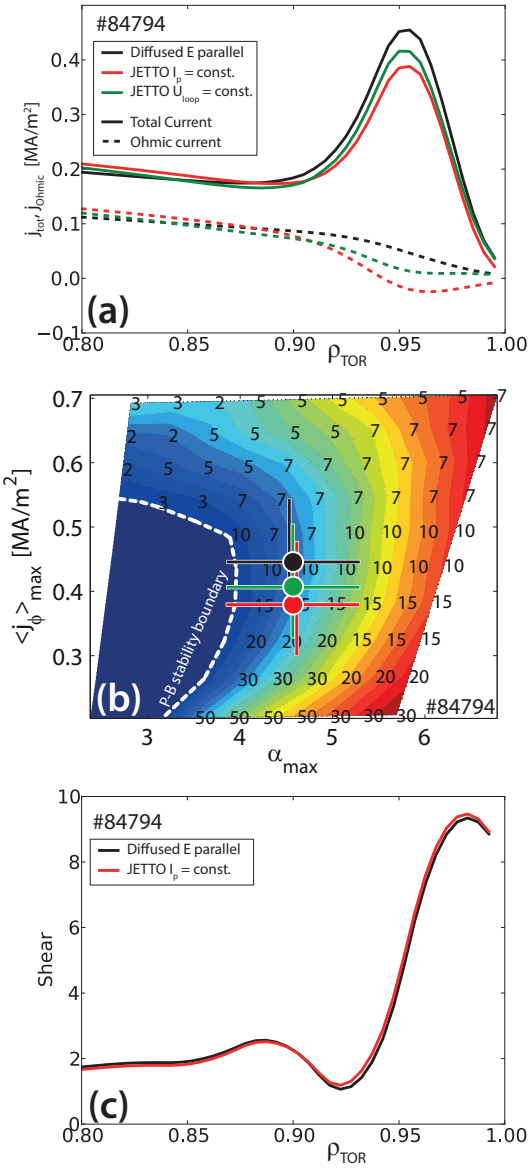

Figure 4.17: (a) Comparison of the edge total and Ohmic currents in the last 20 % of the ELM cycle in the highest $T_{\mathrm{e,PED}}$ pulse (#84794): j_{tot} (solid lines) and j_{OH} (dashed lines) when the Ohmic contribution is calculated assuming a fully diffused electric field profile (black); j_{tot} and j_{OH} when simulated in JETTO using constant total current (red) and constant loop voltage (green) as boundary condition, respectively. (b) Result of linear MHD stability analysis for #84794. The operational point was scaled to show the impact of current diffusion on P-B mode stability in the pre-ELM phase. The y axis in figure 4.17b is the maximum of the toroidal component of the total current density, the x axis is the ballooning α. (c) The magnetic shear from the JETTO simulation with fixed I_p (red) and from the fully diffused electric field assumption (black) are compared.

full ELM cycle (including the ELM crash) is simulated, the Ohmic current is always redistributed so as to mitigate the effect of the varying bootstrap current. As a result, the effect of current diffusion on the time evolution of the total edge current is not significant in the second half of the ELM cycle. Therefore, inter-ELM current diffusion does not

explain why JET-ILW pedestals at high gas rate and medium to high β_N are stable to P-B modes, as found by linear MHD stability analysis with HELENA/ELITE [53].

One caveat of the simulations with JETTO is that the plasma shape and size are fixed during the simulation. Although the effect of total plasma current loss was investigated in the simulations with constant $U_{\text{loop}}^{\text{sep.}}$, no current loss through filaments or fast loss of a current-carrying plasma layer during the ELM crash were modelled.

Accurate modelling of the total edge current profile evolution requires a precise knowledge of the evolution of the kinetic profiles (including the ELM crash) and an accurate measurement of the loop voltage at the separatrix for the boundary condition. Without these it is difficult to quantify the effect of the Ohmic current contribution on pedestal stability analysis, although some qualitative conclusions can be made. Generally, linear MHD pedestal stability calculations estimate the contribution of the Ohmic current by assuming a fully diffused electric field profile. However, as a result of the dynamic equilibrium of the bootstrap current and electric field profiles in the ELM cycle, the electric field in the pedestal is typically larger in the early phase, and lower in the second half of the ELM cycle compared to the fully diffused state. Therefore, the assumption of a fully diffused electric field may overestimate the total current in the pre-ELM phase. This work estimates this error to be of order of 10-20 % at the maximum of the total current density profile in the pedestal. Although, this uncertainty error is not large, it adds to all other uncertainties that feed into the edge stability analysis, such as those arising from the profile measurements and the bootstrap current models. In addition, as a consequence of the large profile changes in the first half of the ELM cycle, the fully diffused electric field assumption can potentially lead to higher errors in this phase. This might have an impact on pedestal stability analysis such as presented in [82, 156], where the stability of the $n = \infty$ ideal MHD ballooning mode as a proxy for Kinetic Ballooning Mode was investigated during the inter-ELM cycle.

Chapter 5

Pedestal structure in JET-ILW H and D type I ELMy H-modes

This chapter presents the differences in pedestal structure between H and D pedestals in JET-ILW type I ELMy H-modes at low plasma triangularity ($\delta \approx 0.2$) with mostly NBI heating. This study focuses on type I ELMy H-modes only, the separation between type I and type III ELMy H-modes in these plasmas has already been reported in [104]. The H and D isotope dataset includes power ($P_{\mathrm{NBI}} = 3 - 16$ MW) and gas scans at two different plasma current and magnetic field combinations (1.0 MA/1.0 T with $q_{95} = 3.0$ and 1.4 MA/1.7 T with $q_{95} = 3.7$), $\beta_N = 1.3 - 2.8$. Hereinafter, the H_2/D_2 gas rates will be referred to as "low" $= 3 - 4.5 \cdot 10^{21}$ e/s, "medium" $= 8 - 10 \cdot 10^{21}$ e/s and "high" $= 16 - 18 \cdot 10^{21}$ e/s. NBI was operated with the ion species of the plasma (H-NBI in H and D-NBI in D plasmas). The plasma isotope purity was higher than 97 % both in H and D, as measured by Balmer-α spectroscopy at the plasma edge.

The majority of the dataset is in the so-called "Corner" or C/C divertor configuration (see figure 4.3), where both divertor strike points are close to the pumping duct. One power scan (1.4 MA/1.7 T, at low gas rate) is in the so-called V/H configuration, where the inner strike point is on the vertical target and outer strike point is on the horizontal target. Due to a 2-3 fold increase in sub-divertor neutral pressure, and thus improved cryo-pumping, operation in C/C configuration leads to a $10 - 15$ % decrease in $n_{\mathrm{e,PED}}$ and a similar increase in $T_{\mathrm{e,PED}}$ at similar $p_{\mathrm{e,PED}}$ values than in V/H configuration [53]. In the present chapter, the two different divertor configurations are treated together as the main scope of this paper is to present the differences between H and D plasmas. The effect of divertor configuration on the pedestal parameters has already been published in [53].

The pedestal structure in the D plasmas of the 1.4 MA/1.7 T dataset has already been characterised elsewhere [53, 54], but here some of those findings are recalled for comparison with the H plasmas. First, the ELM frequency (f_{ELM}) as a function of the power crossing the separatrix (P_{sep}) is shown in figure 5.1 to demonstrate the type I nature of the ELMs and to show some other important features in the dataset. In the 1.4 MA/1.7 T dataset f_{ELM} increases with P_{sep} and f_{ELM} is higher in H than in D at a low gas rate at given input power (figure 5.1a). Note that NBI heating was limited to 10 MW in H in order to maintain the power load on the ion dump of the NBI within engineering limits [45]. Thus in the "medium" and "high" gas H plasmas at 1.4 MA/1.7 T, 2-5 MW ion cyclotron resonance heating (ICRH: 51 MHz, H majority, 2nd harmonic) was added to the heating mix to reach type I ELMy H-modes, which is expected to lead to an increase in f_{ELM} compared to NBI only plasmas [176]. All other plasmas were NBI heated only.

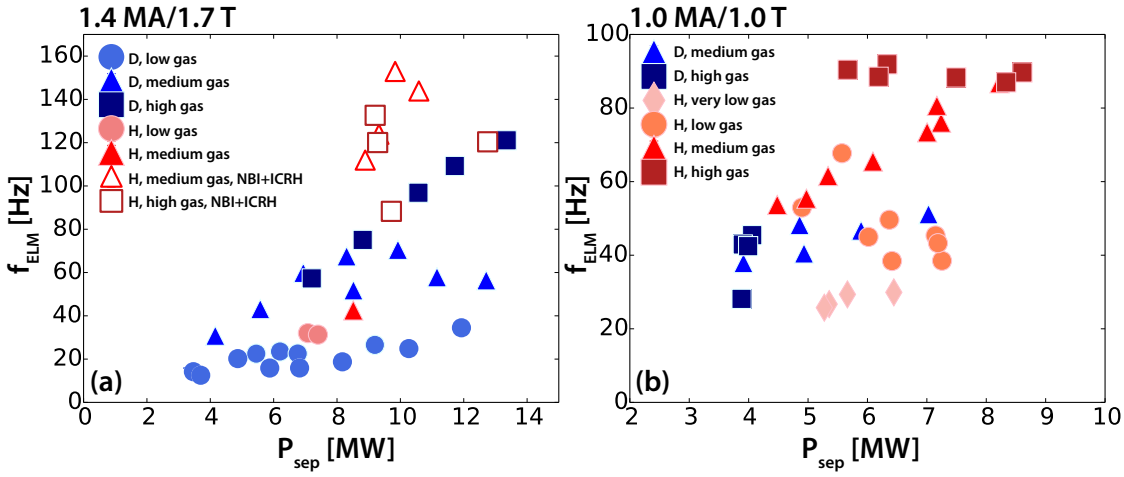

Figure 5.1: ELM frequency as a function of net power crossing the separatrix for the (a) 1.4 MA/1.7 T and the (b) 1.0 MA/1.0 T dataset. Note that most of the medium and high gas pulses at 1.4 MA/1.7 T (open symbols on figure (a)) were heated also with ICRH.

At 1.0 MA/1.0 T two different "low" gas levels are distinguished: "very low" $= 3 \cdot 10^{21}$ e/s and "low" $= 4.5 \cdot 10^{21}$ e/s. As it is visible in figure 5.1b, f_{ELM} decreases with P_{sep} for the "low gas" power scan and is constant for the "high gas" power scan. Despite the f_{ELM} behaviour, other parameters such as β_N and the ELM signature in the divertor Be II ($\lambda = 527$ nm) photon flux suggest that these pulses are in the type I ELMy regime. It is possible that the decreasing trend of f_{ELM} with the input power for the "low gas" dataset is a consequence of the density being very close to the point where the type III-type I ELMy power threshold ($P_{\mathrm{III-I}}$) "rolls over" from the low density branch to the high density branch and the small density variation between pulses could lead to

some plasmas accessing type I ELMy H-mode from the low density branch, while others from the high density branch. In the low density branch, $P_{\mathrm{III-I}}$ increases very rapidly with decreasing density. Thus, a given P_{sep} is closer to the type III to type I power threshold in the low than in the high density branch. This may lead to lower f_{ELM} in the low density branch than in the high density branch even at higher P_{sep}, resulting in the observed decreasing trend of f_{ELM} with the input power. In D, at 1.0 MA/1.0 T stable H-mode operation was not possible at "low gas" rate due to W and mid-Z impurity accumulation in the core. The "medium gas" power scan with a factor of 2 variation in P_{sep} provides a good basis for comparison between H and D at this plasma current (I_p) and magnetic field (B_t), thus the analysis of the 1.0 MA/1.0 T dataset will mostly focus on these data.

The pedestal structure analysis is carried out for the pre-ELM phase (namely the last 20 % of the ELM cycle) and is based on the mtanh fitted electron density (n_e) and temperature (T_e) profiles as measured by Thomson scattering (TS). The kinetic profiles, collected from a steady time window ($> 10 \times \tau_{\mathrm{E,th}}$) of the discharge, are ELM-synchronised to improve signal statistics. The width and height of the pedestal electron density and temperature are taken directly from the mtanh fit. The error bars on the pedestal structure parameters are defined as the standard deviation of the parameter estimates of the mtanh fit.

5.1 Pedestal height

Figure 5.2 shows the electron pedestal pressure ($p_{e,PED}$ [Pa] = 1.602 × $n_{e,PED}$ [$10^{-19}\mathrm{m}^{-3}$] × $T_{e,PED}$ [eV]) as a function of P_{sep}. Both at 1.0 MA/1.0 T and 1.4 MA/1.7 T, $p_{\mathrm{e,PED}}$ decreases with increasing gas rate both in H and D. In general, $p_{\mathrm{e,PED}}$ is higher in D than in H at a given P_{sep}.

At 1.0 MA/1.0 T and medium gas rate $p_{\mathrm{e,PED}}$ is comparable in H and in D, but the total thermal stored energy is still higher in D. This is due to higher T_e peaking in D than in H, when the core temperature is compared to $T_{\mathrm{e,PED}}$ as shown in figure 5.3a. However, when T_e peaking is defined as $T_e(\rho_{\mathrm{TOR}} = 0.3)/T_e(\rho_{\mathrm{TOR}} = 0.8)$, the difference between H and D diminishes as shown in figure 5.3b, which is consistent with R/L_{T_e} being similar at $\rho_{\mathrm{TOR}} = 0.5$ as shown in figure 18 in [104]. This can also be seen in figure 5.4, where the electron kinetic profiles on a log scale are shown for a pair of H and D pulses at the same P_{sep} as a representative example. Gradient lengths in the core are very similar and any difference in the temperature gradient length arises at $\rho_{\mathrm{TOR}} > 0.8$. Therefore, for the 1.0 MA/1.0 T medium gas rate dataset as well, the difference in thermal energy

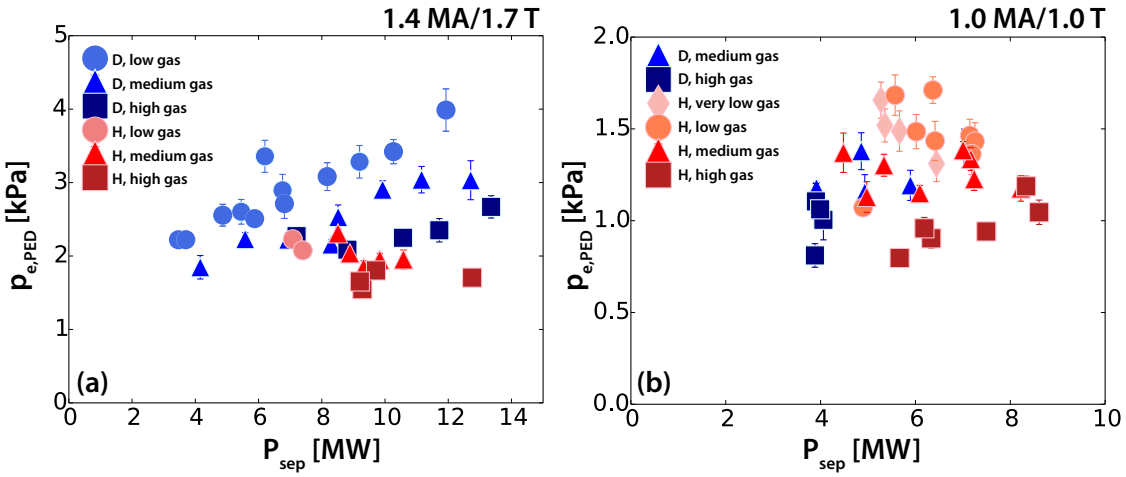

Figure 5.2: The electron pressure at the pedestal top as a function of net power crossing the separatrix for the (a) 1.4 MA/1.7 T and the (b) 1.0 MA/1.0 T dataset.

confinement between H and D is emerging at the edge, but in this case it is not well represented by the pedestal top values as derived from the mtanh fit. This may be due to the lack of TS data in H just inside the pedestal, which could lead to higher uncertainties in the profile fitting method.

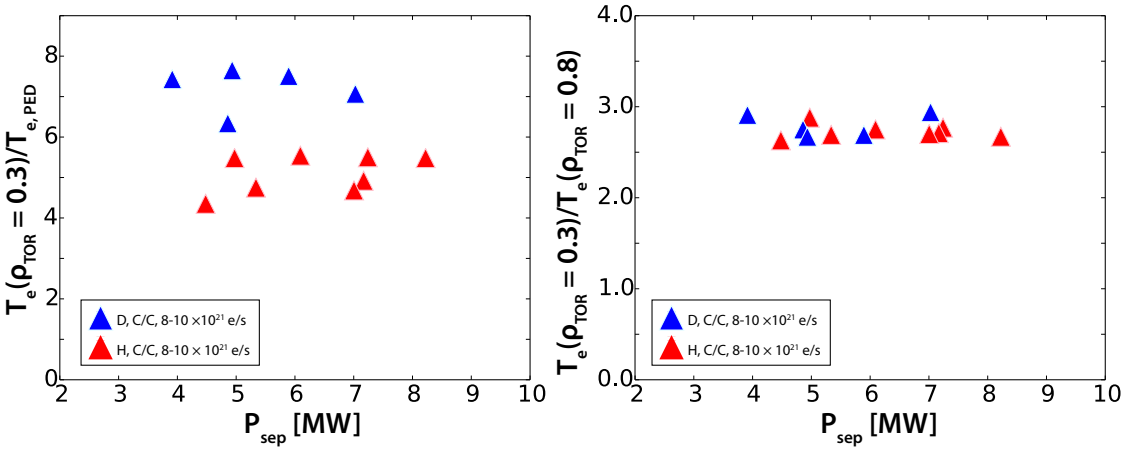

Figure 5.3: T_e peaking in the 1.0 MA/1.0 T medium gas dataset defined in two different ways: (a) $T_e(\rho_{\mathrm{TOR}} = 0.3)/T_{\mathrm{e,PED}}$ and (b) $T_e(\rho_{\mathrm{TOR}} = 0.3)/T_e(\rho_{\mathrm{TOR}} = 0.8)$.

The ion temperature (T_i) is similar to T_e at the pedestal top within the measurement uncertainties of the edge CXRS system. Discharges with good T_i data in the pedestal gradient region confirm $T_e \approx T_i$, although T_i at the separatrix cannot be resolved. The line-averaged Z_{eff} in the 1.4 MA/1.7 T dataset varies between 1.1 and 1.5 for D and between 1.2 and 1.8 for H. For the 1.0 MA/1.0 T dataset it varies between 1.2 and 1.4 for D and between 1.1 and 1.4 for H. Assuming Be as single impurity and $T_e = T_i$, the ion dilution leads to at most 10 % difference between the total pressure (calculated as $p = p_e + p_i$) and $2 \times p_e$, thus the conclusions drawn from the analysis of the electron pressure also apply to the total pressure.

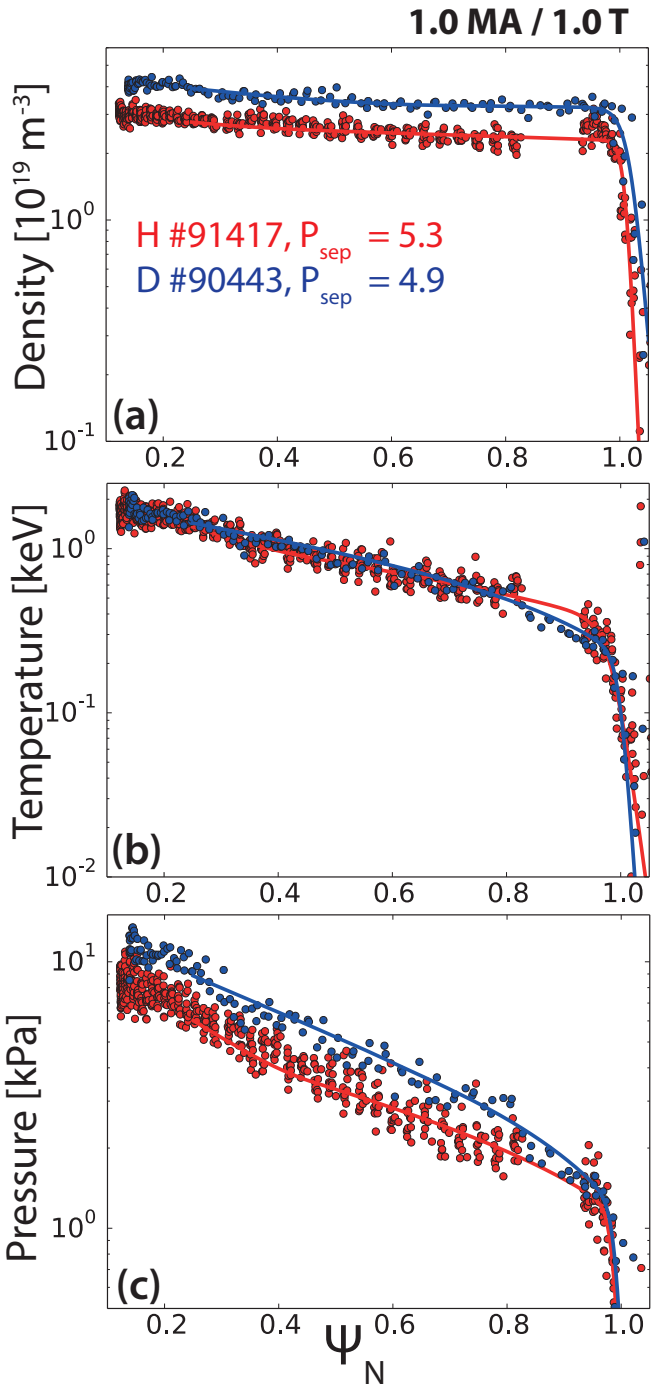

Figure 5.4: Pre-ELM (80-100 % of the ELM cycle) electron kinetic profiles from TS for a pair of H (#91417, in red) and D (#90443, in blue) pulses at 1.0 MA/1.0 T at the same P_{sep} as a representative example. (a) Electron density, (b) electron temperature and (c) electron pressure are shown on a log scale to compare the gradient lengths in the core. Profiles are radially shifted to have $T_{\mathrm{e,sep}} = 100$ eV.

The edge n_e-T_e diagram in figure 5.5 shows that the pedestal density is typically lower in H than in D. Pedestals at the same $p_{\mathrm{e,PED}}$ (typically obtained with more heating power in H than in D) have lower density, but higher temperature in H compared to D. In other words, by varying input power and/or gas rate it was not possible to simultaneously match n_e and T_e in H and D, as for example in JT-60U experiments [83, 105, 106].

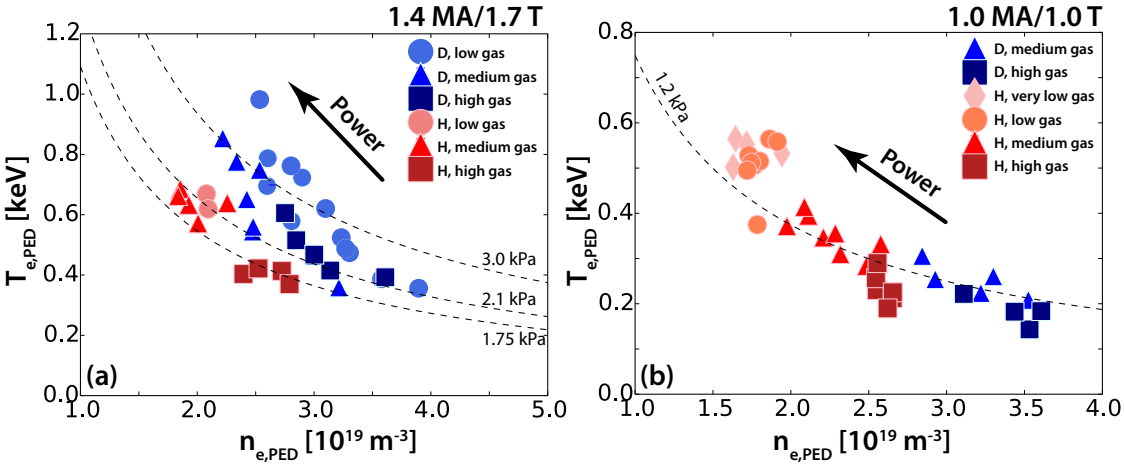

Figure 5.5: $n_{\mathrm{e,PED}}$-$T_{\mathrm{e,PED}}$ diagram for the (a) 1.4 MA/1.7 T and the (b) 1.0 MA/1.0 T dataset. The dashed black lines are isobars at a pressure level indicated in the figure.

5.2 Pedestal gradient

The peak pedestal pressure gradient is comparable in H and D within error bars at the same pedestal top poloidal beta ($\beta_{\mathrm{pol,PED}}$) at both plasma current levels, as shown in figure 5.6. However, at 1.4 MA/1.7 T ∇n_e is lower and ∇T_e is higher in H compared to D (see figure 5.7a for ∇n_e and figure 5.8a for ∇T_e), while at 1.0 MA/1.0 T ∇n_e and ∇T_e are comparable in H and D (see figure 5.7b for ∇n_e and figure 5.8b for ∇T_e). At 1.4 MA/1.7 T, ∇p_e increases with increasing $\beta_{\mathrm{pol,PED}}$ and more power is needed in H than in D to reach the same $\beta_{\mathrm{pol,PED}}$, thus ∇p_e is typically larger in D than in H at the same P_{sep}.

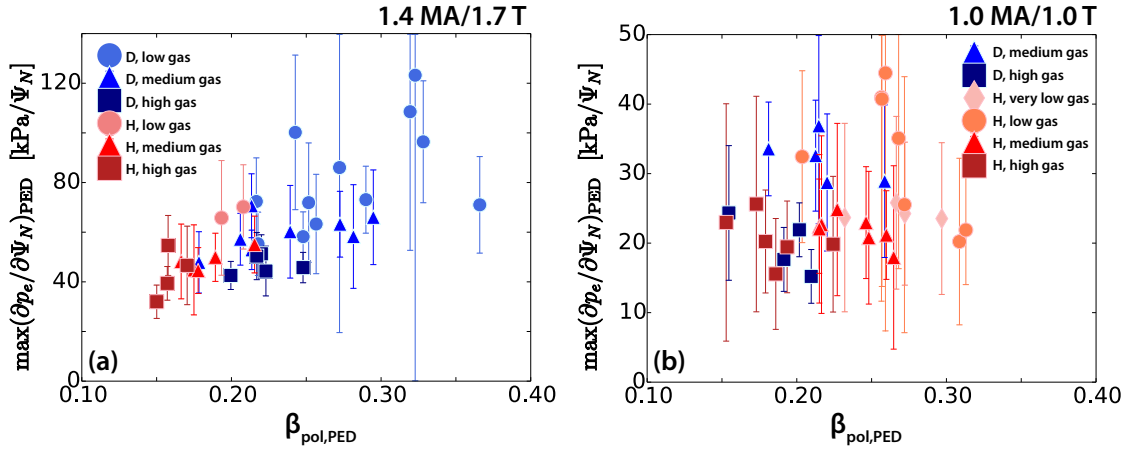

Figure 5.6: The peak electron pressure pedestal gradient (∇p_e) as a function of $\beta_{\mathrm{pol,PED}}$ for the (a) 1.4 MA/1.7 T and the (b) 1.0 MA/1.0 T dataset.

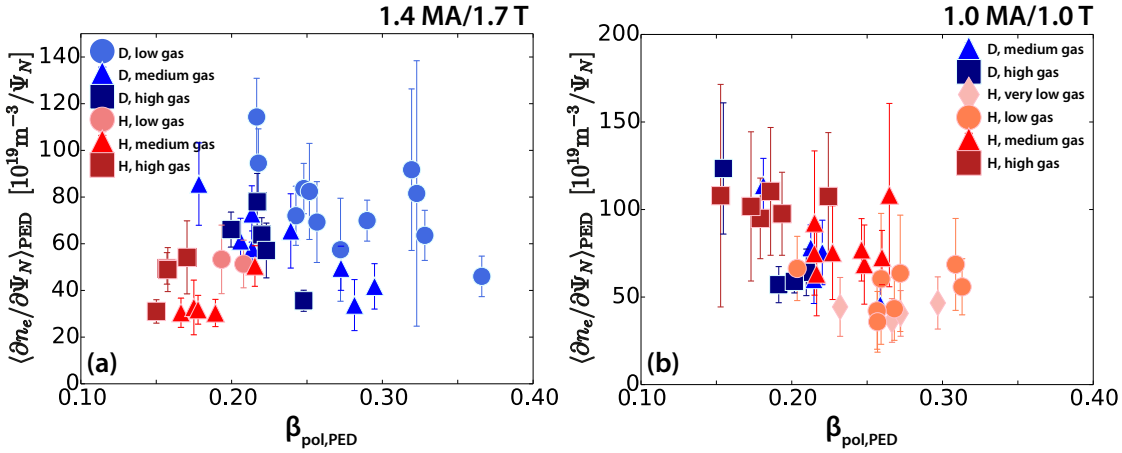

Figure 5.7: The average density pedestal gradient (∇n_e) as a function of $\beta_{\mathrm{pol,PED}}$ for the (a) 1.4 MA/1.7 T and the (b) 1.0 MA/1.0 T dataset. $\nabla n_e = n_{\mathrm{e,PED}}/\Delta n_e$.

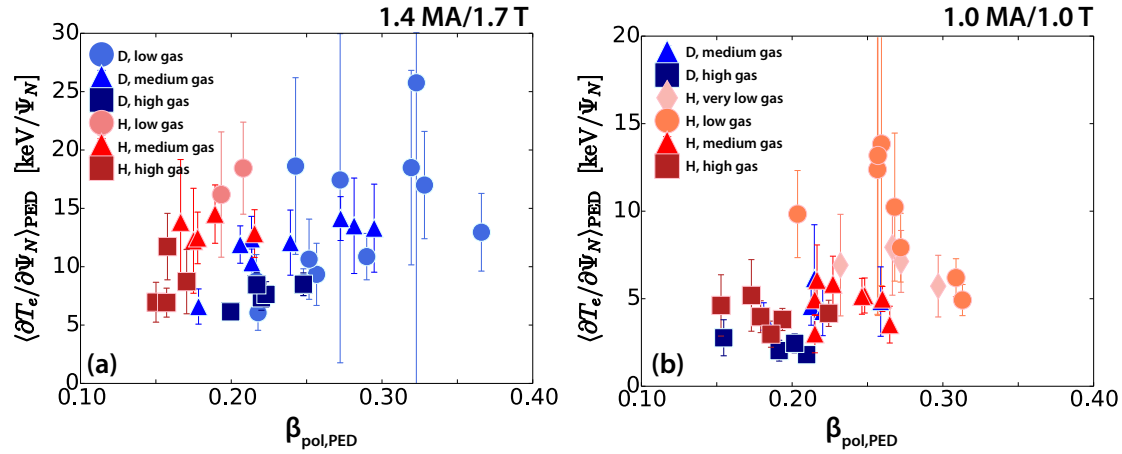

Figure 5.8: The average electron temperature pedestal gradient (∇T_e) as a function of $\beta_{\mathrm{pol,PED}}$ for the (a) 1.4 MA/1.7 T and the (b) 1.0 MA/1.0 T dataset. $\nabla T_e = T_{\mathrm{e,PED}}/\Delta T_e$.

5.3 Pedestal width

The pedestal pressure width, defined here as $\Delta n_e/2 + \Delta T_e/2$[1], has a much larger variation at a given $\beta_{\mathrm{pol,PED}}$ than is expected by the EPED model ($\Delta p_{\mathrm{e,PED}} = c_{\mathrm{EPED}} \times \beta^{1/2}_{\mathrm{pol,PED}}$ with $c_{\mathrm{EPED}} = 0.076$ [76]) both in H and D as shown in figure 5.9. $\beta_{\mathrm{pol,PED}}$ is the poloidal normalised pressure at the pedestal top calculated using the expression given by [87, 177]. At 1.4 MA/1.7 T Δp_e broadens with increasing gas rate at constant $\beta_{\mathrm{pol,PED}}$, which is not consistent with EPED (with constant width multiplier c_{EPED}) [54, 177]. No clear trend with $\beta_{\mathrm{pol,PED}}$ is observed in the variation of Δp_e at 1.0 MA/1.0 T. The difference in $p_{\mathrm{e,PED}}$ between H and D at the same P_{sep} at 1.4 MA/1.7 T (shown in figure 5.2a) is mainly due to lower ∇p_e in H than in D and similar pedestal p_e width.

[1]The EPED pedestal pressure width definition [76] is used here for comparison with the EPED pedestal width scaling. Δn_e and ΔT_e are the full widths of the mtanh profiles, not only the part up to the LCFS.

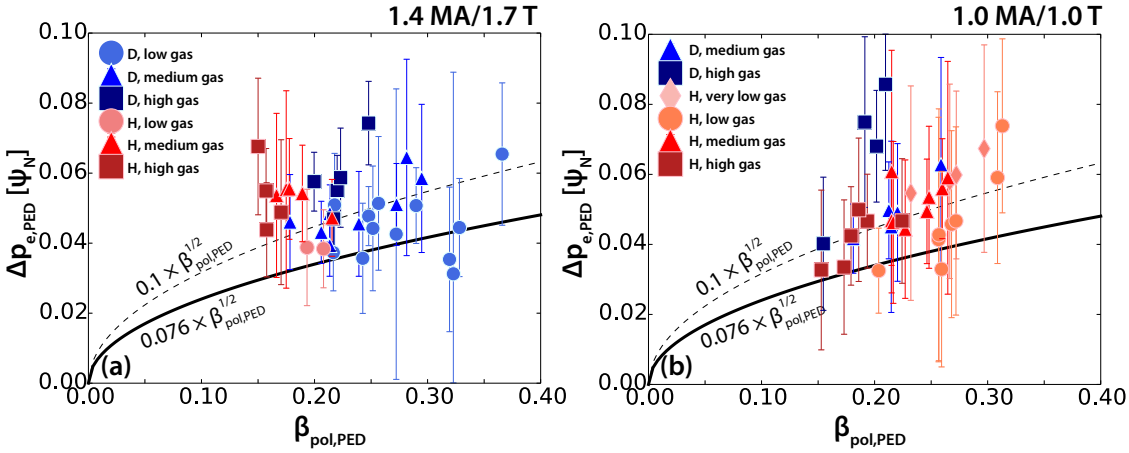

Figure 5.9: The electron pressure pedestal width in normalised poloidal flux (Ψ_N) for the (a) 1.4 MA/1.7 T and the (b) 1.0 MA/1.0 T dataset. The solid black lines indicate the $0.076 \times \beta_{\mathrm{pol,PED}}^{1/2}$ EPED scaling [76] and the dashed black lines indicate the $0.1 \times \beta_{\mathrm{pol,PED}}^{1/2}$ curve to show the variation in the dataset.

5.4 Edge density profile and neutral fuelling

It is anticipated that the penetration of neutrals and the resulting particle source at the edge of the plasma could be an important mechanism in setting the density pedestal. Indeed, the neutral penetration model (NPM) assumes that the pedestal density is set by the edge particle flux and that the pedestal width is approximately equal to the neutral penetration length [97]. This model is tested here against the experimental pedestal density width of H and D plasmas. At similar temperature, H neutrals have a higher thermal speed than D neutrals, thus larger mean free path and neutral penetration length is expected in H. According to the NPM this should lead to a wider density pedestal in H.

The neutral penetration model [97] describes the width of the density pedestal as

$$\Delta_{n_e} = \frac{2V_N}{S_i E n_{e,ped}} \ , \tag{5.1}$$

where Δ_{n_e} is the pedestal width at the midplane (in real units), V_N is the neutral velocity, E is a flux expansion parameter, $n_{e,ped}$ is the pedestal top density and S_i is the ionisation rate, which is approximated as $\sigma_i V_e$ [97] with σ_i the cross section for electron impact ionisation and V_e the electron thermal velocity. If the fuelling location is maintained, $T_e/T_i \approx$ constant and assuming that the neutrals are in equilibrium with the ions, the NPM predicts the following relation between Δ_{n_e} and $n_{e,ped}$:

$$\Delta_{n_e} \sim \frac{1}{\sqrt{A} n_{e,ped}} \ . \tag{5.2}$$

This assumption can easily be tested against the experimental pedestals analysed in the present paper. Previous JET-ILW studies in D plasmas indicated that for some datasets at low δ, Δ_{n_e} is broadly consistent with the $1/n_{e,ped}$ dependence of the pedestal density, while for other cases (for example a high δ dataset [54] or a dimensionless ν^* scan [178]) the density pedestal broadens at roughly constant $n_{e,ped}$, in contradiction to the assumptions of the NPM.

In figure 5.10 $\Delta n_e \times \sqrt{A}$ is shown as a function of $n_{e,ped}$ for the H and D pedestals discussed in this section. At 1.0 MA/1.0 T (figure 5.10b), the pedestal width in H follows the $1/n_{e,ped}$ scaling at all fuelling gas rates, but the pedestals are significantly narrower in H than in D in contradiction to the NPM. Figure 5.10a shows the comparison for the 1.4 MA/1.7 T dataset, where the result depends on the gas fuelling rate. At low gas rate (circles), the H pedestals are narrower than the D pedestals, in contradiction to the NPM. At medium (triangles) and high (squares) fuelling gas rates, Δn_e is similar in H and D in accordance with the NPM. In summary, this comparison of the experimental observations with the NPM suggests that the changes in neutral fuelling due to the change of the isotope mass is not sufficient to fully describe the difference in pedestal density between H and D. Inter-ELM pedestal transport and/or ELM losses must also play a role. This is also supported by the interpretative EDGE2D-EIRENE simulations, which will be discussed in section 6.3. Results indicate that the difference in the kinetic profiles between H and D is due to significantly higher perpendicular particle and heat diffusivities at the edge in H than in D.

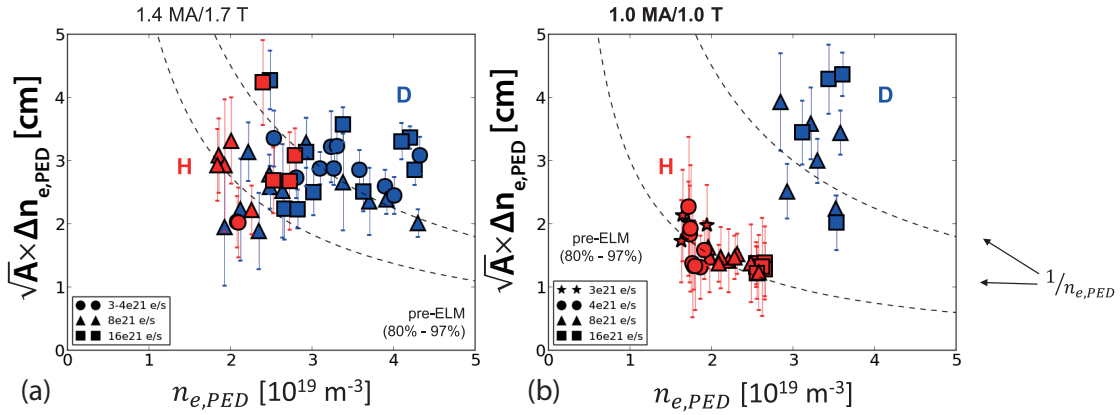

Figure 5.10: $n_{e,width} \times \sqrt{A}$ as a function of $n_{e,ped}$ for the (a) 1.4 MA/1.7 T and the (b) 1.0 MA/1.0 T datasets.

5.5 Ratio of the electron density and temperature gradient length

In view of recent gyrokinetic analysis of the pedestal in JET with Carbon wall (JET-C) and JET-ILW [99, 102, 171], I compare the ratio of the electron density and temperature gradient length η_e between H and D plasmas. $\eta = L_{n_e}/L_{T_e}$, with $L_{n_e} = n_e/\nabla n_e$ and $L_{T_e} = T_e/\nabla T_e$ being the density and temperature gradient lengths, respectively. The growth rate of temperature gradient driven micro turbulence is expected to increase with η_e, generating increasing levels of heat transport inside the pedestal [99, 102]. It has been reported in [99] and [102] that the degradation of the temperature pedestal in JET-ILW, where significant gas injection is needed for core W control, can partly be explained by an increase in η_e and η_i in JET-ILW producing more robust slab-like ion temperature gradient (ITG) and electron temperature gradient (ETG) instability, leading to limited pedestal temperature and demanding more heating power to achieve similar pedestal pressure as in JET-C. The experimental characterisation of η_e for the JET-ILW H and D isotope dataset is attempted here, in order to collect any evidence for differences in the inter-ELM transport between H and D pedestals, which may shed light on the physics mechanism behind the lower H pedestals.

η_e is calculated here in two different ways. In one case, η_e is evaluated from the mtanh fit of the T_e and n_e TS profiles for the pre-ELM pedestals in a region $0.02\Psi_N$ wide around the centre (peak gradient) of the T_e pedestal.[2] A representative example is shown in figure 5.11 for discharge #84793. It shows the fitted pre-ELM n_e and T_e profiles in figures a and b, respectively, and the calculated η_e in figure c. The colour scales indicate Ψ_N, which will be useful for comparison with subsequent figures. It is clear from figure 5.11c that the variation of η_e at the plasma edge is high and this is typical for the whole dataset. The $0.02\Psi_N$ wide region around the centre of the T_e pedestal, from where the η_e values are taken for this type of analysis is shown with the grey area in figure 5.11.

Another way of calculating η_e utilises the TS data directly without any regularisation introduced by the mtanh fit. Given that η_e can be expressed as

$$\eta_e = \frac{\mathrm{d}\log(n_e)}{\mathrm{d}\log(T_e)} \ , \tag{5.3}$$

[2]The temperature pedestal width is typically $> 0.03\Psi_N$ in the dataset, thus the $0.02\Psi_N$ wide region only covers the gradient region and not the "knee" and the "bottom" of the pedestal.

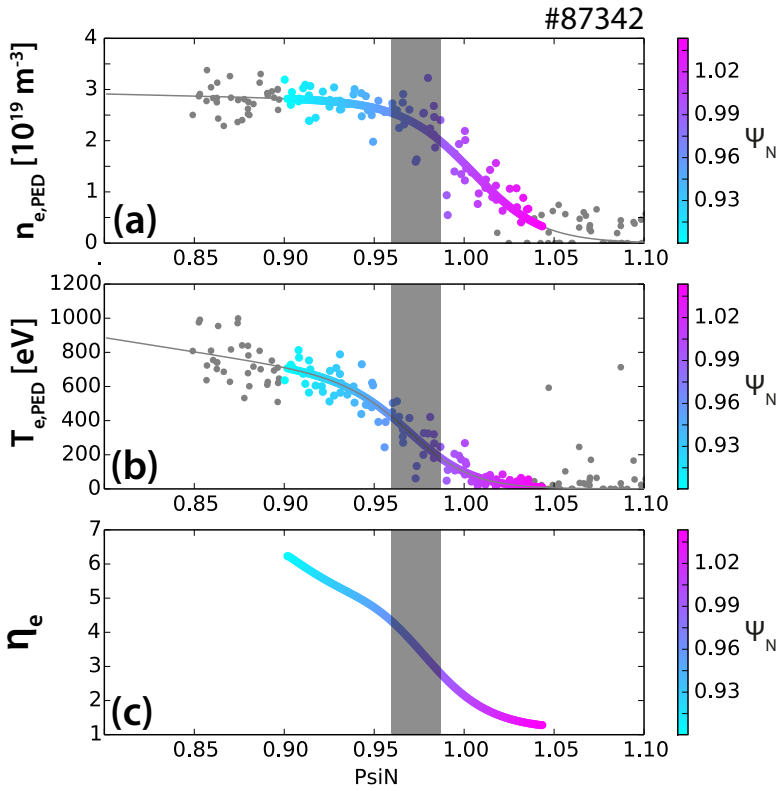

Figure 5.11: Fitted pre-ELM n_e and T_e profiles in figures a and b, respectively, and the calculated η_e in figure c for discharge #87342. The colour scales indicate Ψ_N for comparison with figure 5.13b.

in this method the gradient of $\log(n_e)/\log(T_e)$ is analysed. This method also exploits that there is no relative uncertainty in the position of n_e and T_e measurements from TS. Figure 5.12 shows T_e as a function of n_e for the pre-ELM pedestal TS data from the pedestal top to the foot on a logarithmic scale for discharge #87342. A linear fit to the data was obtained taking into account the uncertainties both in n_e and T_e. The slope of the linear fit provides an estimate for η_e in the pedestal.

The results of the two methods are compiled in figure 5.13. for comparison. Both figure a and b show the TS data points on a logarithmic scale in black and the linear fit in red. The η_e profile evaluated from the mtanh fits is also shown in these figures in colors. In figure 5.13a, the color scale indicates η_e, while it shows Ψ_N in figure 5.13b. It is clear from figure 5.13 that the η_e profile estimate from the mtanh fits implies a large variation in the pedestal, which is not captured by the linear fit.

In the following figures η_e is compared for the H and D dataset with both methods. For the mtanh fit estimate, given that the variation of the η_e profile is typically large in the pedestal, in figure 5.14 ranges of η_e between the lowest and highest values in the $0.02\Psi_N$ wide region are compared. For the linear fit estimate (shown in figure 5.15), the

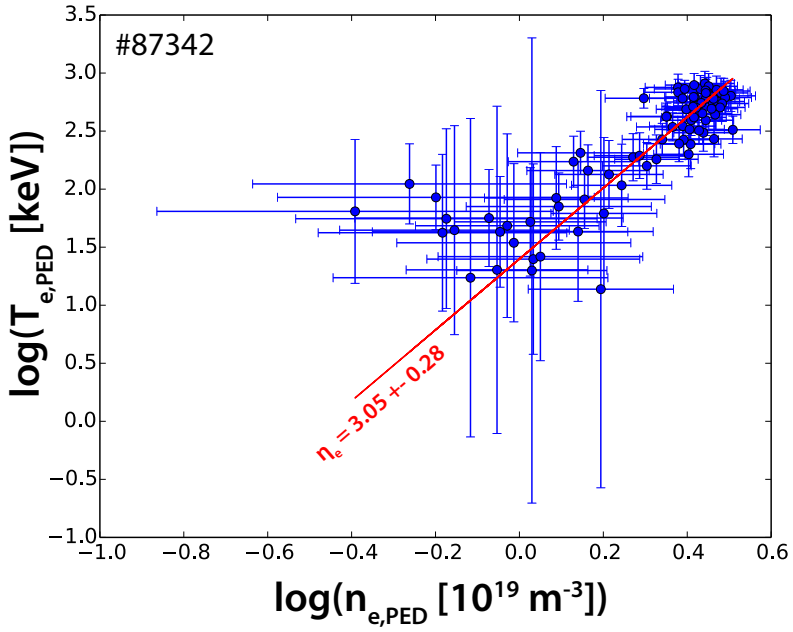

Figure 5.12: The pre-ELM pedestal T_e as a function of n_e directly from the TS data for discharge #87342. In order to estimate η_e, a linear fit to the data was obtained taking into account the uncertainties both in n_e and T_e.

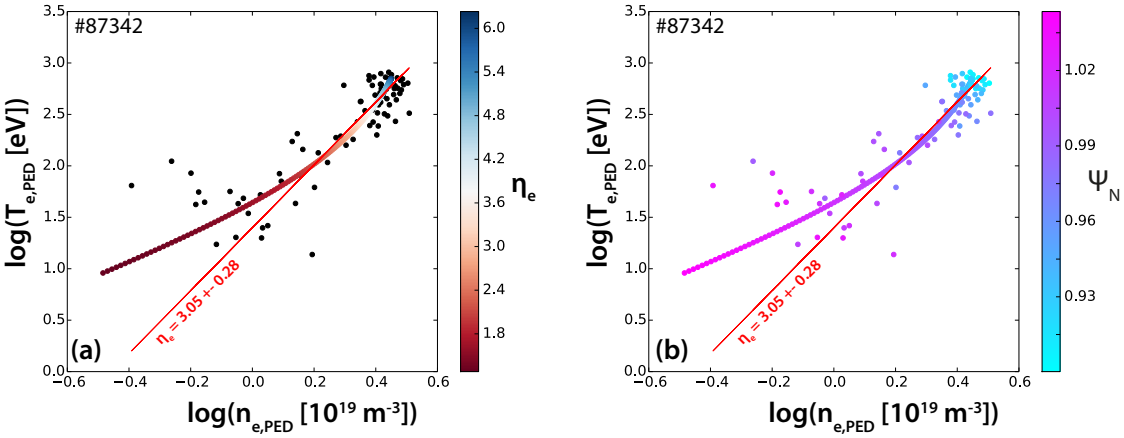

Figure 5.13: Comparison of the two different methods used to estimate η_e in the pedestal for a representative example (discharge #87342). Both figure a and b show the TS data points on a logarithmic scale in black and the linear fit in red. The η_e profile evaluated from the mtanh fits is also shown in these figures in colors. The color scale shows η_e in figure a, and Ψ_N in figure b.

region of interest is extended to 2 times the wdith of the T_e pedestal in order to increase statistics for the fit.

Despite the different approaches, η_e from the two different methods showing qualitatively similar results for the H and D dataset as can be seen in figures 5.14 and 5.15. In the 1.4 MA/1.7 T dataset, there is some separation in η_e for the discharges at different gas rates in D, as shown in figure 5.14a and 5.15a. η_e increases with increasing gas rate for $P_{\text{sep}} > 6$ MW in D, which is consistent with the larger relative radial shift between T_e and n_e pedestals at higher gas rates and power [169–171]. The position of

the n_e pedestal is radially outwards with respect to the T_e pedestal, thus in the region of maximum T_e gradient the density gradient is smaller, leading to higher values of η_e. There is no significant difference between the η_e values of the H and D plasmas (see figure 5.14a). L_{n_e} and L_{T_e} at given P_{sep} are also similar in H and D for this dataset. This suggests that the mechanism identified in [99] and [102] explaining the differences between JET-C and JET-ILW pedestals through differences in η_e does not apply here. Differences in the inter-ELM transport between the H and D pedestals due to other mechanisms are not excluded and future work should focus on studying transport with gyrokinetic simulations in order to identify these. Figure 5.14b shows that at 1.0 MA/1.0 T, η_e is typically larger in H than in D, which is a result of the n_e pedestal being very narrow and shifted radially outwards with respect to the T_e pedestal. Figure 5.15b shows somewhat different behaviour. The very high values of η_e seen in H at the top of the T_e pedestal (see figure 5.14b) are not captured by the linear fit. However, except for the high gas D cases, η_e is typically larger in H than in D at given P_{sep}. Higher η_e in H may imply differences in pedestal heat transport between H and D, although the degradation of the pedestal is the least pronounced in this dataset, thus further transport analysis and comparison with gyrokinetic simulations would be required to clarify the relation between the heat transport and η_e at 1.0 MA/1.0 T.

In summary, the main differences in the pedestal structure between H and D are that the pedestal pressure is typically reduced in H compared to D at the same input power and gas rate, primarily due to lower pedestal density in H. The pedestal electron pressure gradient is typically lower in H than in D at similar pedestal pressure widths. The neutral penetration model is not consistent with differences in the density pedestals between H and D, indicating that transport is likely to play a role in the isotope dependence of the pedestal.

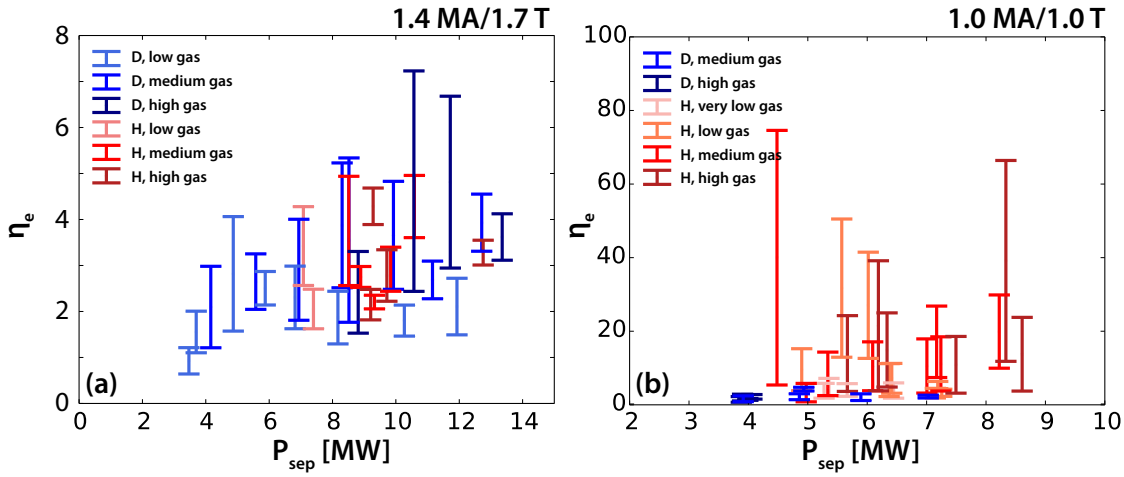

Figure 5.14: $\eta_e = L_{n_e}/L_{T_e}$ is calculated for the pre-ELM pedestals from the mtanh fits. The figure shows the range of η_e between the lowest and highest values in a $0.02\Psi_N$ wide region around the centre of the T_e pedestal for the (a) 1.4 MA/1.7 T and the (b) 1.0 MA/1.0 T datasets.

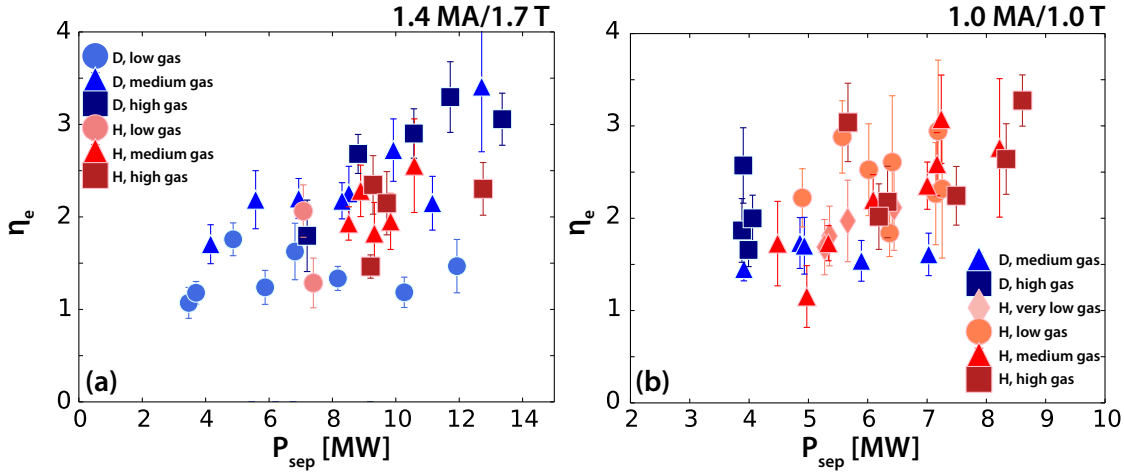

Figure 5.15: η_e as evaluated from the linear fit on $\log(T_e)$ as a function of $\log(n_e)$ directly from the TS data in the pedestal. The figure shows η_e for the (a) 1.4 MA/1.7 T and the (b) 1.0 MA/1.0 T datasets.

Chapter 6

Pedestal transport in JET-ILW H and D type I ELMy H-modes

The previous chapter revealed numerous differences between H and D pedestals in JET-ILW type I ELMy H-modes and indicated that the understanding of pedestal transport is essential to explain the observed favourable isotope dependence of the pedestal. Thus, in the present chapter, pedestal transport is investigated experimentally in detail. Section 6.1 presents a power balance analysis of the pedestal to separate the ELM and inter-ELM losses. Section 6.2 examines the potential role of ELM particle losses in setting the lower density in H. The edge transport and neutral penetration are then investigated using interpretative 2D edge transport simulations with the EDGE2D-EIRENE code. These results are presented in section 6.3.

6.1 Power balance analysis

In this section a power balance analysis is presented to compare JET-ILW H and D type I ELMy H-modes in terms of radiation, ELM losses and inter-ELM transport. P_{sep} in the power balance equation here is separated into inter-ELM and ELM components and $\mathrm{d}W/\mathrm{d}t$ is omitted as only the steady phases of the discharges are examined, where the rate of change of stored energy on time scales longer than the ELM cycle is negligible:

$$P_{\mathrm{sep}} = P_{\mathrm{inter-ELM}} + P_{\mathrm{ELM}} = P_{\mathrm{loss}} - P_{\mathrm{rad,bulk}} \tag{6.1}$$

The ELM energy loss (ΔW_{ELM}) - which gives $P_{\mathrm{ELM}} = \Delta W_{\mathrm{ELM}} \times f_{\mathrm{ELM}}$ - has been evaluated from two independent measurements: a) the stored energy drop from EFIT equilibrium reconstruction (ΔW_{MHD}) and b) Thomson scattering electron kinetic profile

measurements (ΔW_{TS}). ΔW_{MHD} is estimated by the difference between the maximum and the minimum of the W_{MHD} signal in the vicinity of the ELM crash, as illustrated by the red arrow in figure 6.1. ΔW_{MHD} is evaluated for all ELMs individually in the steady phase of the discharge. The ELM energy losses are then averaged and their standard deviation provides a measure for the scatter in ΔW_{MHD}, which will be represented with error bars.

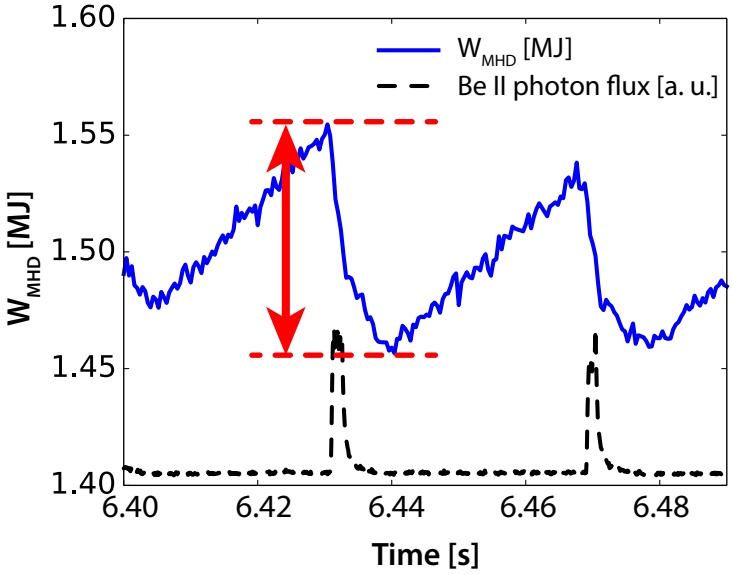

Figure 6.1: Stored energy signal (W_{MHD}) from EFIT equilibrium reconstruction (in blue) during an ELM crash in H pulse #91554. The inner divertor BeII (λ = 527 nm) photon flux (in black) is used as an ELM marker.

ΔW_{TS} is evaluated by applying the method explained in [155]. In the steady phase of the pulse, the pre- and post-ELM TS profiles are fitted using the ELM synchronisation technique to compensate for the low time resolution (20 Hz) of the TS diagnostic. The post-ELM profile fit represents roughly the 5-15 % interval of the ELM period. TS measurements taken during the ELM crash are excluded, as the profiles in this interval are often dominated by the particular dynamics of each ELM crash. Typically 2 or 3 TS measurements following the ELM crash are selected. An example is shown in figure 6.2, where pre-ELM (80-97 %) and post-ELM (5-15 %) electron density (figure 6.2a) and temperature (figure 6.2b) TS profiles can be seen for D discharge #84796. The ELM energy loss is calculated from the difference between the pre- and post-ELM TS profiles volume integrated in the region $\Psi_N = [0.5, 1.05]$. $T_i = T_e$ is assumed and line-averaged Z_{eff} measurements (assuming Be as single impurity) are taken into account to evaluate the total ELM energy loss. Due to ELM synchronisation, ΔW_{TS} is already an average over the steady phase of the discharge. The uncertainty of ΔW_{TS} is estimated from the errors of the pedestal top values of the mtanh fit.

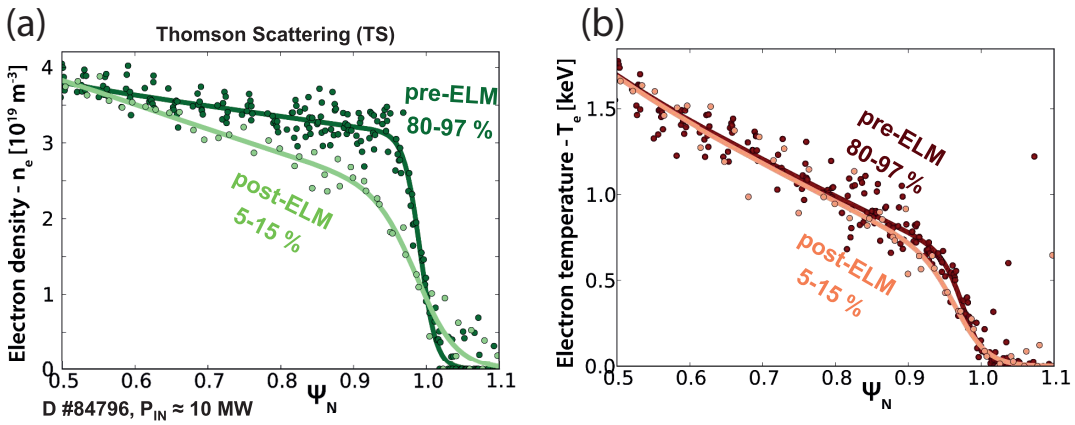

Figure 6.2: The mtanh fitted pre-ELM (80-97 %) and post-ELM (5-15 %) electron density (a) and temperature (b) profiles of D pulse #84796.

A comparison of ELM losses evaluated from ΔW_{MHD} and ΔW_{TS} for selected type I ELMy H-modes of the JET-ILW H and D isotope dataset is shown in figure 6.3. The ELM losses evaluated by the two measurements are broadly consistent, especially in controlled parameter scans, but differences between individual discharges can be as high as a factor of 2 due to the intrinsic uncertainties of this analysis. These include uncertainties in ΔW_{MHD} due to slow data acquisition of the magnetic diagnostics, screening of the vacuum vessel and other conducting structures and uncertainties in ΔW_{TS} due to uncertainties in the TS measurement and errors introduced by ELM-synchronisation and regularisation of the profile by the mtanh fit. Due to these difficulties with the measurements, ELM energy losses can only be evaluated below $f_{\mathrm{ELM}} \approx 50 - 60$ Hz. Thus, figure 6.3 shows a subset of JET-ILW H and D type I ELMy H-modes, where the ELM frequency satisfies this condition. In figure 6.3, ΔW_{TS} is typically lower than ΔW_{MHD}. This may be a consequence of the low time resolution of the TS diagnostic, which results in an underestimate of the ELM losses, as it is difficult to capture the very fast recovery phase of the pedestal in the beginning of the ELM cycle.

The power balance analysis is presented here for selected discharges with plasma current $I_p = 1.4$ MA, toroidal magnetic field $B_t = 1.7$ T, fuelling gas rate $\Gamma_e = 3 - 4 \times 10^{21}$ e/s and NBI heating as reported in table 6.1. The ELM-averaged pedestal kinetic profiles of the selected pulses are shown in figure 6.4. It shows the pedestal profiles of electron density, temperature and pressure for a H reference discharge in red (#91554) and two deuterium plasmas, one with similar thermal stored energy (in blue, #84793) and one with similar input power (in black, #84796) with respect to the hydrogen counterpart. The main parameters of these 3 discharges can be seen in table 6.1.

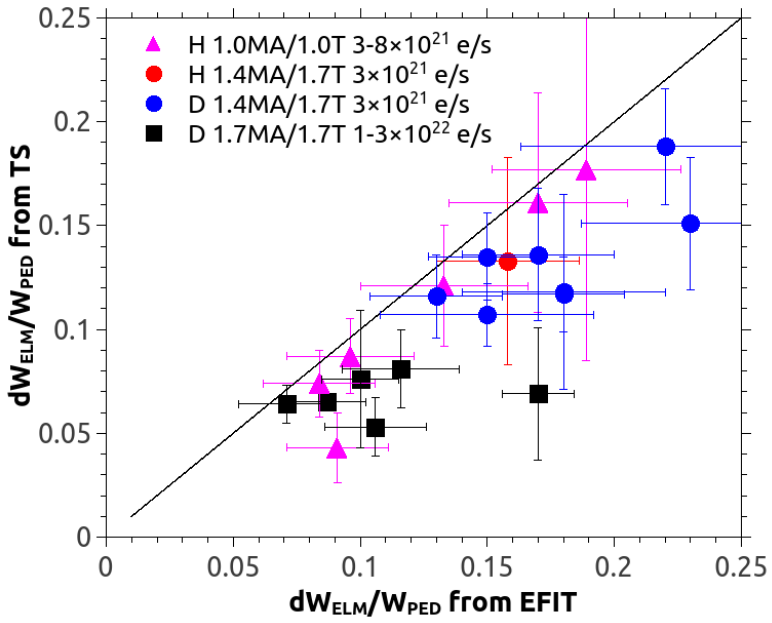

Figure 6.3: Comparison of ELM losses normalised to the pedestal stored energy (W_{PED}) evaluated from W_{MHD} and TS profiles on a subset of JET-ILW H and D type I ELMy H-modes.

Shot	Isotope	I_{p} [MA]	B_{t} [T]	Γ_{D} [10^{21} e/s]	δ	P_{NBI} [MW]	P_{loss} [MW]	W_{th} [MJ]	f_{ELM} [Hz]
#84793	D	1.4	1.7	2.8	0.2	4.4	4.6	1.2	14.2
#84796	D	1.4	1.7	2.8	0.2	10.6	10.4	1.9	18.7
#91554	H	1.4	1.7	4	0.2	10.0	9.4	1.1	31.3

Table 6.1: Main parameters of the H and D plasmas selected for comparison of power balance. P_{NBI} is the NBI heating power, P_{loss} is the loss power (i.e. the total absorbed power compensated with the time derivative of the total stored energy), W_{th} is the thermal stored energy calculated as 2 times the electron stored energy from TS measurements and f_{ELM} is the ELM frequency.

The comparison of H and D type I ELMy H-modes at similar stored energy (#91554 and #84793) shows that roughly two times higher heating power is needed in H to match the stored energy of the D counterpart. In this comparison the pedestal pressure is also similar and the lower density in H is compensated by the higher temperature as shown in figure 6.4. When the heating power is similar in H and D (#91554 and #84796), the pedestal temperature is similar too, but the pedestal density is significantly lower in H.

The result of the power balance analysis for the 3 discharges characterised above is summarised in table 6.2. The comparison of H and D plasmas at similar stored energy (#91554 and #84793) shows that roughly double inter-ELM separatrix loss power is required in H than in D to maintain similar pedestal top pressure. This is in agreement with observations from ASDEX-Upgrade H-mode plasmas [110]. When the heating power

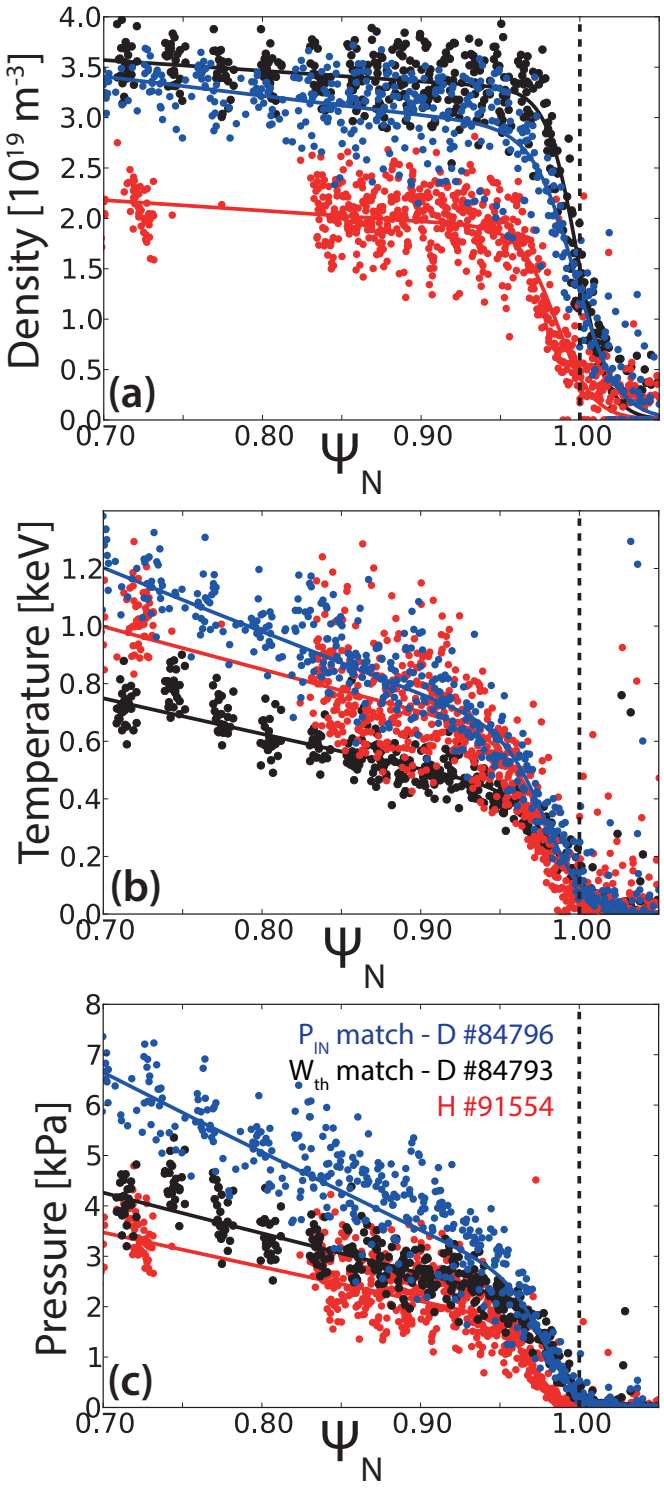

Figure 6.4: ELM-averaged (0-100 % of the ELM cycle) electron kinetic profiles from TS of the pedestal for the hydrogen reference discharge (#91554) and two deuterium plasmas, one with similar thermal stored energy (#84793) and one with similar input power (#84796) with respect to the hydrogen counterpart. (a) Electron density (b) electron temperature (c) electron pressure. These profiles are radially shifted to have $T_{\mathrm{e,sep}} = 100$ eV.

is similar in H and D (#91554 and #84796), the inter-ELM separatrix loss powers are also similar (but $p_{\mathrm{e,PED}}$ is higher in D than in H).

Shot	Isotope	P_{loss} [MW]	P_{rad} [MW]	P_{ELM} [MW]	P_{sep} inter-ELM [MW]	$p_{e,PED}$ [kPa]
#84793	D	4.6	1.1	1.1	2.4	2.2
#84796	D	10.4	2.2	2.4	5.8	3.1
#91554	H	9.4	2.0	2.3	5.1	2.1

Table 6.2: Power balance analysis for the three discharges at 1.4 MA/1.7 T and low gas rate introduced in table 6.1.

6.2 ELM particle losses

It is now analysed how ELMs affect the particle and energy channels. Figure 6.2a and b show the pre-ELM (80-97 %) and post-ELM (5-15 %) TS profiles for D discharge #84796. In this example, the ELMs primarily affect the density, not so much the temperature profiles. This behaviour is general in the analysed dataset and applies to both H and D plasmas as indicated by figure 6.5, where the relative drop of the pedestal top density and temperature is shown for H and D plasmas at 1.4 MA/1.7 T (circles) and 1.0 MA/1.0 T (triangles). A comparison of the fuelling sources in representative plasmas (from EDGE2D-EIRENE simulations, see section 6.3) and an order of magnitude estimate for the ELM particle losses utilising the TS measurement suggests that ELMs could be responsible for $\sim 20-30$ % of the total particle losses. In view of this, ELM particle losses are investigated here in detail.

ELM energy losses primarily due to the loss of particles have also been observed in low triangularity JET-C experiments, where f_{ELM} was increased by increasing the fuelling gas rate [38, 153]. At low f_{ELM}, ELM energy losses (relative to the total stored energy) and the relative temperature drop were high, with smaller relative density drop. With increasing f_{ELM}, the ELM energy losses decreased, primarily due to the reduction of the relative temperature drop and no change in the relative density drop. Hence, the high frequency ELMs mainly affected the density pedestal, similarly to the ELMs observed in the JET-ILW isotope experiments described here.

As it was shown in chapter 5, the pedestal density in D is higher than in H at similar P_{sep} and gas rate in the JET-ILW isotope dataset. However, it has also been shown that the ELM frequency is typically higher in H in these conditions. Figure 6.6a shows the pedestal top density as a function of f_{ELM} in H and D for the low gas 1.4 MA/1.7 T and the medium gas 1.0 MA/1.0 T datasets. In these low triangularity plasmas ($\delta \approx 0.2$), $n_{\text{e,PED}}$ decreases as f_{ELM} is increased by increasing input power at constant gas rate. H and D pedestals at similar f_{ELM} (obtained at different P_{sep}) have comparable pedestal

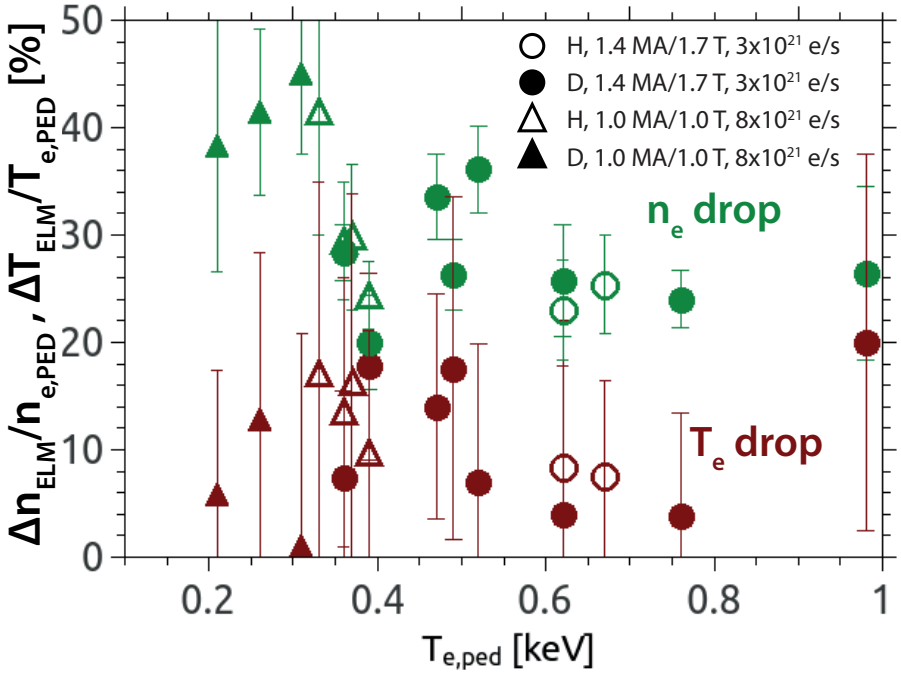

Figure 6.5: The relative drop of the pedestal top density and temperature during ELMs for H (open symbols) and D (full symbols) plasmas at 1.4 MA/1.7 T low gas rate (circles) and 1.0 MA/1.0 T medium gas rate (triangles).

densities, as highlighted by the black dashed circles in figure 6.6a. This suggests that the higher ELM frequency in H may also play a role in setting the observed lower $n_{\mathrm{e,PED}}$.

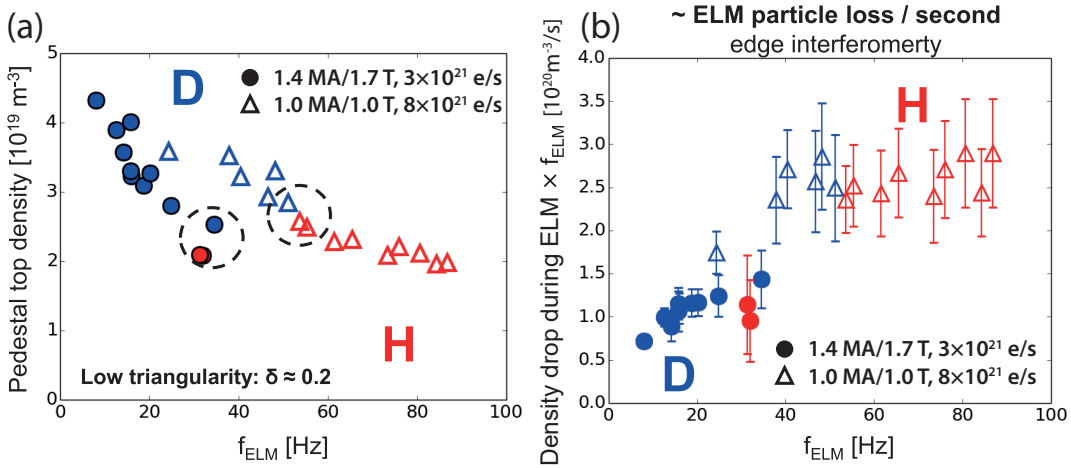

Figure 6.6: (a) Pedestal top density as a function of f_{ELM} in low $\delta(\approx 0.2)$ H and D plasmas at 1.4 MA/1.7 T (full circles) and 1.0 MA/1.0 T (open triangles). H and D pedestals at similar f_{ELM} (but different P_{sep}) have comparable pedestal densities as highlighted by the black dashed circles. (b) Average drop in edge interferometer signal during ELMs per second. D pulses are indicated in blue, H pulses in red. The error bars represent the statistical variation of the ELM particle loss throughout the steady phase of the discharge.

The increase in "density pump out" with increasing f_{ELM} has been observed in JET experiments utilising ELM pacing via fast vertical plasma motion (vertical kick) [179].

Vertical kicks trigger ELMs by introducing a local perturbation of the current density close to the separatrix. A kick is an intermittent perturbation and only affects the transport by triggering extra ELMs but not modifying the inter-ELM transport [179]. It has been reported that the correlation between the density pump-out and f_{ELM} suggests that the reduction in the plasma particle content is a consequence of the increase in the time averaged ELM particle loss [179].

In order to understand the cause of the correlation between f_{ELM} and $n_{\mathrm{e,PED}}$ in the H and D isotope database, the ELM particle losses are investigated. High time resolution density profile measurements were not available for the plasmas in the analysed dataset. The TS system has slow time resolution (20 Hz) and the reflectometry is not available on JET below $B_t = 2$ T. Therefore, an edge interferometer LOS with submillisecond time resolution was utilised to estimate the particle loss in an ELM crash. The drop in the line-averaged interferometer signal during the ELM crash multiplied by the ELM frequency is taken as proxy for the total ELM induced particle loss, $f_{\mathrm{ELM}} \times \Delta n_{\mathrm{ELM}}$, where Δn_{ELM} is the particle loss caused by the ELM.

Figure 6.6b shows that at low f_{ELM} (< 40 Hz) ELM particle losses increase with ELM frequency. This implies that the higher f_{ELM} in H than in D at similar P_{sep} and gas rate may contribute to the observed lower pedestal density in H. However, ELM particle losses saturate at higher f_{ELM}, both in H and in D, indicating that other mechanisms may also play a role in setting lower density in H. EDGE2D-EIRENE simulations discussed in the next section indicate that higher particle transport (ELM and inter ELM particle transport together in these simulations) in H than in D is likely to play an important role in the observed lower pedestal density in H.

6.3 Interpretative EDGE2D-EIRENE simulations

In order to support the experimental analysis on the H and D pedestals presented in this thesis, interpretative 2D edge transport simulations were also carried out. These simulations help to understand how transport and neutral penetration affect the pedestal performance when the isotope mass is changed. Furthermore, an important boundary condition, namely the electron temperature at the separatrix, can also be tested with such simulations. As it will be shown in chapter 7, the value of the separatrix temperature affects the MHD stability of the pedestal. The edge transport code utilised for the simulations described here is EDGE2D-EIRENE [180–182].

6.3.1 EDGE2D-EIRENE

EDGE2D solves the multi-fluid equations in a two-dimensional, realistic divertor geometry. Due to the relatively cold temperature in the edge region of the plasma, the presence of neutral atoms and molecules are important and their interaction with the plasma needs to be taken into account for accurate treatment of the sources due to atomic physics effects such as radiation, ionisation, charge exchange, etc. As the density of neutrals is relatively low, neutral-neutral collisions can be neglected and the neutrals can be tracked with the Monte Carlo transport code, EIRENE [180, 182].

The fluid equations for species s solved by EDGE2D are the following:

$$\frac{\partial n_s}{\partial t} + \nabla \cdot (n_s \mathbf{v_s}) = S^{\text{neut}}_{s,\text{part}} \ , \tag{6.2}$$

$$\frac{\partial (\rho_s \mathbf{v_s})}{\partial t} + \Big(\nabla \cdot (\rho_s \mathbf{v_s} \mathbf{v_s} + \boldsymbol{\pi_s}) + \nabla p_s \Big) = e_s n_s (\mathbf{E} + \mathbf{v_s} \times \mathbf{B}) + \sum_{s \neq s'} \mathbf{R_{ss'}} + S^{\text{neut}}_{s,\text{mom}} \ , \tag{6.3}$$

$$\frac{\partial}{\partial t} \left(\frac{3}{2} p_s \right) + \frac{5}{2} p_s \nabla \cdot \mathbf{v_s} + \nabla \cdot \mathbf{q_s} = \sum_{s \neq s'} \mathbf{W_{ss'}} + \mathbf{v_s} \nabla p_s + S^{\text{neut}}_{s,\text{en}} + S^{\text{rad}}_{e,\text{en}} \ . \tag{6.4}$$

Eq. (6.2) is the particle conservation equation, which shows that the number of particles in a differential volume are changed by the sources (or sinks) and the particle flux out of the volume. Eq. (6.3) is the momentum conservation equation. On the left hand side of eq. (6.3) the first term is the rate of change of the momentum and the second term is the momentum flow out of the differential volume with $\boldsymbol{\pi_s}$ the viscosity tensor. On the right hand side of eq. (6.3) the first term is the Lorentz force, the second term is the collisional friction between the different species and momentum source as a result of interactions with neutrals is represented by the third term. Eq. (6.4) represents the conservation of the internal energy in the rest frame of species s. On the left hand side of eq. (6.4) the first term is the rate of change of the internal energy density (i.e. the pressure p_s). The second term is the work done in compressing the fluid and the third term represents the heat flowing out the differential volume with $\mathbf{q_s}$ the heat flux. The first term on the right hand side of eq. (6.4) is the energy gain due to collisions with other species, the second term is the convection of the pressure gradient, the third term is the energy loss due to interactions with neutrals and the fourth term is the energy loss due to radiation which only applies to the electrons. Viscosity is neglected in the energy conservation equation in EDGE2D.

Eqs. (6.2)-(6.4) are solved in EDGE2D for the electrons, bulk ions and impurity ions. Assuming axisymmetry, the equations are written in a curvilinear coordinate system

representing the poloidal plane. The coordinate system relies on the EFIT equilibrium reconstruction for the plasma being simulated and the simulation cells are aligned with the magnetic flux surfaces. The parallel transport is calculated using the so-called "21 moment" description [183], which is an extension of the Braginskii equations [184] and is valid for arbitrary impurity concentrations. In the perpendicular direction the transport is simulated as a diffusive process and the perpendicular heat and particle transport coefficients are user defined. These perpendicular transport coefficients are usually set in a way that the upstream profiles for density and temperature match with those measured in the plasma being modelled. At the sheath region in front of the divertor targets the Bohm criterion is applied, which assumes that ions enter the sheath with a parallel velocity equal to, or greater than the sound speed. In the simulations presented in this thesis, it is assumed that this criterion is marginally satisfied, i.e. the ion parallel velocity is equal to the sound speed. The neutral source terms are treated by EIRENE, which is a Monte-Carlo kinetic neutral code. The atomic and molecular processes considered in the default version of EDGE2D-EIRENE are ionisation, charge exchange, radiative recombination, 3-body recombination and dissociative recombination, dissociative excitation and dissociative ionisation. For impurity ions, only ionisation and recombination processes are considered.

6.3.2 Edge plasma properties in H and D type I ELMy H-modes

In this thesis, EDGE2D-EIRENE is used in an interpretative way to investigate the edge properties of H and D type I ELMy H-modes. A pair of type I ELMy H-modes at low gas rate (#91554 and #84793) with similar stored energy were selected (see table 6.1). Note that the input power is doubled in H compared to D to reach similar stored energy and pedestal pressure, and the H pulse has lower $n_{\mathrm{e,PED}}$ and higher $T_{\mathrm{e,PED}}$ than the D pulse (see figure 6.4). In these interpretative runs the perpendicular transport coefficient of electron particle diffusion $D_\perp$ ($\Gamma_e = D_\perp \nabla n_e$), electron and ion heat transport $\chi_{e,i}$ ($q_{e,i} = -n_{e,i}\chi_{e,i}\nabla T_{e,i}$) and the pump albedo were iterated until the solution fitted the upstream n_e and T_e profiles (measured by TS) and the outer target heat deposition profile (measured by IR-camera). χ_e and χ_i were assumed to be the same. χ in the SOL was set such that the heat deposition profile at the outer divertor target matched the IR camera measurements. The aim here was to approximately match the width of the heat deposition profile in order to constrain the width of the SOL, which potentially affects $T_{e,sep}$. Cross-field drifts were not taken into account in the simulations.

The grid for EDGE2D relies on EFIT equilibrium reconstruction and is shown in cyan in figure 6.7a. The EDGE2D simulation domain extends to $\sim 10-15$ cm inside the separatrix to the core plasma. The input power in EDGE2D was set to the power crossing the separatrix inter-ELM, i.e. the ELM power loss (P_{ELM}) was excluded. The ELM crash was not simulated and it was assumed that P_{ELM} does not contribute to the power balance in the SOL, which sets the separatrix temperature inter-ELM. For simplicity, both the H (#91554) and the D (#84793) case were simulated in the corner-corner (C/C) divertor target configuration, albeit discharge #84793 was in vertical-horizontal (V/H) divertor target configuration in the experiment. For the C/C configuration, the wall structure of the grid had to be slightly modified around the outer strike-point so that the EDGE2D grid does not cross wall surfaces, as shown in figure 6.7b. In this way, the real JET divertor geometry (in green) is slightly altered to be aligned with the outermost grid elements. This modification could possibly lead to some differences in the neutral pressure around the outer strike point compared to that in the real geometry, but the aim here was to compare a pair of H and D simulations and not to carry out comprehensive validation of the code. Thus, both the H and the D cases were simulated using the same grid. A quantitative answer on how much the wall structure alteration used here affects the simulated target and upstream profiles could only be given by testing this effect with an edge transport code such as SolEdge2D [185, 186] that is capable of handling complex geometries, but this is out of the scope of the present work.

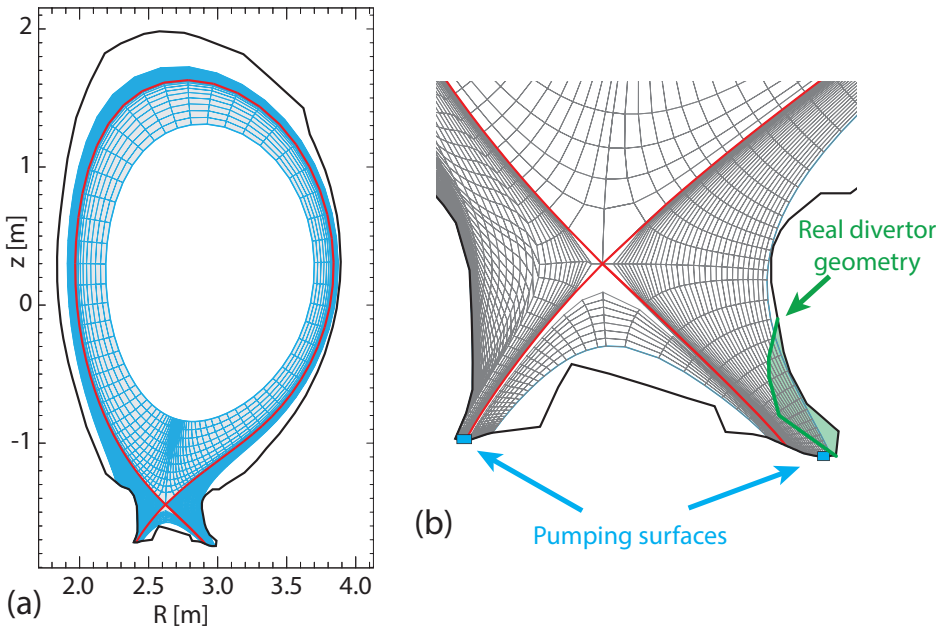

Figure 6.7: (a) The EDGE2D simulation grid in cyan. (b) The real divertor geometry (in green) is slightly altered at the outer strike point to be aligned with the outermost grid elements. The pump surfaces are shown in cyan close to the strike points.

As explained in chapter 5, divertor cryopumping is more effective in the C/C configuration, thus the pump albedo is likely to be overestimated in our EDGE2D-EIRENE simulations for the D case (which is in V/H configuration in the experiment). The gas fuelling was set in accordance with the experiment. The impact of divertor configuration (C/C vs V/H) on the pedestal density has been investigated in a separate study, where all input parameters of the interpretative simulation for #84793 (transport coefficients, pump albedo, input power, gas fuelling, etc.) were kept fixed, but the divertor configuration was changed from C/C to V/H. The pedestal density increased by approximately 15-20 %, while $T_{\mathrm{e,PED}}$ decreased leading to virtually no change in pedestal pressure, which is consistent with the experimental observations [53].

Figure 6.8 shows the "inter-ELM" (40-80 % of the ELM cycle) n_e and T_e profiles measured by TS (in grey) and the profiles of the EDGE2D-EIRENE solutions (in red for H and blue for D). The "inter-ELM" outer target heat flux profiles are evaluated by averaging the profiles from the IR camera in the 40-80 % part of the ELM cycle and are compared with the EDGE2D simulations in figure 6.9. The time evolution of heat deposition reconstructed from IR measurements can be very uncertain in the vicinity of the ELM crash due to the transient heat flux arriving to the target. Thus, the 40-80 % interval was chosen to represent the inter-ELM parameters and exclude any artefacts in the heat deposition profiles. TS data are also filtered for the 40-80 % part of the ELM cycle for consistency. The implications on the separatrix temperatures indicated in figure 6.8 will be discussed in section 6.3.3.

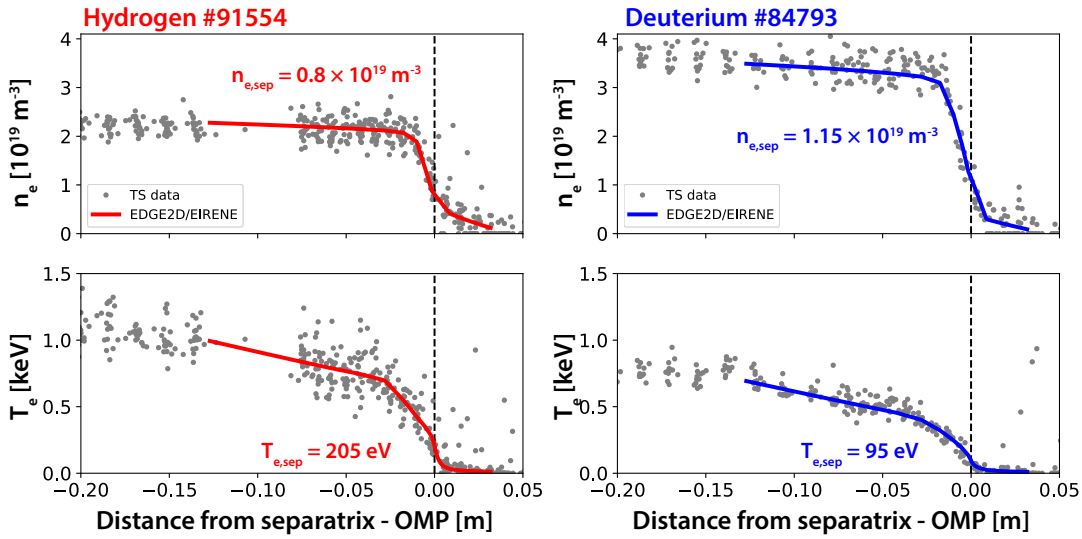

Figure 6.8: Inter-ELM TS profiles (40-80 % of the ELM cycle) for n_e and T_e (in grey) in the steady phase of the H (#91554: 5.7-8.2 s) and D (#84793: 5.0-6.3 s) discharges. The resulting upstream n_e and T_e profiles of the interpretative EDGE2D-EIRENE simulations for the H pulse (#91554) in red and for the D pulse (#84793) in blue.

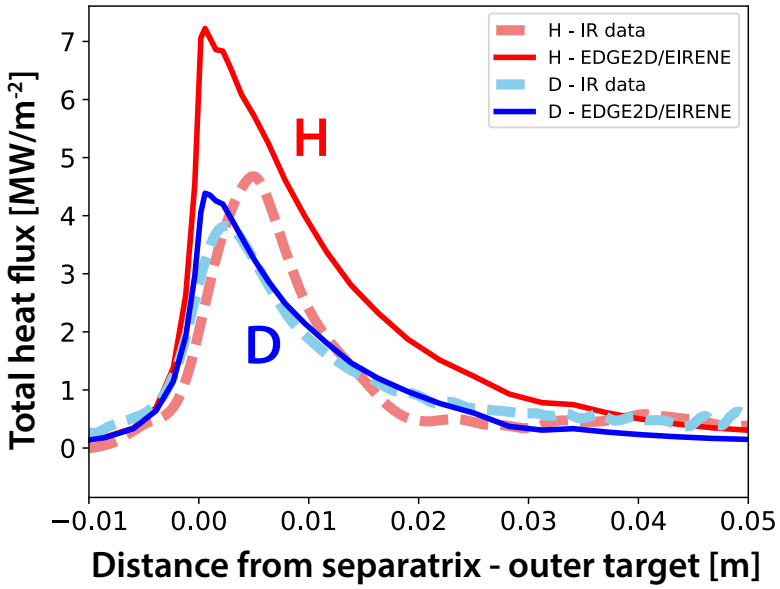

Figure 6.9: Inter-ELM (40-80 % of the ELM cycle) outer target heat deposition profiles as evaluated from IR camera measurements in the steady phase of the H (#91554: 5.7-8.2 s) and D (#84793: 5.0-6.3 s) discharges with dashed lines. Outer divertor target heat deposition profiles from EDGE2D-EIRENE with solid lines for H (red #91554) and D (blue #84793).

In the simulations, the pumping surfaces were placed at the corners of the simulated divertor (see figure 6.7b), where - in experiment - neutrals would be moving into the sub-divertor region by the action of the cryopump. The pump efficiency is defined by the pump albedo, which gives the probability that a neutral - which reaches the pumping surface - is reflected. The pump albedo was set to 0.4 for H and to 0.7 for D to obtain a match of the upstream profiles for these two discharges. However, these values are not consistent with testbed results on the sticking coefficients (α_s) of H_2 and D_2 at a cryopump surface [187, 188]. The sticking coefficient is the ratio of the number of particles sticking to the cryosurface related to the total number of particles impinging on it. The sub-divertor structures and the cryopump are not modelled in these EIRENE simulations, thus a one-to-one comparison between the albedo defined in EDGE2D-EIRENE and the testbed results for the sticking coefficients on a cryosurface is not possible, but the albedo is roughly proportional to $(1 - \alpha_s)$. The testbed results show that the sticking coefficient is higher in D than in H [187, 188], implying lower albedo in D than in H in contrast to the EDGE2D-EIRENE pump albedo settings. A possible reason for this disagreement could be that the much hotter ions, electrons and neutrals in the SOL of the H discharge may have resulted in different neutral recycling at the wall.

Figure 6.10 shows the anomalous transport coefficients used in the simulations to match the experimental upstream and divertor target profiles. The anomalous heat transport coefficients inside of the pedestal are higher in H than in D, but are comparable

in the edge transport barrier (ETB). $D_\perp$ is higher in H than in D everywhere inside the separatrix. This implies that larger particle transport in H than in D could be responsible for the different pedestals, which is consistent with the experimental observations suggesting higher ELM particle losses in H than in D as discussed in section 6.2. Note that in the EDGE2D-EIRENE simulations, $D_\perp$ represents the total particle transport, which - in the experiment - is a sum of the ELM and the inter-ELM particle losses. The "steps" in $D_\perp$ and $\chi_{e,i}$ in the ETB (see figure 6.10) were needed in EDGE2D-EIRENE to match the TS data as closely as possible, but it is important to note that $T_{\mathrm{e,sep}}$ is not sensitive to these fine details in the shape of the perpendicular transport coefficients. $\chi_{e,i}$ outside the separatrix is constrained by the outer target IR heat deposition profile, but there is insufficient information from IR to distinguish between H and D. Similarly, there is no available TS density data outside the separatrix to constrain $D_\perp$, which was therefore imposed to be the same in H and D. It is important to note that an edge particle pinch, which may have an important role in the particle transport [189–191] is not introduced in these EDGE2D-EIRENE simulations. The experimental n_e profile shape could be reproduced with different variations of the diffusion coefficient and the pinch velocity, due to the lack of additional constraints. The particle pinch is not taken into account in these EDGE2D-EIRENE simulations, although its role in edge particle transport is not excluded and is the subject of ongoing research.

The effect of change in mean free path of neutrals between H and D in the EDGE2D-EIRENE simulations is investigated with a test where all input parameters (transport coefficients, pump albedo, input power, gas fuelling, etc.) are kept fixed, but only the isotope mass is changed from D to H. The input parameters of the interpretative simulation for the D case (#84793) were taken. The results of the change from D to H for otherwise fixed conditions is only a ~ 10 % increase in the pedestal top density and a slight decrease in the temperature, as shown in figure 6.11. The change in the upstream profiles is small and opposite to experimental observations (see figure 6.4). This result - together with the previous findings that higher transport coefficients are required in H (#91554) than in D (#84793) to match the experimental profiles - indicate that the change in neutral penetration due to different isotope mass does not explain the observed lower density in H pedestals and therefore transport must also play a role.

6.3.3 Separatrix temperature in H and D type I ELMy H-modes

The EDGE2D-EIRENE simulations yield a more accurate value for the electron separatrix temperature than the typically used $T_{\mathrm{e,sep}} \approx 100$ eV for JET H-modes obtained

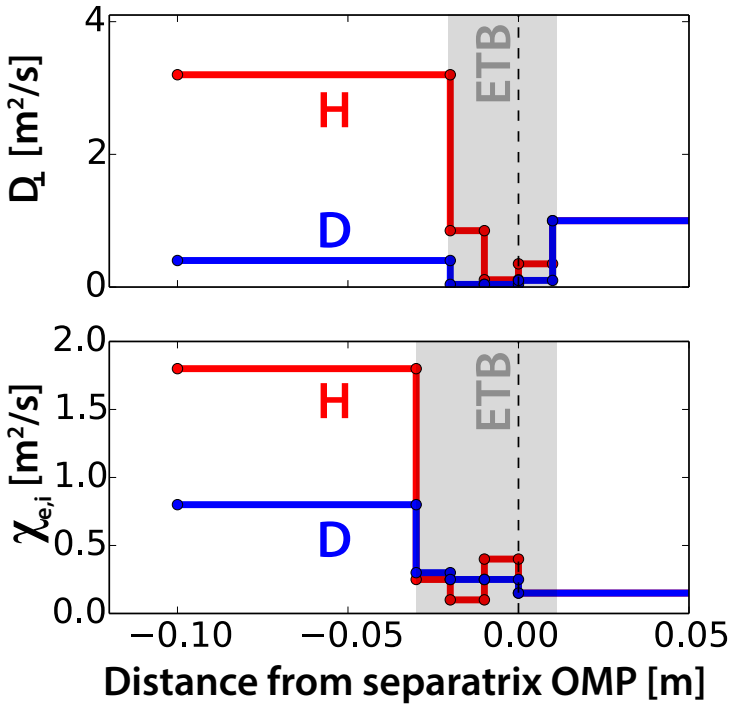

Figure 6.10: Electron particle diffusion ($D_\perp$) and electron and ion heat transport ($\chi_e = \chi_i = \chi_{e,i}$) coefficients of the EDGE2D-EIRENE simulations for the inter-ELM phase (40-80 %) of the H (red #91554) and D (blue #84793) discharges. The edge transport barrier (ETB) is indicated by the grey shaded area.

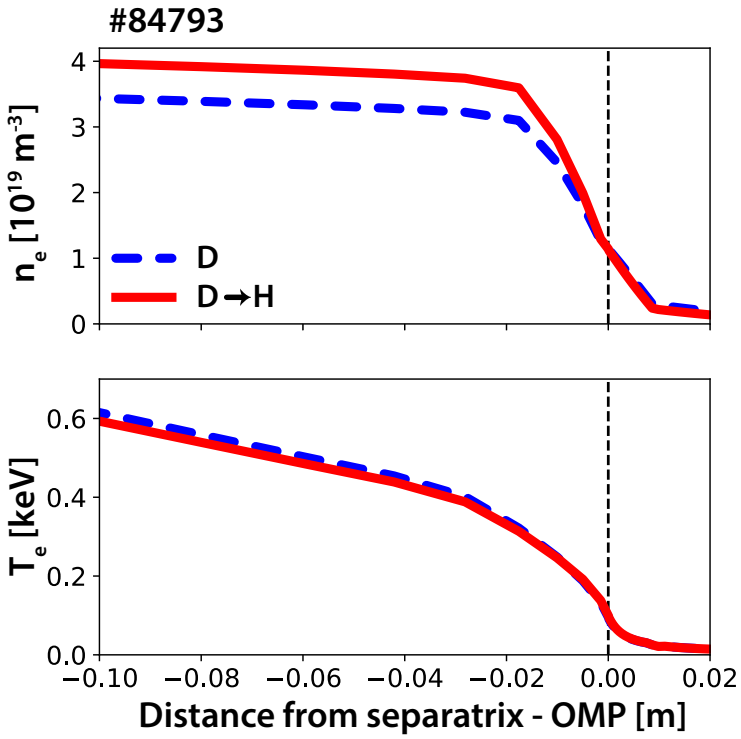

Figure 6.11: Upstream n_e and T_e profiles of a pair EDGE2D-EIRENE simulations where all parameters were kept fixed (transport coefficients, pump albedo, input power, gas fuelling, etc.), but the isotope was changed from D to H.

by the 2-point model [192, 193]. $T_{e,sep}$ is required to constrain the separatrix position for the radial alignment of the measured kinetic profiles. The position of the separatrix from EFIT is uncertain and typically implies unphysical separatrix temperatures ($\ll 100$ eV) due to the uncertainties in the magnetic equilibrium reconstruction. An estimate for $T_{e,sep}$ can be obtained by taking into account the parallel heat conduction and pressure and power balance in the scrape-off-layer (SOL), thus obtaining a relation between the upstream ($T_{e,\text{upstream}} \equiv T_{e,sep}$) and divertor target temperatures ($T_{e,\text{target}}$). Assuming a conduction limited divertor regime, the upstream temperature at the separatrix can be approximated by the two point model equation [193]:

$$T_{e,\text{upstream}} = \left(T_{e,\text{target}}^{7/2} + \frac{7 P_{sep} L}{2 A_q \kappa} \right)^{\frac{2}{7}}, \tag{6.5}$$

where L is the connection length, A_q is the projection of the wetted area perpendicular to the heat flux and κ is the parallel heat conductivity coefficient. $T_{e,\text{target}}$ is often neglected as $T_{e,\text{upstream}}^{7/2} \gg T_{e,\text{target}}^{7/2}$ is satisfied in a conduction limited divertor regime. It is common practice to assume that in eq. (6.5) P_{sep} is the only significantly varying parameter and thus $T_{e,\text{upstream}}$ weakly varies with power ($T_{e,\text{upstream}} \sim P_{sep}^{2/7}$), and approximately equals 100 eV for JET H-modes. However, A_q could also change from discharge to discharge and the condition of the conduction limited divertor regime is not necessarily satisfied in all cases. In the sheath limited regime, the value of $T_{e,\text{target}}^{7/2}$ cannot be neglected. Thus, in realistic experimental conditions, $T_{\text{e,sep}}$ could vary from ≈ 100 eV and in extreme cases it might have a significant effect on pedestal stability [194, 195], as it will be discussed in section 7.3.

As highlighted in figure 6.8, the EDGE2D-EIRENE simulations indicate that $T_{\text{e,sep}}$ is higher in the H discharge (≈ 205 eV) than in the D pulse (≈ 95 eV). This difference is due to the fact that roughly two times more power crosses the separatrix at lower density in the H case. As a result, the H discharge in the EDGE2D-EIRENE simulation is found to be in the sheath limited regime with $T_{\text{e,upstream}} \approx 205$ eV and $T_{\text{e,target}} \approx 200$ eV. In contrast, for the D case $T_{\text{e,upstream}} \approx 95$ eV and $T_{\text{e,target}} \approx 75$ eV. These are still high temperatures at the divertor target, but the temperature drop between upstream and target is larger in the D case than in H. This suggests that the D discharge is closer to the conduction limited regime, while the H discharge is in the sheath limited regime.

The outer divertor target T_e obtained in the EDGE2D-EIRENE simulation for the D case is supported by Langmuir probe measurements, as shown in figure 6.12. Note that these high $T_{\text{e,target}}$ values are not typical of JET-ILW operation but of the low

gas fuelling of this discharge. In the H pulse (#91554), due to lack of Langmuir probe measurements, the high $T_{\mathrm{e,target}}$ suggested by the EDGE2D-EIRENE simulation cannot be compared with experiment. Note that at such high divertor target temperature, above 100 eV as indicated by EDGE2D-EIRENE simulations in H, secondary electron emission could also be important. Secondary electrons are emitted due to high energy plasma particles striking the solid surface. This effect, which would act as an extra electron heat sink in the SOL, is not included in the EDGE2D model. Thus, the high $T_{\mathrm{e,sep}} = 205$ eV obtained for the H discharge should only be taken as an upper limit and must not be considered at face value.

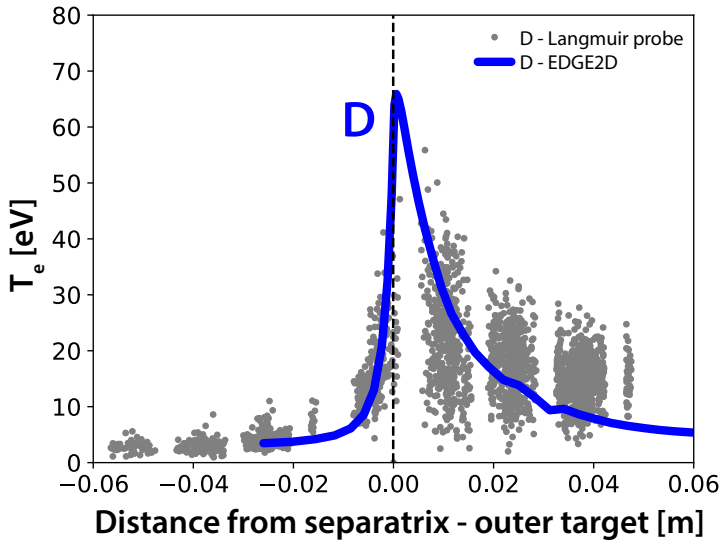

Figure 6.12: Inter-ELM (40-80 %) outer target T_e profile as evaluated from Langmuir probe measurements for the steady phase of the D pulse #84793 (5.0-6.3 s) in grey and T_e from EDGE2D-EIRENE in blue.

The interpretative EDGE2D-EIRENE simulations indicate that $T_{\mathrm{e,sep}}$ is mostly affected by the input power and $\chi_{e,i}$ values in the SOL, which are constrained by the outer target heat flux profile from IR. When both the upstream kinetic profile and outer target heat flux constraints are given, $T_{\mathrm{e,sep}}$ is a robust parameter in the simulation and is not sensitive to the $D_\perp$ and $\chi_{e,i}$ profiles inside the separatrix. The higher power and lower density in the H discharge compared to the D discharge result in a sheath limited divertor regime in the H case, which leads to high electron temperatures both upstream and at the target. The simulation result suggests higher $T_{\mathrm{e,sep}}$ in H than in D, while $T_{\mathrm{e,sep}}(D) \approx 100$ eV as originally assumed using the 2-point model. This difference in divertor regime between the two discharges is a consequence of the density and input power difference in the H and D pair and not to the isotope mass alone. Due to the limitations of the EDGE2D-EIRENE model as discussed above, the $T_{\mathrm{e,sep}}$ value quoted

in figure 6.8, must not be regarded as the exact solution for the H case, but as an indication that $T_{e,sep}$ could be larger than 100 eV in the H pulse. Note that the selected pair of discharges are representative of the divertor conditions of JET-ILW at low gas fuelling rates. It is expected that at higher gas rate (and density) the divertor regime shifts towards conduction limited regime also in H, where lower target and upstream temperatures are expected than those obtained in the EDGE2D-EIRENE simulations for the H discharge at low gas rate (#91554).

The effect of a possible higher separatrix temperature in H on pedestal stability is discussed in the next chapter. The main conclusion of this modelling exercise is that the experimentally observed lower pressure and density pedestal in H compared to D cannot be explained by the changes in neutral penetration. In order to match the experimental pedestal profiles, higher perpendicular transport coefficients need to be set for the H pulse compared to D in EDGE2D-EIRENE, indicating that pedestal transport must play a role in setting the different pedestals when the isotope mass is changed. This is consistent with the conclusions of the experimental analysis, which showed that the density pedestals of the investigated plasmas are not consistent with the neutral penetration model (section 5.4), higher inter-ELM P_{sep} is needed in H compared to D to maintain similar pedestal pressure (section 6.1) and ELM particle losses may be higher in H than in D due to higher ELM frequency at similar input power and gas rate (section 6.2).

Chapter 7

Pedestal stability of JET-ILW Hydrogen type I ELMy H-modes

After discussing the potential isotope dependence of pedestal transport and neutral penetration, in this chapter the pedestal MHD stability is investigated. Modification of the bootstrap current due to finite orbit width effect, when the isotope mass is changed, could potentially affect pedestal stability. This is discussed in section 7.1. It is followed by the analysis of linear MHD pedestal stability in view of the isotope dependence, when diamagnetic stabilisation is taken into account. Finally, a sensitivity of pedestal stability on the separatrix electron temperature, motivated by the results of the EDGE2D-EIRENE simulations, is discussed in section 7.3.

7.1 Isotope dependence of the bootstrap current

As the current density at the edge is typically dominated by the bootstrap current in H-mode plasmas, any isotope dependence of j_{BS} could potentially affect the MHD stability of the pedestal. An isotope dependence of the bootstrap current is only expected if the ion orbit width is comparable to the density and temperature gradient scale lengths.

In the local limit, the bootstrap current does not depend on the ion mass. In order to understand this, the explanation of the source of j_{BS} presented in section 2.1. needs to be elaborated here. As discussed, in the presence of a density gradient, the difference in the number of particles populating the banana orbits in different radial positions leads to a net toroidal current, the banana current. The banana current (j_b) can be estimated by the number of particles going in the direction of the current (δn_b) times their average parallel velocity ($v_{\|}$) [68]. δn_b is roughly the banana orbit width (w_b) times the density gradient. w_b is proportional to the Larmor radius (r_L), which scales as $r_L \sim \sqrt{m}$. At a

given temperature the $1/\sqrt{m}$ scaling of $v_{\|}$ cancels out the $\sqrt{m}$ scaling of δn_b, leading to no ion mass dependence of the banana current.

However, the bootstrap current is mostly carried by the passing particles due to collisional coupling of trapped and passing particles. Thus, the current is arising from the difference in velocity between the passing ions and the passing electrons. The momentum exchange between the passing ions and electrons is proportional to the electron-ion collision frequency and the bootstrap current ($\nu_{ei} j_{\mathrm{BS}}$) [7]. For the passing electrons this is balanced by the momentum exchange between the passing and trapped electrons, which is proportional to the electron-electron collision frequency and the banana current ($\nu_{ee} j_b$) [7]. Equating the two expressions for the momentum exchange for the passing electrons shows that the relation between j_{BS} and j_b is proportional to ν_{ee}/ν_{ei}. The ratio of the e-e and e-i collision frequencies is independent of the ion mass [64]:

$$\nu_{ee} = \frac{\ln \Lambda_e e^4 n_e}{12\sqrt{2}\pi^{3/2}\epsilon_0^2 m_e^{1/2} T^{3/2}} \ , \tag{7.1}$$

$$\nu_{ei} = \frac{\ln \Lambda_e e^4 n_e}{6\sqrt{2}\pi^{3/2}\epsilon_0^2 m_e^{1/2} T^{3/2}} \ , \tag{7.2}$$

where $\ln \Lambda_e$ is the Coloumb logarithm. Consistently, j_{BS} evaluated with local neoclassical transport solvers such as NEO has no isotope dependence.

The isotope mass could play a role in the bootstrap current when finite orbit width effects are important. When the ion orbit width is comparable to the density and temperature gradient lengths, the small orbit width approximation used by local neoclassical codes breaks down. In this section the finite orbit width effect of the bootstrap current is discussed based on Hager's work [168]. Given that the bootstrap current is mostly carried by the electrons (in the laboratory frame) and the electron orbit width is typically much smaller than the kinetic profile gradient lengths, one may think that finite orbit-width effects of j_{BS} are negligible. However, finite orbit-width effects do play a role by entering the electron flow indirectly through the radial electric field (E_r). E_r emerges to keep the plasma quasi-neutral in the presence of the ion orbit motion. E_r drives a parallel flow in the same way as ∇p does. As E_r is in the same direction as ∇p, E_r counteracts the ion bootstrap current, but adds to the electron bootstrap current due to the sign change in the radial electric field force. In other words, E_r transfers the ion bootstrap current to the electrons. The finite orbit width effect influences the bootstrap current in the non-local regime, because the orbit averaged electric fields experienced by ions and electrons differ.

An attempt to quantify the finite orbit width effect on the bootstrap current is presented here, using the analytical formula reported in Hager's work [168]. It is important to note that some low collisionality JET-ILW pedestals may fall outside the validity domain of Hager's formula, as it will be shown later in this section. Hager's formula improves on Sauter's formula by eliminating the inaccuracies explained in section 4.2 and it also includes corrections for finite orbit width effects. The formula is an analytic fit on the results of numerous gyrokinetic simulations with the XGCa code using various magnetic equilibria and plasma kinetic profiles. XGCa is a non-local, gyrokinetic neoclassical code, which uses a fully non-linear Fokker-Planck collision operator with highly accurate conservation of energy, momentum, and mass. The improved formula takes the following form [168]:

$$j_{\mathrm{BS}} = -(\beta_{\mathrm{col}} + \beta_{\nabla T_i})\frac{Ip_e}{B_0}\Bigg(\gamma_{31}L_{31}\frac{1}{p_e}\frac{\mathrm{d}P}{\mathrm{d}\Psi} + \frac{\gamma_{32}L_{32}}{T_e}\frac{\mathrm{d}T_e}{\mathrm{d}\Psi} + \\ +(\gamma_{34}L_{34})(\gamma_\alpha\alpha_i)\frac{1}{ZT_e}\times\Bigg(1 - 2\Delta_\Psi\Big(-\frac{3}{2}L_{T_i}^{-1} + L_n^{-1} + L_q^{-1}\Big)\Bigg)\frac{\mathrm{d}T_i}{\mathrm{d}\Psi}\Bigg)\,, \tag{7.3}$$

which is similar to Sauter's formula shown in eq. (4.3). The definitions of the parameters in eq. (7.3) can be found in [168]. Here the focus is on $\beta_{\nabla T_i}$, which is a correction term to take into account the finite orbit width effects:

$$\beta_{\nabla T_i} = -\frac{\Lambda_1\nu_i^*}{1 + \Lambda_2\nu_i^{*2} + \Lambda_3\nu_i^{*4}}(1-\epsilon)^{\Lambda_4}|\Delta_R|^{\Lambda_5}\frac{\Delta_\Psi}{T_i}\left|\frac{\mathrm{d}T_i}{\mathrm{d}\Psi}\right|\,, \tag{7.4}$$

where Δ_R is the Shafranov shift, Δ_Ψ is the half of the ion orbit width [1] in units of poloidal flux, ν^* is the collisionality and Λ_n $(n = 1, 2, 3, 4, 5)$ are the numerical parameters of the fit. The finite orbit width correction is proportional to the ion temperature gradient and it becomes weaker at higher collisionality, because the ion orbits are interrupted more frequently.

A comparison of Hager's formula with the local j_{BS} solution from NEO is compared in Hager's work for three DIII-D like pedestals with different pedestal temperatures [168]. This is shown in figure 7.1. The pedestal profiles can be seen in figure 7.1a. The pedestal top collisionalities ($\nu*$) are 5.2, 2.0 and 0.9 for the 250 eV, 500 eV and 1000 eV pedestals, respectively. Figure 7.1b shows the bootstrap current profiles from the XGCa code (solid black), Hager's formula (dotted red), the NEO code (dashed green) and Sauter's formula (dotted-dashed blue). There is a small reduction in j_{BS} when the finite orbit width effect

[1] [168] refers to Δ_Ψ as the ion orbit width, but personal communication with the author has revealed that in eq. (17) in [168] Δ_Ψ is correctly defined as the half of the ion orbit width.

is taken into account (XGCa and Hager's formula) compared to the local solution (NEO). The difference is increasing with decreasing collisionality as expected from eq. (7.4).

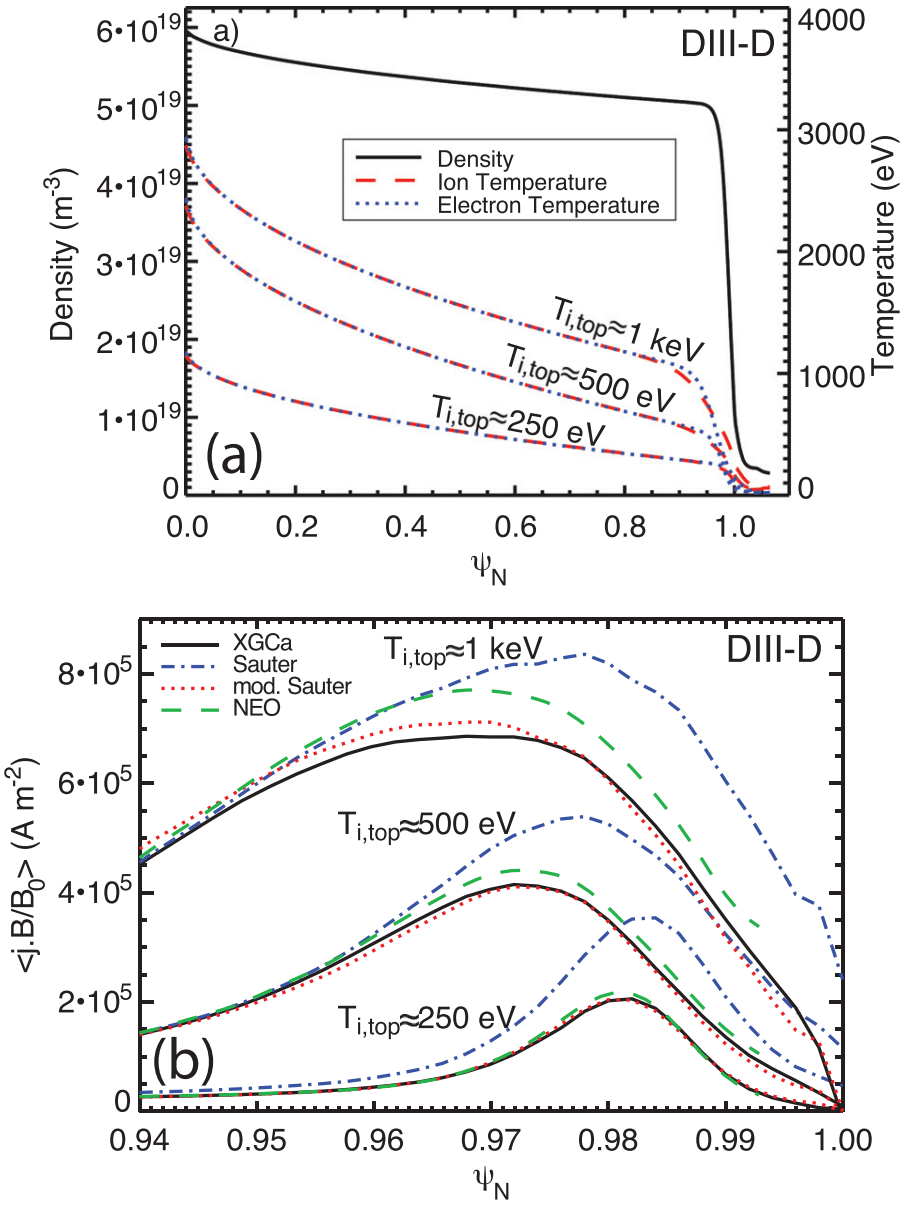

Figure 7.1: j_{BS} profiles calculated for DIII-D like pedestals with different pedestal temperatures. (a) Density and temperature profiles of the investigated pedestals. (b) j_{BS} profiles as evaluated with XGCa, NEO, Hager's formula and Sauter's formula. Figures are adapted from [168].

An attempt has been made to quantify the isotope dependence of the bootstrap current in JET-ILW pedestals with Hager's formula. j_{BS} profiles from NEO and Hager's formula assuming H ($A = 1$) and D ($A = 2$) isotope mass are show in figure 7.2 for the three reference discharges (#84793, #84796 and #91554) introduced in section 6.1 and for #84794, a D pulse from the same power scan as #84793 and #84796, but at higher input power ($P_{\mathrm{NBI}} = 16$ MW) to test low ν^* pedestals. It can be seen that the correction (with respect to the local NEO j_{BS}) introduced to account for finite orbit width effects

is slightly different in H and D. However, the relative magnitude of the finite orbit width correction is significantly higher in the lowest ν^* JET-ILW case (#84794) than in the DIII-D pedestals shown in figure 7.1. This is most probably due to the difference in ν^* (0.3 for #84794 and 0.5 for the 1000 eV DIII-D case) and the difference in ion orbit width normalised to the T_i gradient length, ρ_i/L_{T_i} (1 for #84794 and 0.4 for the 1000 eV DIII-D case). The unexpectedly large finite orbit width correction implies that the low collisionality JET-ILW pedestals may fall outside the validity domain of Hager's formula. In order to quantify the finite orbit width correction for j_{BS} and its isotope dependence, one would need to run the XGCa code on the specific JET-ILW cases. In conclusion, a small isotope dependence of the bootstrap current is expected due to finite orbit width effects, but accurate quantification of this effect is out of the scope of the thesis. Thus, any isotope dependence of the bootstrap current is not taken into account in the following sections. Note that if the finite orbit width correction is excluded from Hager's formula (dashed orange curves in figure 7.2), it closely reproduces the j_{BS} profiles calculated by NEO in the investigated pedestals.

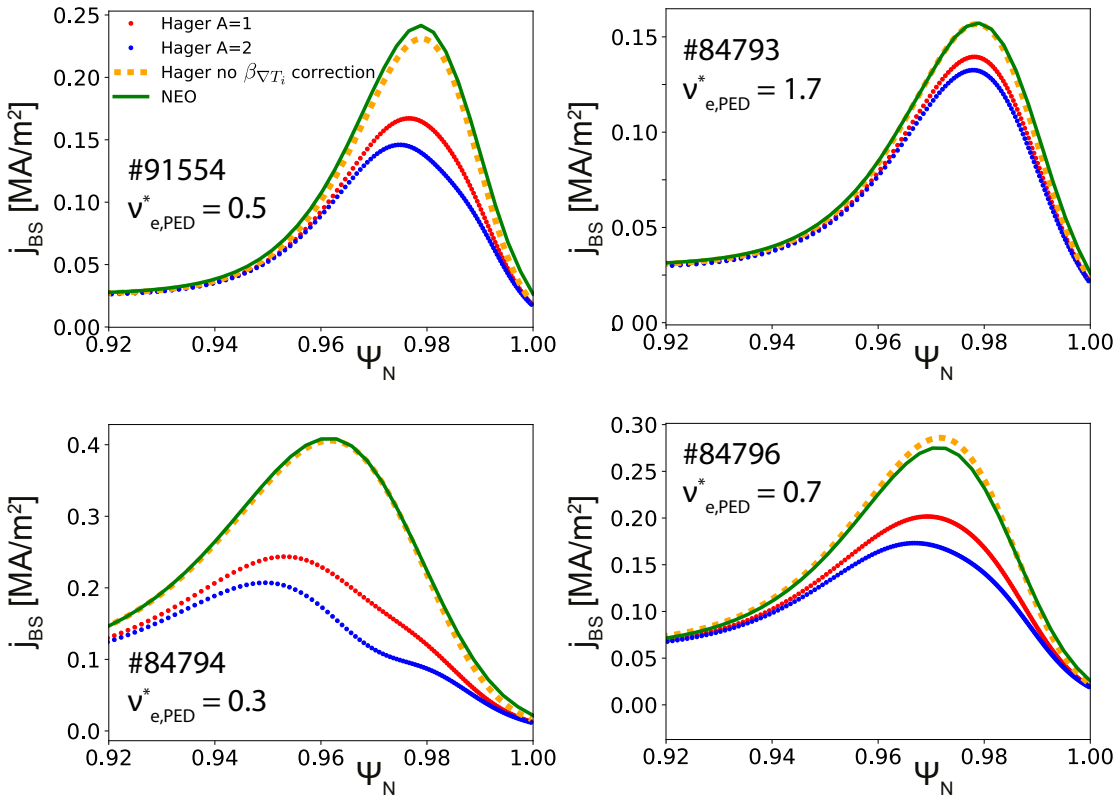

Figure 7.2: j_{BS} profiles calculated for JET-ILW pedestals using Hager's formula assuming different isotope mass ($A = 1$ and $A = 2$), Hager's formula without the finite orbit width correction and NEO.

7.2 Isotope dependence of linear MHD stability

The linear growth rate (γ_{MHD}) of ideal MHD modes scales as $\sim A^{-1/2}$. In numerical stability codes the stability criterion is often set as a small proportion ($c \approx 0.02 - 0.05$) of the Alfven-frequency: $\gamma_{\mathrm{MHD}} > c \times \omega_A$. As ω_A and γ_{MHD} scale with isotope mass in the same way, this stability criterion is independent of A.

An isotope dependence of the linear stability is introduced when diamagnetic stabilisation [196] is considered. The diamagnetic drift is expected to stabilise modes - particularly at high toroidal mode number n - when the diamagnetic frequency (ω_{dia}) is comparable to γ_{MHD}. $\omega_{\mathrm{dia}} = m/r \times T_i/(e_i B_0) \times \mathrm{d}\ln p_i/\mathrm{d}r$, where T_i, e_i and p_i are temperature, charge, and pressure of the ions, B_0 is the equilibrium magnetic field, r is the minor radius, and m is the poloidal mode number which is linked to the toroidal mode number (n) via the safety factor (q): $m = nq$. Diamagnetic stabilisation can be taken into account in ideal MHD stability analysis by modifying the stability criterion to $\gamma_{\mathrm{MHD}} > c \times \omega_{\mathrm{dia}}$ [62, 77]. As ω_{dia} is independent of A, but since $\gamma_{\mathrm{MHD}} \sim A^{-1/2}$, larger isotope mass leads to more stable pedestals when this stability criterion is applied.

Figure 7.3 shows the $j - \alpha$ pedestal stability diagram for the 3 reference discharges of section 6.1 as calculated with the HELENA equilibrium [197] and the ELITE ideal MHD stability codes [62, 63]. j is the normalised current density as calculated self-consistently with HELENA using Sauter's formula for the bootstrap current (j_{BS}) and assuming neoclassical resistivity and a fully diffused Ohmic current. Note that Sauter's formula has no isotope mass dependence. α is the normalised pressure gradient as defined in [74]. The inputs for HELENA/ELITE were the fitted kinetic profiles evaluated from Thomson scattering, assuming $T_e = T_i$ (consistent with charge exchange measurements), line averaged Z_{eff} with Be as a single impurity. The kinetic profiles here are radially aligned so that the separatrix temperature is 100 eV. The effect of $T_{\mathrm{e,sep}}$ on pedestal stability is discussed later in the next section.

In figure 7.3, the stability boundary (white dashed lines) is obtained using $\gamma_{\mathrm{MHD}} > 0.03 \times \omega_A$ stability criterion. The white stars show the operational point of the pedestal as obtained in the experiment. The pedestals in these low gas rate ($\Gamma = 3 \cdot 10^{21}$ e/s) H and D plasmas are close to the P-B boundary within the uncertainties of the operational point. This observation is confirmed with the same analysis performed on a wider dataset, although H pedestals tend to be on the stable side of the stability boundary. At medium and high gas rate, the operational point moves to the stable region in H, which is similar to what has been found in D at higher input power [53]. Pedestals of the 1.0 MA/1.0 T

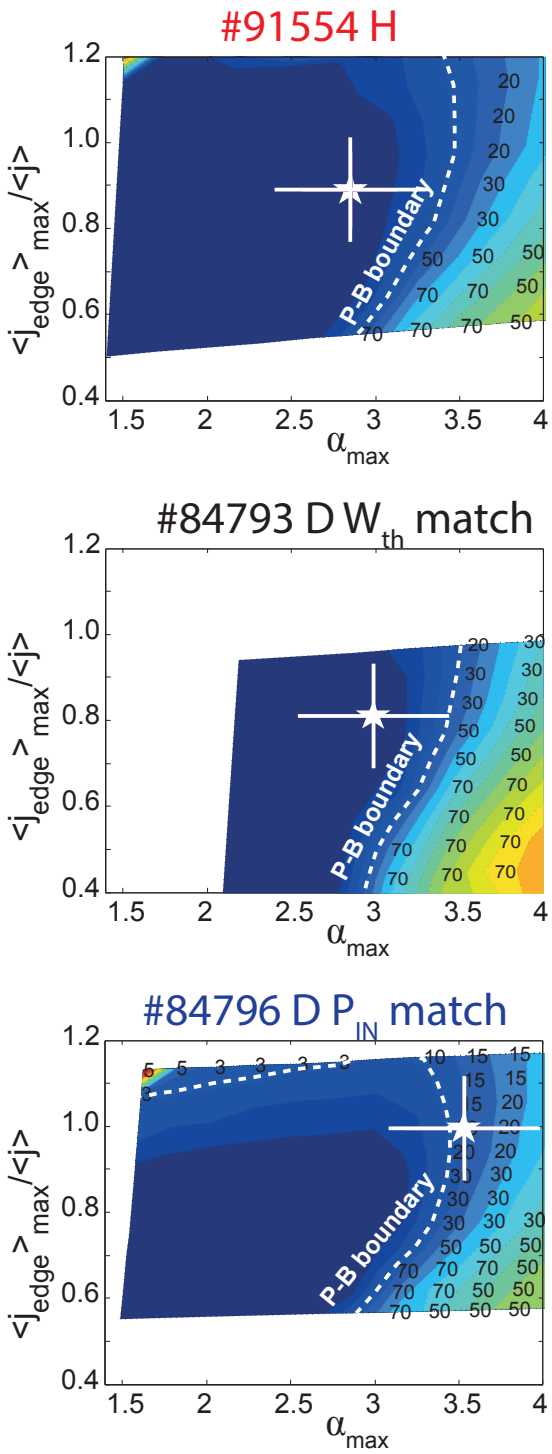

Figure 7.3: Linear MHD pedestal stability analysis for the hydrogen reference discharge (#91554) and the two deuterium plasmas matching the total stored energy (#84793) and the input power (#84796) of the hydrogen counterpart. I_p = 1.4 MA, B_t = 1.7 T.

dataset at medium gas are also stable to P-B modes both in H and D, especially at higher power.

The effect of diamagnetic stabilisation is investigated by performing linear ideal MHD stability analysis with HELENA/ELITE on the hydrogen pedestal. Figure 7.4 shows the

j-α stability diagram for H shot #91554 profiles using $\gamma_{\mathrm{MHD}} > 0.5 \times \omega_{\mathrm{dia}}$ as stability criterion, assuming $A = 2$ (dashed blue line) and $A = 1$ (solid red line) isotope. When diamagnetic stabilisation is taken into account, the stable region shrinks from $A = 2$ to $A = 1$ in the calculations indicating less stable pedestals. The critical pedestal pressure height can be evaluated by scaling up and down the experimental pressure profile and calculating the associated current profile self-consistently. The pressure profile which is closest to marginal stability gives the critical pressure gradient. The difference between the stability boundaries when the isotope mass is changed from $A = 2$ to $A = 1$ for discharge #91554 translates to ≈ 4 % reduction in the critical pedestal pressure height. Thus, the isotope dependence of linear MHD stability is small and alone does not explain the higher pedestal pressure observed in D type I ELMy H-modes in JET-ILW.

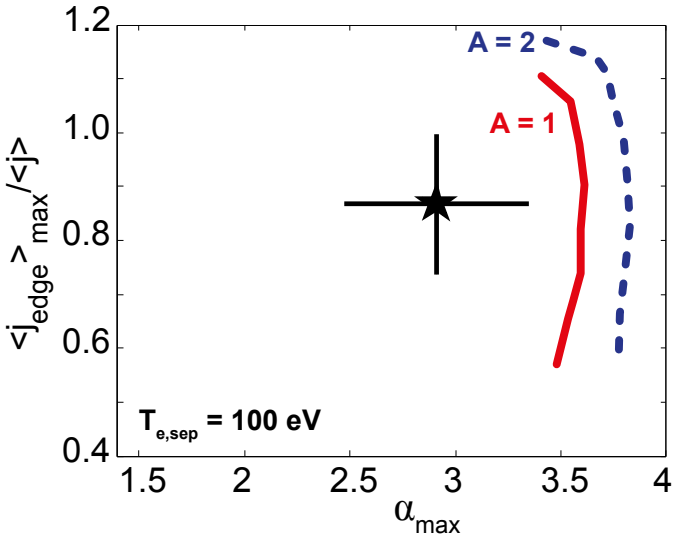

Figure 7.4: P-B stability of the pre-ELM pedestal of H type-I ELMy H-mode #91554 as calculated with HELENA/ELITE with the stability criterion $\gamma_{\mathrm{MHD}} > 0.5 \times \omega_{\mathrm{dia}}$. The black star indicates the operational point. The stable region shrinks when the isotope mass is changed from D (blue dashed line) to H (red solid line). The kinetic profiles are radially aligned so that $T_{e,sep} = 100$ eV.

The effect of diamagnetic stabilisation in JET pedestals has already been demonstrated using a more rigorous treatment of the diamagnetic drift with an extended MHD model [198, 199]. This approach could be the subject of further studies, however, the results of ideal MHD analysis used in the present work suggest that only a weak isotope dependence is expected. The effect of sheared rotation on pedestal stability [200] is not discussed here, but it may lead to differences in the pedestal stability between H and D plasmas, as for example the different input power to achieve the same pedestal pressure in H and D (see chapter 5) could lead to differences in the NBI torque and thus in the sheared rotation.

7.3 Effect of the separatrix temperature on pedestal stability

While so far the pedestal stability has been investigated assuming $T_{\mathrm{e,sep}} = 100$ eV for both H and D pedestals, now the effect of a potentially higher $T_{e,sep}$ in H on pedestal stability, as suggested by EDGE2D-EIRENE simulations presented in section 6.3, is assessed. The linear ideal MHD stability analysis for the hydrogen pulse #91554 is shown in figure 7.5a, assuming $T_{\mathrm{e,sep}} = 100$ eV (black), $T_{\mathrm{e,sep}} = 150$ eV (purple) and $T_{\mathrm{e,sep}} = 200$ eV (green) as a sensitivity test. The difference in boundary condition at the separatrix translates into significant differences in the linear MHD P-B stability boundary, with both ballooning and peeling boundaries shrinking due to destabilisation of P-B modes as $T_{\mathrm{e,sep}}$ is increased, similarly to the analysis reported in [195]. As illustrated in figure 7.5b, the higher $T_{e,sep}$ shifts the maximum pressure gradient closer to the separatrix, thus moving to a region of higher magnetic shear, which leads to destabilisation of ballooning modes. At the same time, the edge current profile - which is dominated by the bootstrap current - is also shifted radially outward, leading to higher current at the separatrix, which destabilises peeling modes. The difference in the critical pedestal pressure height between $T_{e,sep} \approx$ 100 eV and 200 eV cases is approximately 15 %. This change is qualitatively consistent with type I ELMs being triggered at lower pedestal densities in the H case. As described in section 6.3, however, such high $T_{\mathrm{e,sep}}$ in the H discharge is unrealistic and certainly too high, but the qualitative picture illustrated here warrants further investigation and direct measurement of $T_{\mathrm{e,sep}}$ in H and in D.

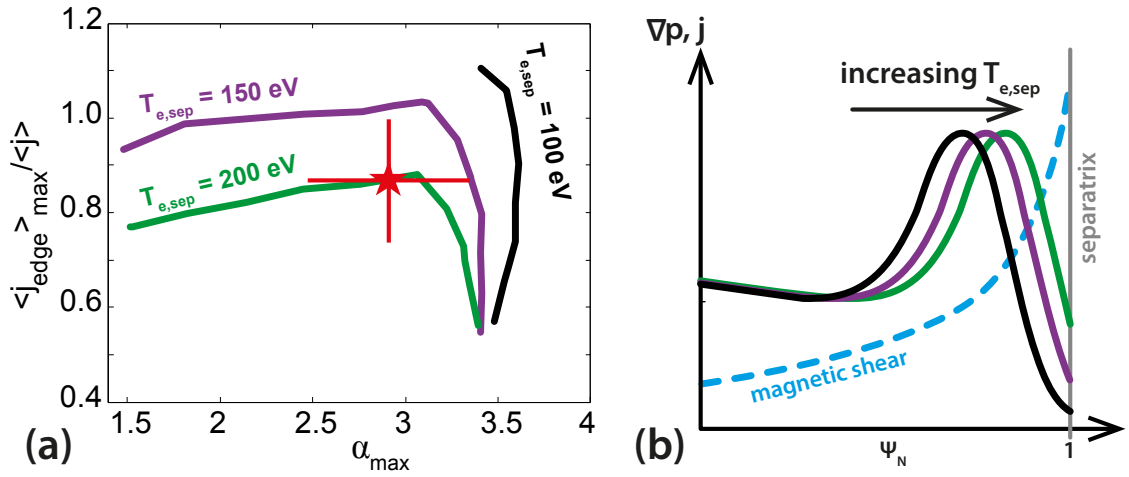

Figure 7.5: (a) Effect of $T_{\mathrm{e,sep}}$ on P-B stability of the pre-ELM pedestal of discharge #91554 as calculated with HELENA/ELITE using the stability criterion $\gamma_{\mathrm{MHD}} > 0.5 \times \omega_{\mathrm{dia}}$. The red star indicates the operational point of the pedestal for #91554. The stability boundary is shown assuming $T_{\mathrm{e,sep}} = 100$ eV (black), $T_{\mathrm{e,sep}} = 150$ eV (purple) and $T_{\mathrm{e,sep}} = 200$ eV (green). (b) Illustration of the maximum pressure gradient and edge current moving radially outwards, closer to the separatrix with increasing $T_{\mathrm{e,sep}}$ to a region with higher magnetic shear.

Chapter 8

Conclusions and future work

The work described in this thesis has contributed to the understanding of pedestal physics in H-mode plasmas with special attention to the isotope dependence. Since the pedestal structure determines the boundary condition for the core plasma transport, understanding of pedestal physics is essential to optimise the confinement in H-mode plasmas. In the first part of the thesis the inter-ELM evolution of the edge current density was investigated in an attempt to explain the ELM trigger in type I ELMy H-mode plasmas where the pedestals are stable to P-B modes. The second part focused on the isotope dependence of the pedestal with the aim to make a contribution towards better understanding of the pedestal in future DT plasmas. The main results of the thesis on linear MHD stability, ELM losses and neutral penetration can provide input for future pedestal simulation tools concerning which physics mechanisms need to be considered for accurate pedestal predictions.

Contributions to the physics of inter-ELM edge current evolution

The inter-ELM evolution of the edge current density has been studied in JET-ILW type I ELMy H-mode pedestals of varying collisionality and total plasma current. The bootstrap current density, which contributes most to the total edge current, has been evaluated with the neoclassical transport code NEO. In JET-ILW type I ELMy H-modes at low gas rate the peak j_{BS} is found to continuously increase during the ELM cycle. In contrast, with increasing gas rate the peak j_{BS} tends to saturate during the ELM cycle. The time evolution of j_{BS} closely follows that of ∇p_e, as expected, and ∇p_e is dominated by the $n_e \nabla T_e$ term.

The effect of current diffusion on the total edge current density has been investigated with the JETTO transport code. JET-ILW pedestals with varying $T_{\mathrm{e,PED}}$ and ELM

frequencies have been investigated in detail. The simulations show that there is no significant delay of the total edge current evolution with respect to the build-up of the pressure gradient inter-ELM. Sensitivity tests indicate that the conclusions are robust against ELM crash duration and/or ELM amplitude.

In the investigated pedestals, the resistive timescale was comparable to the ELM period, but the Ohmic current always redistributed in a way to mitigate the effect of the varying bootstrap current. As a result, the effect of current diffusion on the time evolution of the total edge current was not significant in the second half of the ELM cycle. Therefore, inter-ELM current diffusion could not explain why JET-ILW pedestals at high gas rate and high β_N are stable to P-B modes, as found in previous works by linear MHD stability analysis with HELENA/ELITE. It has also been observed that the electric field in the pedestal is typically larger in the early phase, and lower in the second half of the ELM cycle compared to the fully diffused state. This implies that the assumption of a fully diffused electric field used in HELENA/ELITE and HELENA/MISHKA may overestimate the total current in the pre-ELM phase. The deviation is not large, but it adds to all other uncertainties that feed into the edge stability analysis, such as those arising from the profile measurements and the bootstrap current models.

Contributions to understanding of the isotope dependence of the H-mode pedestal

In JET-ILW Hydrogen and Deuterium type I ELMy H-modes a favourable isotope scaling of the thermal energy confinement is observed and the isotope dependence originates at the pedestal in conditions where core $\nabla T/T$ is approximately constant. In the present thesis, the pedestal structure, linear MHD stability and ELM losses have been analysed to gain insight on the dependence of JET-ILW type I ELMy pedestals on the isotope mass.

The pedestal pressure is typically reduced in H compared to D at the same input power and gas rate, primarily due to lower pedestal density in H. The pedestal electron pressure gradient is typically lower in H than in D at similar pedestal pressure widths. The pedestal density width is typically narrower in H than in D, which is in contradiction to the neutral penetration model and implies that transport also plays a crucial role in setting the density pedestal. Interpretative EDGE2D-EIRENE simulations required higher anomalous perpendicular transport coefficients ($D_\perp$ and $\chi_\perp$) in H than in D to match the experimental edge kinetic profiles, indicating that the higher transport in H than in D is the main reason for the different pedestals and not neutral penetration.

The inter-ELM separatrix loss power is higher in H than in D at similar pedestal top pressure, similar to results from ASDEX-Upgrade. For the isotope dataset, the ELM losses are dominated by particle losses both in H and D plasmas. At low ELM frequencies ($f_{\mathrm{ELM}} \approx 10-20$ Hz), the ELM particle loss increases with increasing f_{ELM}, in correlation with decreasing pedestal top density. Thus, the typically higher ELM frequency in H than in D at the same input power and gas rate possibly contributes to density pump out leading to low pedestal density in H.

Pedestal linear MHD stability has been investigated in H and D, showing that P-B modes are more unstable at lower isotope mass. The direct isotope dependence of linear MHD pedestal stability becomes apparent when the diamagnetic frequency is included in the stability criterion to account for its stabilisation effect. P-B modes are more stable in D than in H, but the effect is small and alone does not explain the higher pedestal pressure observed in D. Interpretative EDGE2D-EIRENE simulations indicate that the electron temperature at the separatrix could be higher in H than in D in a pair of type I ELMy H-modes with similar stored energy achieved at twice the power in H, at low gas rate. The largest difference in boundary conditions at the separatrix between H and D translates into significant destabilisation of P-B modes for the H pedestal compared to D. This effect is qualitatively consistent with type I ELMs being triggered at lower pedestal densities in the H case, although the $T_{\mathrm{e,sep}}$ value in the sensitivity test was chosen as an extreme case and should not be considered at face value. The physics mechanism underlying the profile changes at the plasma edge when the isotope mass is varied is not yet understood. Note that direct measurement of the separatrix location would be needed in order to confirm or disprove the higher indicated $T_{\mathrm{e,sep}}$ in H than in D, but it is not available.

The results presented in this thesis indicate that ELM and inter-ELM transport and pedestal stability could possibly be affected by the isotope mass, leading to a favourable isotope dependence. Further studies are required to be able to provide quantitative predictions beyond the qualitative findings of this work. Changes in pedestal transport in T and DT plasmas with respect to H and D are expected to play an important role in the pedestal and global confinement. The indirect isotope dependence on pedestal MHD stability, through the separatrix temperature, is not considered to be dominant in T and DT, because at the higher densities expected in T and DT (compared to H and D) the divertor is likely to be in a conduction limited divertor regime, with similar target and upstream temperatures to those found in EDGE2D-EIRENE for the D case.

Future work

Future work should include further studies with the EDGE2D-EIRENE code to examine the role of the particle source and transport in setting the density pedestal. These could also investigate the relative importance of ELM and inter-ELM particle losses by utilising time dependent simulations with simplified ELM models.

Further experiments are planned in the upcoming JET campaigns to examine the ELM particle losses in different isotopes by applying ELM trigger techniques to match the ELM frequency in H, D and T plasmas. Experimental analysis and interpretative edge transport analysis suggest that the pedestal transport is likely to play an important role in setting the pedestal height and shape and may be the primary difference between H and D pedestals. Thus, future work should also focus on studying the turbulence driving the inter-ELM pedestal transport with gyrokinetic simulations, which is ongoing.

Bibliography

[1] European Physical Society. *Energy for the future - EPS position paper on the nuclear option*. Press release of the European Physical Society, 2007.

[2] EUROfusion. *European Research Roadmap to the Realisation of Fusion Energy*. EUROfusionProgramme Management Unit, 2018.

[3] H. A. Bethe. Energy production in stars. *Phys. Rev.*, 55(5):434–456, 1939.

[4] D. D. Clayton. *Principles of Stellar Evolution and Nucleosynthesis*. University of Chicago Press, 1983.

[5] J. P. Freidberg. *Plasma Physics and Fusion Energy*. Cambridge Unversity Press, 2008.

[6] T. J. Dolan. *Fusion Research*. Pergamon Press, corrected edition, 2000.

[7] J. Wesson. *Tokamaks*. Oxford University Press, Oxford, fourth edition, 2011.

[8] M. Kikuchi, K. Lackner, and M. Q. Tran. *Fusion Physics*. International Atomic Energy Agency, Vienna, 2012.

[9] S. C. Cowley. The quest for fusion power. *Nature Physics*, 12:384–386, 2016.

[10] A. A. Harms, D. R. Kingdon, K. F. Schoepf, and G. H. Miley. *Principles of Fusion Energy*. World Scientific, 2000.

[11] J. D. Lawson. Some criteria for a power producing thermonuclear reactor. *Proceedings of the Physical Society. Section B*, 70(1):6–10, 1957.

[12] P. M. Bellan. *Fundamentals of Plasma Physics*. Cambridge Unversity Press, 2008.

[13] J. P. Freidberg. *Ideal MHD*. Cambridge University Press, 2014.

[14] X. Litaudon et al. Overview of the JET results in support to ITER. *Nuclear Fusion*, 57(10):102001, 2017.

[15] A. Kallenbach. Overview of ASDEX Upgrade results. *Nuclear Fusion*, 57(10):102015, 2017.

[16] W. M. Solomon. DIII-D research advancing the scientific basis for burning plasmas and fusion energy. *Nuclear Fusion*, 57(10):102018, 2017.

[17] N. Oyama. Overview of JT-60U results towards the establishment of advanced tokamak operation. *Nuclear Fusion*, 49(10):104007, 2009.

[18] H. Shirai, P. Barabaschi, and Y. Kamada. Recent progress of the JT-60SA project. *Nuclear Fusion*, 57(10):102002, 2017.

[19] J. G. Kwak et al. An overview of KSTAR results. *Nuclear Fusion*, 53(10):104005, 2013.

[20] B. N. Wan et al. Overview of EAST experiments on the development of high-performance steady-state scenario. *Nuclear Fusion*, 57(10):102019, 2017.

[21] M. Keilhacker, A. Gibson, C. Gormezano, P. J. Lomas, et al. High fusion performance from deuterium-tritium plasmas in JET. *Nuclear Fusion*, 39(2):209–234, 1999.

[22] ITER Organization. ITER Research Plan within the Staged Approach. *ITER Techinal Report*, ITR-18-003, 2018.

[23] P. Helander and D. J. Sigmar. *Collisional Transport in Magnetized Plasmas*. Cambridge University Press, 2005.

[24] P. J. Catto. Linearized gyro-kinetics. *Plasma Physics*, 20(7):719–722, 1978.

[25] T. S. Hahm. Nonlinear gyrokinetic equations for tokamak microturbulence. *The Physics of Fluids*, 31(9):2670–2673, 1988.

[26] A. J. Brizard and T. S. Hahm. Foundations of nonlinear gyrokinetic theory. *Rev. Mod. Phys.*, 79(2):421–468, 2007.

[27] F. Wagner, G. Becker, K. Behringer, D. Campbell, et al. Regime of improved confinement and high beta in neutral-beam-heated divertor discharges of the ASDEX tokamak. *Phys. Rev. Lett.*, 49(19):1408–1412, 1982.

[28] P. H. Diamond, S. I. Itoh, K. Itoh, and T. S. Hahm. Zonal flows in plasma - a review. *Plasma Physics and Controlled Fusion*, 47(5):R35–R161, 2005.

[29] L. Schmitz, L. Zeng, T. L. Rhodes, J. C. Hillesheim, et al. Role of zonal flow predator-prey oscillations in triggering the transition to H-mode confinement. *Phys. Rev. Lett.*, 108(15):155002, 2012.

[30] M. Greenwald, R. L. Boivin, F. Bombarda, P. T. Bonoli, et al. H mode confinement in Alcator C-Mod. *Nuclear Fusion*, 37(6):793–807, 1997.

[31] C. F. Maggi, R. J. Groebner, N. Oyama, R. Sartori, et al. Characteristics of the H-mode pedestal in improved confinement scenarios in ASDEX Upgrade, DIII-D, JET and JT-60U. *Nuclear Fusion*, 47(7):535, 2007.

[32] L. D. Horton, J. P. Christiansen, J. Lingertat, C. F. Maggi, et al. Performance near operational boundaries. *Plasma Physics and Controlled Fusion*, 41(12B):B329–B341, 1999.

[33] P. Mantica, C. Angioni, B. Baiocchi, M. Baruzzo, et al. Ion heat transport studies in JET. *Plasma Physics and Controlled Fusion*, 53(12):124033, 2011.

[34] H. Zohm. Edge localized modes (ELMs). *Plasma Physics and Controlled Fusion*, 38(2):105, 1996.

[35] J. W. Connor. Edge-localized modes - physics and theory. *Plasma Physics and Controlled Fusion*, 40(5):531–542, 1998.

[36] W. Suttrop. The physics of large and small edge localized modes. *Plasma Physics and Controlled Fusion*, 42(5A):A1–A14, 2000.

[37] A. W. Leonard, A. Herrmann, K. Itami, J. Lingertat, et al. The impact of ELMs on the ITER divertor. *Journal of Nuclear Materials*, 266-269:109–117, 1999.

[38] A. Loarte, G. Saibene, R. Sartori, D. Campbell, et al. Characteristics of type I ELM energy and particle losses in existing devices and their extrapolation to ITER. *Plasma Physics and Controlled Fusion*, 45(9):1549–1569, 2003.

[39] A. Loarte, B. Lipschultz, A. S. Kukushkin, G. F. Matthews, et al. Chapter 4: Power and particle control. *Nuclear Fusion*, 47(6):S203–S263, 2007.

[40] P. T. Lang, A. Loarte, G. Saibene, L. R. Baylor, et al. ELM control strategies and tools: status and potential for ITER. *Nuclear Fusion*, 53(4):043004, 2013.

[41] F. Wagner. A quarter-century of H-mode studies. *Plasma Physics and Controlled Fusion*, 49(12B):B1–B33, 2007.

[42] J. Roth, E. Tsitrone, T. Loarer, V. Philipps, et al. Tritium inventory in ITER plasma-facing materials and tritium removal procedures. *Plasma Physics and Controlled Fusion*, 50(10):103001, 2008.

[43] ITER Physics Expert Group on Divertor, ITER Physics Expert Group on Divertor Modelling and Database, and ITER Physics Basis Editors. Chapter 4: Power and particle control. *Nuclear Fusion*, 39(12):2391–2469, 1999.

[44] V. Philipps, Ph. Mertens, G. F. Matthews, and H. Maier. Overview of the JET ITER-like wall project. *Fusion Engineering and Design*, 85(7):1581–1586, 2010. Proceedings of the Ninth International Symposium on Fusion Nuclear Technology.

[45] D. Ciric, A. D. Ash, B. Crowley, I. E. Day, et al. Performance of upgraded JET neutral beam injectors. *Fusion Engineering and Design*, 86(6):509–512, 2011.

[46] L. Horton, P. Batistoni, H. Boyer, C. Challis, et al. JET experiments with tritium and deuterium–tritium mixtures. *Fusion Engineering and Design*, 109-111:925–936, 2016.

[47] E. Lerche, M. Goniche, P. Jacquet, D. Van Eester, et al. Impact of localized gas injection on ICRF coupling and SOL parameters in JET-ILW H-mode plasmas. *Journal of Nuclear Materials*, 463:634–639, 2015.

[48] G. F. Matthews, P. Edwards, T. Hirai, M. Kear, et al. Overview of the ITER-like wall project. *Physica Scripta*, T128:137–143, 2007.

[49] G. F. Matthews, M. Beurskens, S. Brezinsek, M. Groth, et al. JET ITER-like wall - overview and experimental programme. *Physica Scripta*, PT145:014001, 2011.

[50] S. Brezinsek, T. Loarer, V. Philipps, H. G. Esser, et al. Fuel retention studies with the ITER-like wall in JET. *Nuclear Fusion*, 53(8):083023, 2013.

[51] M. N. A. Beurskens, J. Schweinzer, C. Angioni, A. Burckhart, et al. The effect of a metal wall on confinement in JET and ASDEX Upgrade. *Plasma Physics and Controlled Fusion*, 55(12):124043, 2013.

[52] M. N. A. Beurskens, L. Frassinetti, C. Challis, C. Giroud, et al. Global and pedestal confinement in JET with a Be/W metallic wall. *Nuclear Fusion*, 54(4):043001, 2014.

[53] C. F. Maggi, S. Saarelma, F. J. Casson, C. Challis, et al. Pedestal confinement and stability in JET-ILW ELMy H-modes. *Nuclear Fusion*, 55(11):113031, 2015.

[54] C. F. Maggi, L. Frassinetti, L. Horvath, A. Lunniss, et al. Studies of the pedestal structure and inter-ELM pedestal evolution in JET with the ITER-like wall. *Nuclear Fusion*, 57(11):116012, 2017.

[55] C. Giroud, G. P. Maddison, S. Jachmich, F. Rimini, et al. Impact of nitrogen seeding on confinement and power load control of a high-triangularity JET ELMy H-mode plasma with a metal wall. *Nuclear Fusion*, 53(11):113025, 2013.

[56] C. D. Challis, J. Garcia, M. Beurskens, P. Buratti, et al. Improved confinement in JET high beta plasmas with an ITER-like wall. *Nuclear Fusion*, 55(5):053031, 2015.

[57] H. T. Kim, A. C. C. Sips, M. Romanelli, C. D. Challis, et al. High fusion performance at high Ti/Te in JET-ILW baseline plasmas with high NBI heating power and low gas puffing. *Nuclear Fusion*, 58(3):036020, 2018.

[58] E. Joffrin et al. Overview of the JET preparation for deuterium-tritium operation with the ITER like-wall. *Nuclear Fusion*, 59(11):112021, 2019.

[59] F. J. Casson, H. Patten, C. Bourdelle, S. Breton, et al. Predictive multi-channel flux-driven modelling to optimise ICRH tungsten control and fusion performance in JET. *to be submitted to Nuclear Fusion*, 2019.

[60] R. Lasser, A. C. Bell, N. Bainbridge, P. D. Brennan, et al. Overview of the performance of the JET Active Gas Handling System during and after DTE1. *Fusion Engineering and Design*, 47(2):173–203, 1999.

[61] E. J. Doyle, W. A. Houlberg, Y. Kamada, V. Mukhovatov, et al. Chapter 2: Plasma confinement and transport. *Nuclear Fusion*, 47(6):S18–S127, 2007.

[62] P. B. Snyder, H. R. Wilson, J. R. Ferron, L. L. Lao, et al. Edge localized modes and the pedestal: A model based on coupled peeling-ballooning modes. *Physics of Plasmas*, 9(5):2037–2043, 2002.

[63] H. R. Wilson, P. B. Snyder, G. T. A. Huysmans, and R. L. Miller. Numerical studies of edge localized instabilities in tokamaks. *Physics of Plasmas*, 9(4):1277–1286, 2002.

[64] R. Fitzpatrick. *Plasma Physics: An Introduction*. CRC Press, 2014.

[65] H. Grad and H. Rubin. Hydromagnetic equilibria and force-free fields. In *Proceedings of the Second United Nations International Conference on the Peaceful Uses of Atomic Energy, Geneva*, volume 31, page 190, 1958.

[66] V. D. Shafranov. Plasma Equilibrium in a Magnetic Field. *Reviews of Plasma Physics*, 2:103, 1966.

[67] H. Zohm. *Magnetohydrodynamic Stability of Tokamaks*. Wiley, 2014.

[68] A. G. Peeters. The bootstrap current and its consequences. *Plasma Physics and Controlled Fusion*, 42(12B):B231, 2000.

[69] J. Wesson. *The Science of JET*. JET-R(99)13, 1999.

[70] H. R. Wilson, S. C. Cowley, A. Kirk, and P. B. Snyder. Magneto-hydrodynamic stability of the H-mode transport barrier as a model for edge localized modes: an overview. *Plasma Physics and Controlled Fusion*, 48(5A):A71–A84, 2006.

[71] J. W. Connor, R. J. Hastie, and J. B. Taylor. Shear, periodicity, and plasma ballooning modes. *Phys. Rev. Lett.*, 40(6):396–399, 1978.

[72] J. W. Connor, R. J. Hastie, H. R. Wilson, and R. L. Miller. Magnetohydrodynamic stability of tokamak edge plasmas. *Physics of Plasmas*, 5(7):2687–2700, 1998.

[73] S. Saarelma, A. Alfier, M. N. A. Beurskens, R. Coelho, et al. MHD stability analysis of small ELM regimes in JET. *Plasma Physics and Controlled Fusion*, 51(3):035001, 2009.

[74] R. L. Miller, M. S. Chu, J. M. Greene, Y. R. Lin-Liu, et al. Noncircular, finite aspect ratio, local equilibrium model. *Physics of Plasmas*, 5(4):973–978, 1998.

[75] S. Saarelma, L. Frassinetti, P. Bilkova, C. D. Challis, et al. Self-consistent pedestal prediction for JET-ILW in preparation of the DT campaign. *Physics of Plasmas*, 26(7):072501, 2019.

[76] P. B. Snyder, R. J. Groebner, A. W. Leonard, T. H. Osborne, et al. Development and validation of a predictive model for the pedestal height. *Physics of Plasmas*, 16(5):056118, 2009.

[77] P. B. Snyder, R. J. Groebner, J. W. Hughes, T. H. Osborne, et al. A first-principles predictive model of the pedestal height and width: development, testing and ITER optimization with the EPED model. *Nuclear Fusion*, 51(10):103016, 2011.

[78] W. M. Tang, J. W. Connor, and R. J. Hastie. Kinetic-ballooning-mode theory in general geometry. *Nuclear Fusion*, 20(11):1439–1453, 1980.

[79] B. D. Scott. Computation of electromagnetic turbulence and anomalous transport mechanisms in tokamak plasmas. *Plasma Physics and Controlled Fusion*, 45(12A):A385–A398, 2003.

[80] J. Candy. Beta scaling of transport in microturbulence simulations. *Physics of Plasmas*, 12(7):072307, 2005.

[81] P. B. Snyder and G. W. Hammett. Electromagnetic effects on plasma microturbulence and transport. *Physics of Plasmas*, 8(3):744–749, 2001.

[82] S. Saarelma, M. N. A. Beurskens, D. Dickinson, L. Frassinetti, et al. MHD and gyro-kinetic stability of JET pedestals. *Nuclear Fusion*, 53(12):123012, 2013.

[83] H. Urano, T. Takizuka, Y. Kamada, N. Oyama, et al. Dimensionless parameter dependence of H-mode pedestal width using hydrogen and deuterium plasmas in JT-60U. *Nuclear Fusion*, 48(4):045008, 2008.

[84] R. J. Groebner and T. H. Osborne. Scaling studies of the high mode pedestal. *Physics of Plasmas*, 5(5):1800–1806, 1998.

[85] T. H. Osborne, K. H. Burrell, R. J. Groebner, L. L. Lao, et al. H-mode pedestal characteristics in ITER shape discharges on DIII-D. *Journal of Nuclear Materials*, 266-269:131–137, 1999.

[86] P. B. Snyder, N. Aiba, M. Beurskens, R. J. Groebner, et al. Pedestal stability comparison and ITER pedestal prediction. *Nuclear Fusion*, 49(8):085035, 2009.

[87] M. N. A. Beurskens, T. H. Osborne, P. A. Schneider, E. Wolfrum, et al. H-mode pedestal scaling in DIII-D, ASDEX Upgrade, and JET. *Physics of Plasmas*, 18(5):056120, 2011.

[88] J. R. Walk, P. B. Snyder, J. W. Hughes, J. L. Terry, et al. Characterization of the pedestal in Alcator C-mod ELMing H-modes and comparison with the EPED model. *Nuclear Fusion*, 52(6):063011, 2012.

[89] R. J. Groebner, C. S. Chang, J. W. Hughes, R. Maingi, et al. Improved understanding of physics processes in pedestal structure, leading to improved predictive capability for ITER. *Nuclear Fusion*, 53(9):093024, 2013.

[90] M. J. Leyland, M. N. A. Beurskens, L. Frassinetti, C. Giroud, et al. The H-mode pedestal structure and its role on confinement in JET with a carbon and metal wall. *Nuclear Fusion*, 55(1):013019, 2014.

[91] L. Frassinetti, M. N. A. Beurskens, S. Saarelma, J. E. Boom, et al. Global and pedestal confinement and pedestal structure in dimensionless collisionality scans of low-triangularity H-mode plasmas in JET-ILW. *Nuclear Fusion*, 57(1):016012, 2016.

[92] S. Saarelma, C. D. Challis, L. Garzotti, L. Frassinetti, et al. Integrated modelling of H-mode pedestal and confinement in JET-ILW. *Plasma Physics and Controlled Fusion*, 60(1):014042, 2017.

[93] J. M. Park, J. R. Ferron, C. T. Holcomb, R. J. Buttery, et al. Integrated modeling of high betaN steady state scenario on DIII-D. *Physics of Plasmas*, 25(1):012506, 2018.

[94] J. Y. Kim, H. S. Han, and L. Terzolo. Physics-based integrated modeling of the energy confinement time scaling laws for the H- and L-modes in the KSTAR-type tokamak model. *Nuclear Fusion*, 57(7):076012, 2017.

[95] T. Luda, C. Angioni, M. Dunne, E. Fable, et al. Integrated modelling of plasma confinement combining core and edge pedestal physics. In *23rd Joint EU-US Transport Task Force Meeting, Seville, Spain*, 2018.

[96] T. Luda, C. Angioni, M. Dunne, E. Fable, et al. Integrated modeling of tokamak plasma confinement. In *46th EPS Conference on Plasma Physics, Milan, Italy*, page P5.1088, 2019.

[97] R. J. Groebner, M. A. Mahdavi, A. W. Leonard, T. H. Osborne, et al. The role of neutrals in high-mode (H-mode) pedestal formation. *Physics of Plasmas*, 9(5):2134–2140, 2002.

[98] D. R. Hatch, M. Kotschenreuther, S. Mahajan, P. Valanju, et al. Microtearing turbulence limiting the JET-ILW pedestal. *Nuclear Fusion*, 56(10):104003, 2016.

[99] D. R. Hatch, M. Kotschenreuther, S. Mahajan, P. Valanju, et al. A gyrokinetic perspective on the JET-ILW pedestal. *Nuclear Fusion*, 57(3):036020, 2017.

[100] M. Kotschenreuther, D.R. Hatch, S. Mahajan, P. Valanju, et al. Pedestal transport in H-mode plasmas for fusion gain. *Nuclear Fusion*, 57(6):064001, 2017.

[101] M. Kotschenreuther, X. Liu, D. R. Hatch, S. Mahajan, et al. Gyrokinetic analysis and simulation of pedestals to identify the culprits for energy losses using 'fingerprints'. *Nuclear Fusion*, 59(9):096001, 2019.

[102] D. R. Hatch, M. Kotschenreuther, S. M. Mahajan, G. Merlo, et al. Direct gyrokinetic comparison of pedestal transport in JET with carbon and ITER-like walls. *Nuclear Fusion*, 59(8):086056, 2019.

[103] C. Giroud, N. Aiba, A. Chankin, D. Hatch, et al. Optimisation of JET-DT and ITER operation by developing an understanding of the role of low-Z impurity on the H-mode pedestal. In *27th IAEA Fusion Energy Conference, Ahmedabad, India*, pages EX/3–4, 2018.

[104] C. F. Maggi, H. Weisen, J. C. Hillesheim, A. Chankin, et al. Isotope effects on L-H threshold and confinement in tokamak plasmas. *Plasma Physics and Controlled Fusion*, 60(1):014045, 2017.

[105] H. Urano, T. Takizuka, T. Fujita, Y. Kamada, et al. Energy confinement of hydrogen and deuterium H-mode plasmas in JT-60U. *Nuclear Fusion*, 52(11):114021, 2012.

[106] H. Urano, T. Takizuka, N. Aiba, M. Kikuchi, et al. Hydrogen isotope effects on ITG scale length, pedestal and confinement in JT-60 H-mode plasmas. *Nuclear Fusion*, 53(8):083003, 2013.

[107] D. P. Schissel, K. H. Burrell, J. C. DeBoo, R. J. Groebner, et al. Energy confinement properties of H-mode discharges in the DIII-D tokamak. *Nuclear Fusion*, 29(2):185–197, 1989.

[108] ASDEX Team. The H-Mode of ASDEX. *Nuclear Fusion*, 29(11):1959–2040, 1989.

[109] M. Bessenrodt-Weberpals, F. Wagner, O. Gehre, L. Giannone, et al. The isotope effect in ASDEX. *Nuclear Fusion*, 33(8):1205–1238, 1993.

[110] F. M. Laggner, E. Wolfrum, M. Cavedon, F. Mink, et al. Pedestal structure and inter-ELM evolution for different main ion species in ASDEX Upgrade. *Physics of Plasmas*, 24(5):056105, 2017.

[111] ITER Physics Basis Editors, ITER Physics Expert Group Chairs and Co-Chairs, and ITER Joint Central Team and Physics Unit. Chapter 1: Overview and summary. *Nuclear Fusion*, 39(12):2137–2174, 1999.

[112] ITER Physics Expert Group on Confinement and Transport, ITER Physics Expert Group on Confinement Modelling and Database, and ITER Physics Basis Editors. Chapter 2: Plasma confinement and transport. *Nuclear Fusion*, 39(12):2175–2249, 1999.

[113] W. Horton. Drift waves and transport. *Rev. Mod. Phys.*, 71(3):735–778, 1999.

[114] R. E. Waltz, J. C. DeBoo, and M. N. Rosenbluth. Magnetic-field scaling of dimensionally similar tokamak discharges. *Phys. Rev. Lett.*, 65(19):2390–2393, 1990.

[115] T. C. Luce, C. C. Petty, and J. G. Cordey. Application of dimensionless parameter scaling techniques to the design and interpretation of magnetic fusion experiments. *Plasma Physics and Controlled Fusion*, 50(4):043001, 2008.

[116] G. Bateman, A. H. Kritz, V. Parail, and J. G. Cordey. Effect of isotope mass on transport simulations of Joint European Torus high-mode plasmas with Edge Localized Modes. *Physics of Plasmas*, 6(12):4607–4614, 1999.

[117] R. E. Waltz, J. C. DeBoo, and T. H. Osborne. Modelling of almost dimensionally similar discharges. *Nuclear Fusion*, 32(6):1051–1056, 1992.

[118] G. M. Staebler, J. E. Kinsey, and R. E. Waltz. A theory-based transport model with comprehensive physics. *Physics of Plasmas*, 14(5):055909, 2007.

[119] G. M. Staebler, N. T. Howard, J. Candy, and C. Holland. A model of the saturation of coupled electron and ion scale gyrokinetic turbulence. *Nuclear Fusion*, 57(6):066046, 2017.

[120] C. F. Maggi, H. Weisen, F. J. Casson, F. Auriemma, et al. Isotope identity experiments in JET-ILW with H and D L-mode plasmas. *Nuclear Fusion*, 59(7):076028, 2019.

[121] P. A. Schneider, A. Bustos, P. Hennequin, F. Ryter, et al. Explaining the isotope effect on heat transport in L-mode with the collisional electron-ion energy exchange. *Nuclear Fusion*, 57(6):066003, 2017.

[122] S. M. Kaye, M. Greenwald, U. Stroth, O. Kardaun, et al. ITER L mode confinement database. *Nuclear Fusion*, 37(9):1303–1328, 1997.

[123] E. Delabie, N. C. Hawkes, S. Menmuir, A. Meigs, et al. Development of main ion CXS for ion heat and momentum transport studies on JET-ILW. In *23rd Joint EU-US Transport Task Force Meeting, Seville, Spain*, 2018.

[124] F. J. Casson. The challenge and reward of predictive multi-channel modelling. In *23rd Joint EU-US Transport Task Force Meeting, Seville, Spain*, 2018.

[125] I. Pusztai, J. Candy, and P. Gohil. Isotope mass and charge effects in tokamak plasmas. *Physics of Plasmas*, 18(12):122501, 2011.

[126] J. Garcia, T. Görler, and F. Jenko. Isotope and fast ions turbulence suppression effects: Consequences for high-beta ITER plasmas. *Physics of Plasmas*, 25(5):055902, 2018.

[127] R. E. Waltz, R. L. Dewar, and X. Garbet. Theory and simulation of rotational shear stabilization of turbulence. *Physics of Plasmas*, 5(5):1784–1792, 1998.

[128] J. Garcia, T. Görler, F. Jenko, and G. Giruzzi. Gyrokinetic nonlinear isotope effects in tokamak plasmas. *Nuclear Fusion*, 57(1):014007, 2017.

[129] M. Oberparleiter, C. F. Maggi, F. J. Casson, P. Strand, et al. Gyrokinetic studies of the isotope effect in JET-ILW H-mode discharges. In *23rd Joint US-EU Transport Task Force Meeting, Seville*, 2018.

[130] N. Bonanomi, I. Casiraghi, P. Mantica, C. Challis, et al. Role of fast ion pressure in the isotope effect in JET L-mode plasmas. *Nuclear Fusion*, 59(9):096030, 2019.

[131] J. G. Cordey, B. Balet, D. V. Bartlett, R. V. Budny, et al. Plasma confinement in JET H mode plasmas with H, D, DT and T isotopes. *Nuclear Fusion*, 39(3):301, 1999.

[132] M. Maslov, A. Boboc, M. Brix, J. Flanagan, et al. Energy and particle confinement in JET H-mode plasma. *to be submitted to Nuclear Fusion*, 2019.

[133] Y. Kamada, H. Takenaga, A. Isayama, T. Hatae, et al. Pedestal characteristics and extended high beta poloidal ELMy H-mode regime in JT-60U. *Plasma Physics and Controlled Fusion*, 44(5A):A279–A286, 2002.

[134] P. B. Snyder, K. H. Burrell, H. R. Wilson, M. S. Chu, et al. Stability and dynamics of the edge pedestal in the low collisionality regime: physics mechanisms for steady-state ELM-free operation. *Nuclear Fusion*, 47(8):961, 2007.

[135] A. W. Leonard, R. J. Groebner, T. H. Osborne, and P. B. Snyder. Influence of global beta, shape, and rotation on the H-mode pedestal structure in DIII-D. *Physics of Plasmas*, 15(5):056114, 2008.

[136] P. A. Schneider, C. Angioni, M. Dunne, M. Cavedon, et al. Experimental separation of core transport and edge pedestal isotope dependencies by variation of the plasma shape. In *45th EPS Conference on Plasma Physics, Prague*, page P5.1078, 2018.

[137] P. A. Schneider, N. Bonanomi, C. Angioni, P. Hennequin, et al. Investigation of core transport properties with different isotope masses for matched edge conditions. In *24th Joint US-EU Transport Task Force Meeting, Austin*, 2019.

[138] H. Weisen, C. F. Maggi, L. Horvath, F. Auriemma, et al. Isotope dependence of confinement in JET Deuterium and Hydrogen plasmas. In *27th IAEA Fusion Energy Conference, Ahmedabad, India*, pages EX/P1–4, 2018.

[139] A. Burckhart, E. Wolfrum, R. Fischer, K. Lackner, et al. Inter-ELM behaviour of the electron density and temperature pedestal in ASDEX Upgrade. *Plasma Physics and Controlled Fusion*, 52(10):105010, 2010.

[140] F. M. Laggner, E. Wolfrum, M. Cavedon, M. G. Dunne, et al. Plasma shaping and its impact on the pedestal of ASDEX Upgrade: edge stability and inter-ELM dynamics at varied triangularity. *Nuclear Fusion*, 58(4):046008, 2018.

[141] A. Diallo, R. J. Groebner, T. L. Rhodes, D. J. Battaglia, et al. Correlations between quasi-coherent fluctuations and the pedestal evolution during the inter-edge localized modes phase on DIII-D. *Physics of Plasmas*, 22(5):056111, 2015.

[142] A. Diallo, J. W. Hughes, S. G. Baek, B. LaBombard, et al. Quasi-coherent fluctuations limiting the pedestal growth on Alcator C-Mod: experiment and modelling. *Nuclear Fusion*, 55(5):053003, 2015.

[143] M. G. Dunne, P. J. McCarthy, E. Wolfrum, R. Fischer, et al. Measurement of neoclassically predicted edge current density at ASDEX Upgrade. *Nuclear Fusion*, 52(12):123014, 2012.

[144] E. A. Belli and J. Candy. Kinetic calculation of neoclassical transport including self-consistent electron and impurity dynamics. *Plasma Physics and Controlled Fusion*, 50(9):095010, 2008.

[145] E. A. Belli and J. Candy. Full linearized Fokker-Planck collisions in neoclassical transport simulations. *Plasma Physics and Controlled Fusion*, 54(1):015015, 2012.

[146] G. Cenacchi and A. Taroni. JETTO: A free-boundary plasma transport code. *JET Joint Undertaking, Abingdon*, JET-IR(88)03, 1988.

[147] R. Pasqualotto, P. Nielsen, C. Gowers, M. Beurskens, et al. High resolution Thomson scattering for Joint European Torus (JET). *Review of Scientific Instruments*, 75(10):3891–3893, 2004.

[148] R. Scannell, M. Beurskens, P. G. Carolan, A. Kirk, et al. Deconvolution of Thomson scattering temperature profiles. *Review of Scientific Instruments*, 82(5):053501, 2011.

[149] L. Frassinetti, M. N. A. Beurskens, R. Scannell, T. H. Osborne, et al. Spatial resolution of the JET Thomson scattering system. *Review of Scientific Instruments*, 83(1):013506, 2012.

[150] L. L. Lao, H. St. John, R. D. Stambaugh, A. G. Kellman, et al. Reconstruction of current profile parameters and plasma shapes in tokamaks. *Nuclear Fusion*, 25(11):1611–1622, 1985.

[151] L. L. Lao, J. R. Ferron, R. J. Groebner, W. Howl, et al. Equilibrium analysis of current profiles in tokamaks. *Nuclear Fusion*, 30(6):1035–1049, 1990.

[152] M. J. Leyland, M. N. A. Beurskens, J. C. Flanagan, L. Frassinetti, et al. Edge profile analysis of Joint European Torus (JET) Thomson scattering data: Quantifying the systematic error due to edge localised mode synchronisation. *Review of Scientific Instruments*, 87(1):013507, 2016.

[153] A. Loarte, M. Becoulet, G. Saibene, R. Sartori, et al. Characteristics and scaling of energy and particle losses during Type I ELMs in JET H-modes. *Plasma Physics and Controlled Fusion*, 44(9):1815–1844, 2002.

[154] A. J. Webster and R. O. Dendy. Statistical characterization and classification of edge-localized plasma instabilities. *Phys. Rev. Lett.*, 110(15):155004, 2013.

[155] L. Frassinetti, D. Dodt, M. N. A. Beurskens, A. Sirinelli, et al. Effect of nitrogen seeding on the energy losses and on the time scales of the electron temperature and density collapse of type-I ELMs in JET with the ITER-like wall. *Nuclear Fusion*, 55(2):023007, 2015.

[156] C. Bowman, D. Dickinson, L. Horvath, A. E. Lunniss, et al. Pedestal evolution physics in low triangularity JET tokamak discharges with ITER-like wall. *Nuclear Fusion*, 58(1):016021, 2018.

[157] I. H. Hutchinson. *Principles of Plasma Diagnostics*. Cambridge University Press, second edition, 2002.

[158] A. Boboc, M. Gelfusa, A. Murari, P. Gaudio, et al. Recent developments of the JET far-infrared interferometer-polarimeter diagnostic. *Review of Scientific Instruments*, 81(10):10D538, 2010.

[159] A. Boboc, C. Gil, P. Pastor, P. Spuig, et al. Upgrade of the JET far infrared interferometer diagnostic. *Review of Scientific Instruments*, 83(10):10E341, 2012.

[160] E. de la Luna, J. Sánchez, V. Tribaldos, G. Conway, et al. Electron cyclotron emission radiometer upgrade on the Joint European Torus (JET) tokamak. *Review of Scientific Instruments*, 75(10):3831–3833, 2004.

[161] Y. Andrew, N. C. Hawkes, K. Crombe, and JET EFDA Contributors. Improved charge exchange spectroscopy on the Joint European Torus for ion temperature and rotation velocity profiles. *Review of Scientific Instruments*, 77(10):10E913, 2006.

[162] E. Delabie, N. Hawkes, T. M. Biewer, and M. G. O'Mullane. In situ wavelength calibration of the edge CXS spectrometers on JET. *Review of Scientific Instruments*, 87(11):11E525, 2016.

[163] C. Giroud, A. G. Meigs, C. R. Negus, K. D. Zastrow, et al. Impact of calibration technique on measurement accuracy for the JET core charge-exchange system. *Review of Scientific Instruments*, 79(10):10F525, 2008.

[164] N. C. Hawkes, E. Delabie, S. Menmuir, C. Giroud, et al. Instrumentation for the upgrade to the JET core charge-exchange spectrometers. *Review of Scientific Instruments*, 89(10):10D113, 2018.

[165] I. Balboa, G. Arnoux, T. Eich, B. Sieglin, et al. Upgrade of the infrared camera diagnostics for the JET ITER-like wall divertor. *Review of Scientific Instruments*, 83(10):10D530, 2012.

[166] O. Sauter, C. Angioni, and Y.R. Lin-Liu. Neoclassical conductivity and bootstrap current formulas for general axisymmetric equilibria and arbitrary collisionality regime. *Physics of Plasmas*, 6(7):2834–2839, 1999.

[167] O. Sauter, C. Angioni, and Y.R. Lin-Liu. Erratum: Neoclassical conductivity and bootstrap current formulas for general axisymmetric equilibria and arbitrary collisionality regime [Phys. Plasmas 6, 2834 (1999)]. *Physics of Plasmas*, 9(12):5140–5140, 2002.

[168] R. Hager and C. S. Chang. Gyrokinetic neoclassical study of the bootstrap current in the tokamak edge pedestal with fully non-linear Coulomb collisions. *Physics of Plasmas*, 23(4):042503, 2016.

[169] E. Stefanikova, L. Frassinetti, S. Saarelma, A. Loarte, et al. Effect of the relative shift between the electron density and temperature pedestal position on the pedestal stability in JET-ILW. In *43rd EPS Conference on Plasma Physics, Leuven*, page O4.117, 2016.

[170] E. Stefanikova, L. Frassinetti, S. Saarelma, A. Loarte, et al. Effect of the relative shift between the electron density and temperature pedestal position on the pedestal stability in JET-ILW and comparison with JET-C. *Nuclear Fusion*, 58(5):056010, 2018.

[171] L. Frassinetti, M. G. Dunne, U. Sheikh, S. Saarelma, et al. Role of the pedestal position on the pedestal performance in AUG, JET-ILW and TCV and implications for ITER. *Nuclear Fusion*, 59(7):076038, 2019.

[172] M. Romanelli, G. Corrigan, V. Parail, S. Wiesen, et al. JINTRAC: A System of Codes for Integrated Simulation of Tokamak Scenarios. *Plasma and Fusion Research*, 9:3403023, 2014.

[173] W. A. Houlberg, K. C. Shaing, S. P. Hirshman, and M. C. Zarnstorff. Bootstrap current and neoclassical transport in tokamaks of arbitrary collisionality and aspect ratio. *Physics of Plasmas*, 4(9):3230–3242, 1997.

[174] G. V. Pereverzev and P. N. Yushmanov. ASTRA: Automated System for TRansport Analysis. *IPP Report, Max Planck Institute for Plasmaphysics, Garching*, IPP 5/98, 2002.

[175] A. B. Mikhailovskii, G. T. A. Huysmans, W. O. K. Kerner, and S. E. Sharapov. Optimization of computational MHD normal-mode analysis for tokamaks. *Plasma Physics Reports*, 23(10):844–857, 1997.

[176] V. P. Bhatnagar, J. Lingertat, R. Barnsley, P. Breger, et al. Edge localized modes and edge pedestal in NBI and ICRF heated H, D and T plasmas in JET. *Nuclear Fusion*, 39(3):353–367, 1999.

[177] M. J. Leyland, M. N. A. Beurskens, L. Frassinetti, C. Giroud, et al. The H-mode pedestal structure and its role on confinement in JET with a carbon and metal wall. *Nuclear Fusion*, 55(1):013019, 2015.

[178] L. Frassinetti, M. N. A. Beurskens, S. Saarelma, J. E. Boom, et al. Global and pedestal confinement and pedestal structure in dimensionless collisionality scans of low-triangularity H-mode plasmas in JET-ILW. *Nuclear Fusion*, 57(1):016012, 2017.

[179] E. de la Luna, I. T. Chapman, F. Rimini, P. J. Lomas, et al. Understanding the physics of ELM pacing via vertical kicks in JET in view of ITER. *Nuclear Fusion*, 56(2):026001, 2015.

[180] D. Reiter. Progress in two-dimensional plasma edge modelling. *Journal of Nuclear Materials*, 196–198:80–89, 1992.

[181] R. Simonini, G. Corrigan, G. Radford, J. Spence, et al. Models and numerics in the multi-fluid 2-D edge plasma code EDGE2D/U. *Contributions to Plasma Physics*, 34(2–3):368–373, 1994.

[182] S. Wiesen. EDGE2D/EIRENE code interface report. *IRC Report*, 2006.

[183] G. J. Radford. The application of moment equations to scrape off layer plasmas. *Contributions to Plasma Physics*, 32(3–4):297–302, 1992.

[184] S. I. Braginskii. Transport processes in a plasma. *Reviews of Plasma Physics*, 1:205, 1965.

[185] H. Bufferand, B. Bensiali, J. Bucalossi, G. Ciraolo, et al. Near wall plasma simulation using penalization technique with the transport code SolEdge2D-Eirene. *Journal of Nuclear Materials*, 438:S445–S448, 2013.

[186] H. Bufferand, G. Ciraolo, Y. Marandet, J. Bucalossi, et al. Numerical modelling for divertor design of the WEST device with a focus on plasma-wall interactions. *Nuclear Fusion*, 55(5):053025, 2015.

[187] C. Day. Basics and applications of cryopumps. In *CERN Accelerator School, Vacuum in accelerators, Platja d'Aro, Spain, 16-24 May 2006*, pages 241–274, 2006.

[188] C. Day. Use of porous materials for cryopumping. In *Handbook of Surfaces and Interfaces of Materials*, pages 265–307. Academic Press, Burlington, 2001.

[189] H. Weisen, A. Zabolotsky, M. Maslov, M. Beurskens, et al. Scaling of density peaking in JET H-modes and implications for ITER. *Plasma Physics and Controlled Fusion*, 48(5A):A457–A466, 2006.

[190] C. Angioni, E. Fable, M. Greenwald, M. Maslov, et al. Particle transport in tokamak plasmas, theory and experiment. *Plasma Physics and Controlled Fusion*, 51(12):124017, 2009.

[191] A. Loarte, M. J. Leyland, J. A. Mier, M. N. A. Beurskens, et al. Plasma density and temperature evolution following the H-mode transition at JET and implications for ITER. *Nuclear Fusion*, 53(8):083031, 2013.

[192] P. C. Stangeby. *The Plasma Boundary of Magnetic Fusion Devices*. CRC Press, 2000.

[193] A. Kallenbach, N. Asakura, A. Kirk, A. Korotkov, et al. Multi-machine comparisons of H-mode separatrix densities and edge profile behaviour in the ITPA SOL and Divertor Physics Topical Group. *Journal of Nuclear Materials*, 337-339:381–385, 2005.

[194] J. Simpson, D. Moulton, C. Giroud, M. Groth, et al. Using EDGE2D-EIRENE to simulate the effect of impurity seeding and fueling on the upstream electron separatrix temperature. *Nuclear Materials and Energy*, 20:100599, 2019.

[195] S. Saarelma, A. Järvinen, M. Beurskens, C. Challis, et al. The effects of impurities and core pressure on pedestal stability in Joint European Torus (JET). *Physics of Plasmas*, 22(5):056115, 2015.

[196] G. T. A. Huysmans, S. E. Sharapov, A. B. Mikhailovskii, and W. Kerner. Modeling of diamagnetic stabilization of ideal magnetohydrodynamic instabilities associated with the transport barrier. *Physics of Plasmas*, 8(10):4292–4305, 2001.

[197] G. T. A. Huysmans, J. P. Goedbloed, and W. Kerner. Isoparametric bicubic Hermite elements for solution of the Grad-Shafranov equation. In *Proceedings of the CP90 Conference on Computational Physics*, volume 02, pages 371–376, 1991.

[198] N. Aiba, C. Giroud, M. Honda, E. Delabie, et al. Numerical analysis of ELM stability with rotation and ion diamagnetic drift effects in JET. *Nuclear Fusion*, 57(12):126001, 2017.

[199] N. Aiba, S. Pamela, M. Honda, H. Urano, et al. Analysis of ELM stability with extended MHD models in JET, JT-60U and future JT-60SA tokamak plasmas. *Plasma Physics and Controlled Fusion*, 60(1):014032, 2017.

[200] N. Aiba, M. Furukawa, M. Hirota, and S. Tokuda. Destabilization mechanism of edge localized MHD mode by a toroidal rotation in tokamaks. *Nuclear Fusion*, 50(4):045002, 2010.